Semi-analytical and numerical characterization of acoustic black holes in duct terminations

Davide Ghilardi

http://hdl.handle.net/10803/689196

Data de defensa: 06-10-2023

C.I.F. G: 59069740 Universitat Ramon Llull Fundació Rgtre. Fund. Generalitat de Catalunya núm. 472 (28-02-90)

ADVERTIMENT. L'accés als continguts d'aquesta tesi doctoral i la seva utilització ha de respectar els drets de la persona autora. Pot ser utilitzada per a consulta o estudi personal, així com en activitats o materials d'investigació i docència en els termes establerts a l'art. 32 del Text Refós de la Llei de Propietat Intel·lectual (RDL 1/1996). Per altres utilitzacions es requereix l'autorització prèvia i expressa de la persona autora. En qualsevol cas, en la utilització dels seus continguts caldrà indicar de forma clara el nom i cognoms de la persona autora i el títol de la tesi doctoral. No s'autoritza la seva reproducció o altres formes d'explotació efectuades amb finalitats de lucre ni la seva comunicació pública des d'un lloc aliè al servei TDX. Tampoc s'autoritza la presentació del seu contingut en una finestra o marc aliè a TDX (framing). Aquesta reserva de drets afecta tant als continguts de la tesi com als seus resums i índexs.

ADVERTENCIA. El acceso a los contenidos de esta tesis doctoral y su utilización debe respetar los derechos de la persona autora. Puede ser utilizada para consulta o estudio personal, así como en actividades o materiales de investigación y docencia en los términos establecidos en el art. 32 del Texto Refundido de la Ley de Propiedad Intelectual (RDL 1/1996). Para otros usos se requiere la autorización previa y expresa de la persona autora. En cualquier caso, en la utilización de sus contenidos se deberá indicar de forma clara el nombre y apellidos de la persona autora y el título de la tesis doctoral. No se autoriza su reproducción u otras formas de explotación efectuadas con fines lucrativos ni su comunicación pública desde un sitio ajeno al servicio TDR. Tampoco se autoriza la presentación de su contenido en una ventana o marco ajeno a TDR (framing). Esta reserva de derechos afecta tanto al contenido de la tesis como a sus resúmenes e índices.

WARNING. The access to the contents of this doctoral thesis and its use must respect the rights of the author. It can be used for reference or private study, as well as research and learning activities or materials in the terms established by the 32nd article of the Spanish Consolidated Copyright Act (RDL 1/1996). Express and previous authorization of the author is required for any other uses. In any case, when using its content, full name of the author and title of the thesis must be clearly indicated. Reproduction or other forms of for profit use or public communication from outside TDX service is not allowed. Presentation of its content in a window or frame external to TDX (framing) is not authorized either. These rights affect both the content of the thesis and its abstracts and indexes.

UNIVERSITAT
RAMON LLULL

DOCTORAL THESIS

Title	Semi-analytical and numerical characterization of acoustic black holes in duct terminations
Presented by	Davide Ghilardi
Centre	La Salle Digital Engineering School
Department	Engineering
Directed by	Dr. Oriol Guasch i Fortuny

Contents

Abstract **7**

Resum **8**

Resumen **9**

Acknowledgements **10**

List of Figures **11**

1 Introduction **16**
- 1.1 Motivation and scope 16
- 1.2 State of the art 17
  - 1.2.1 ABH - Fundamental principle 17
  - 1.2.2 ABH for beams and plates 19
  - 1.2.3 ABH for duct terminations 23
  - 1.2.4 Resolution methods 25
  - 1.2.5 Experimental results 31
- 1.3 Aims of the thesis 34
- 1.4 Thesis organization 35

2 Solution and analysis of theoretical acoustic black holes in duct terminations by Gaussian functions **37**
- 2.1 Introduction 38
- 2.2 Theoretical framework 40
  - 2.2.1 Generalized Webster equation in waveguides as a Helmholtz equation in an inhomogeneous medium 40
  - 2.2.2 Formulation of the acoustic black hole problem in a finite duct termination 42
  - 2.2.3 Variational formulation of the Helmholtz equation for the scaled pressure inside a ABH 44
  - 2.2.4 Gaussian expansion of the locally scaled acoustic pressure and test function 45
  - 2.2.5 Discretization and solution of the variational problem in terms of Gaussian functions 47

2.2.6 Quadratic eigenvalue problem and modal participation factors for the forced problem . . . 48
2.3 Simulation results . . . 49
2.3.1 Validation with FEM: a quadratic ABH . . . 49
2.3.2 Sound speed and wavenumber within the ABH . . . 52
2.3.3 Modal decomposition . . . 54
2.3.4 Reflection coefficient and admittance at the ABH entrance . . . 56
2.3.4.1 Influence of the residual radius, the damping and the ABH order on the reflection coefficient . . . 56
2.3.4.2 Influence of the residual radius and damping on the admittance 60
2.3.5 Alternative ABH profiles to the power-law: power-cosine, exponential and Gaussian. . . . 63
2.4 Conclusions . . . 64

3 The Transfer Matrix Method applied to acoustic black hole duct terminations 66
3.1 Introduction . . . 67
3.2 Governing differential equations and TMM approximation . . . 69
3.2.1 Governing equation for the ABH in a duct termination . . . 69
3.2.2 Governing equation of plane waves in a duct filled with a non-homogeneous fluid . . . 71
3.2.3 The Transfer Matrix Method (TMM) for ABHs . . . 72
3.3 Consistency of the TMM . . . 76
3.3.1 The metafluid analogy . . . 76
3.3.2 The TMM for multilayered media . . . 79
3.3.3 Proof of consistency of the TMM solution . . . 80
3.4 Numerical results . . . 85
3.4.1 The ABH reflection coefficient . . . 85
3.4.2 Numerical simulations . . . 86
3.5 Conclusions . . . 88

4 Finite element simulations of the linear and quadratic ABH in duct terminations 90
4.1 Introduction . . . 91
4.2 Methodology . . . 92
4.2.1 The wave equation in mixed form . . . 92
4.2.2 Finite Element simulations . . . 93
4.2.3 The two microphone transfer function method . . . 94
4.3 Results of the FEM simulations . . . 96
4.3.1 Influence of the number of rings and of the ABH order . . . 96
4.3.2 Influence of the boundary admittance coefficient . . . 97
4.3.3 Influence of the ring thickness . . . 99
4.3.4 Pressure distribution inside the ABH . . . 100
4.3.5 Influence of the ABH final wall . . . 104
4.3.6 Occlusion of the first cavities . . . 105

4.4 Conclusions 107

5 Conclusions and future work **108**

5.1 Conclusions 108
5.2 Future work 111
5.3 Publications 113

Abstract

In recent times, the acoustic black hole (ABH) effect has been studied for noise control in ducts, while it originates for structural waves propagating in beams and plates. The comprehension of an ABH can be tackled by different methods: mathematical and analytical techniques, transfer matrix method (TMM) and finite element method (FEM) simulations, alongside with experiments.

In this thesis, the three aforementioned methods are considered. A new theoretical framework, based on Gaussian discretization of the variational formulation of Helmholtz equation is proposed. The problem considered involves a rigid residual surface at the termination of the ABH and the proposed approach allows to compute the ABH modes through an eigenvalue problem. Therefore, this theoretical approach is validated against FEM results, showing a very strong agreement. Then, the transfer matrix method is introduced and applied to the ABH problem. It is shown that the TMM solution formally tends to the solution of the ABH equation in the limit cases of number of rings tending to infinity. In order to do that, the concept of a metamaterial is used and the analogy between an acoustic wave propagating in an ABH and a wave propagating in a duct filled with a metafluid with particular physical properties is discussed. Finally, some preliminary FEM results are obtained and discussed. The influence of many parameters, such as number of rings and ABH order, on the ABH performance, expressed in terms of its reflection coefficient, is discussed. FEM results are the most expensive (as for computational cost) and closest to reality. In fact, FEM allows to visualize and understand the physics inside the ABH termination.

Resum

En els últims anys, s'ha estudiat l'efecte dels forats negres acústics (ABHs) per tal de controlar el soroll en conductes, tot i que originàriament es van desenvolupar per la propagació d'ones estructurals en bigues i plaques. Un ABH es pot caracteritzar de diferents maneres: per mitjà de tècniques matemàtiques analítiques, amb el mètode de les matrius de transferència (TMM) o amb el mètode numèric dels elements finits (FEM), conjuntament amb experiments. En aquesta tesi es consideren els tres mètodes esmentats. Es proposa un nou marc teòric, basat en la discretització de la formulació variacional de l'equació de Helmholtz fent servir funcions de base Gaussianes. El problema considerat inclou una superfície residual rígida a la terminació de l'ABH i l'enfocament proposat permet calcular els modes de l'ABH a partir d'un problema de valors propis. Aquest enfocament semi-analític s'ha validat amb simulacions FEM i el grau de similitud és molt notable. A continuació, s'ha introduït el mètode de les matrius de transferència i s'ha aplicat al problema dels ABHs. Es demostra que la solució TMM tendeix formalment a la solució de l'equació de l'ABH en el cas límit en què el nombre d'anells tendeix a infinit. A tal efecte s'utilitza el concepte de metamaterial i es discuteix l'analogia entre una ona acústica que es propaga en un ABH i una ona que es propaga en un conducte ple d'un metafluid amb propietats físiques particulars. Finalment, s'obtenen i es discuteixen alguns resultats preliminars dels ABH obtinguts amb FEM. S'analitza la influència de diferents paràmetres, com el nombre d'anells i l'ordre de l'ABH en el coeficient de reflexió de l'ABH. Els resultats FEM són els més costosos (pel que fa al cost computacional) i els més propers a la realitat. De fet, el FEM permet visualitzar i entendre millor la física a l'interior de la terminació ABH.

Resumen

En los últimos años, se ha estudiado el efecto de los agujeros negros acústicos (ABHs) para controlar el ruido en conductos, aunque originariamente se desarrollaron para la propagación de ondas estructurales en vigas y placas. Un ABH puede caracterizarse de diferentes formas: mediante técnicas matemáticas analíticas, con el método de las matrices de transferencia (TMM) o con el método numérico de los elementos finitos (FEM), a la vez que con experimentos. En esta tesis se consideran los tres métodos citados. Se propone un nuevo marco teórico, basado en la discretización de la formulación variacional de la ecuación de Helmholtz utilizando funciones de base Gaussianas. El problema considerado incluye una superficie residual rígida en la terminación del ABH y el enfoque propuesto permite calcular los modos del ABH a partir de un problema de valores propios. Este enfoque semianalítico se ha validado con simulaciones FEM y el grado de similitud es muy notable. A continuación, se ha introducido el método de las matrices de transferencia y se ha aplicado al problema de los ABHs. Se demuestra que la solución TMM tiende formalmente a la solución de la ecuación del ABH en el caso límite en el que el número de anillos tiende a infinito. A tal efecto se utiliza el concepto de metamaterial y se discute la analogía entre una onda acústica que se propaga en un ABH y una onda que se propaga en un conducto lleno de un metafluido con propiedades físicas particulares. Por último, se obtienen y se discuten algunos resultados preliminares de los ABHs obtenidos con FEM. Se analiza la influencia de distintos parámetros, como el número de anillos y el orden del ABH en el coeficiente de reflexión del ABH. Los resultados FEM son los más costosos (con respecto al coste computacional) y los más cercanos a la realidad. De hecho, el FEM permite visualizar y entender mejor la física en el interior de la terminación ABH.

Acknowledgements

I would like to dedicate the first words of thanks to Prof. Oriol Guasch i Fortuny. Throughout all these years, you have always been helpful and managed to motivate me even in difficult times. You have always shared with me many ideas that have contributed to shape my scientific background.

Then, I would like to thank the co-authors of the works that are the basis for this thesis. Dr. Marc Arnela, Dr. Deng Jie and Dr. Patricia Sánchez-Martín, I knew I could count on you at any time and you helped me a lot when I had a doubt and in moments of uncertainty.

A big thank you also goes to my girlfriend María, who managed to put up with me all these years. Thank you, you have always been a valuable support and you have always listened to me and given me the right advice at the right time. This work would obviously not have been possible without you.

Last but not least, I would like to thank my mother Mariangela, my father Alfio, my sister Federica, my brother-in-law Stefano and my nephew Leonardo. Being apart is never an easy thing, but I know that when we see each other in person you manage to give me moments of happiness and calm.

List of Figures

1.1 (a) A beam with a wedge whose thickness is exponentially decreasing (Pelat *et al.*, 2020), (b) The two-dimensional view of an ABH termination for the case of a duct made of rings whose radii decrease by following a power-law (adapted from Deng, 2020) and (c) a two-dimensional circular ABH inserted in a plate (Pelat *et al.*, 2020). 18

1.2 (a) Ideal ABH where the vibration energy concentrates at the end of the wedge (adapted from Zhao and Prasad, 2019), (b) practical realization of an ABH, where the power-law profile is truncated and an aborbing layer (in green) is added. 20

1.3 (a) Incident and (b) reflected wave without damping layer and (c) incident and (d) reflected wave with damping layer. The comparison between (b) and (d) shows that the reflected wave is much smaller when the damping layer is considered, as the energy dissipation is higher (from Ji *et al.*, 2018). 22

1.4 (a) Two-dimensional view of an incident wave travelling in a duct with an ABH termination made by rings separated by air cavitites (adapted from (Guasch *et al.*, 2017), (b) 3-D view of a duct (in grey) equipped with an ABH termination (in blue), (c) The ABH termination made of rings, separated by air cavities, whose inner radii decrease by following a power law is showed. 24

1.5 The basic setup for the application of the Transfer Matrix Method (TMM). The state variables v_d and p_d can be related to v_u and p_u by a matrix multiplication (figure inspired from (Mechel, 2002)). 27

1.6 Influence of the number of rings on the reflection coefficient for linear (a) and quadratic (b) ABHs. Influence of damping with complex sound speed on the reflection coefficient for linear (c) and quadratic (d) cases (adapted from Guasch *et al.*, 2017). . 28

1.7 Comparison between reflection coefficients computed via Linearized Navier-Stokes Equations (LNSE) or Helmholtz Equation (HE) for a cavity width of 0.25m (a) and 0.75m (b) (Cervenka and Bednarík, 2022). The normalized power loss of all loss mechanisms (c) and magnitude of the reflection coefficient for two cases: only visco-thermal losses considered and layer of melamine foam added at the end of each cavity (outer tube) (Mousavi *et al.*, 2022). 30

1.8 Wave propagation and pressure distribution inside ABH cavities along time. Reflection can be appreciated in yellow in (d). See Chapter 4 for more details. 31

1.9 (a) A rectangular plate with a power-lae profiled wedge, (b) practical realization of a quadratic ABH for a duct termination, (c) plate with a two-dimensional ABH realized through a circular indentation with a power-law profile. 32

1.10 (a) Experimental setup and (b) corresponding results for a quadratic ABH whose last ring holes are covered by different materials (El Ouahabi *et al.*, 2015), (c) experimental setup and (d) corresponding result for a quadratic ABH whose last cavities are filled with materials with increasing density (Mironov and Pislyakov, 2020), (e) experimental setup and (f) corresponding results for an open-end ABH (Mi *et al.*, 2021). . . . 34

2.1 Schematic of the ABH problem. A wave propagating inside the uniform duct impinges on an ABH of length L, which is characterized by a small reflection coefficient $\mathcal{R}$ with corresponding inlet admittance Y_L. The wave within the ABH slows down, while its amplitude grows and its wavelength diminishes as it approaches the termination of the ABH. The profile of the ABH is defined by its radius $r(x)$, which varies from that of the uniform duct at the input, R, to the residual r_0. The residual cross-section $S_0 = \pi r_0^2$ is considered to be perfectly rigid. The ABH has a wall admittance $Y(x)$. 43
2.2 Gaussian basis functions distributed along the ABH termination. 46
2.3 Real part of acoustic pressure, $\mathrm{Re}(\hat{p})$, computed with the FEM and GEM at (a) 100 Hz, (b) 200 Hz, (c) 300 Hz, and (d) 400 Hz. The pressure has been normalized to unity at the ABH termination $x = 0$ to facilitate comparisons. 50
2.4 Comparison of the reflection coefficient for the quadratic ABH calculated with FEM and GEM. 51
2.5 (a) Sound speed $c_Y(x) = c_0 r(x)/R$ and wavenumber $k(x) = k_0 R/r(x)$ for acoustic pressure waves $\hat{p}$ propagating within the ABH. (b) $|c_\kappa(x)|$ and $|\kappa(x)|$ for scaled pressure waves ϕ propagating inside the ABH. 52
2.6 Mode shapes for (a) $r_0 = 0.01$ m and (b) $r_0 = 0.001$ m. For both cases we have considered damping with $\eta = 0.05$. 53
2.7 Black line: real part of the sound pressure at $x = -L$, $\mathrm{Re}[\hat{p}(-L)]$. Colored lines: modal contributions to $\mathrm{Re}[\hat{p}(-L)]$. (a) $r_0 = 0.01$ m and $\eta = 0$, (b) $r_0 = 0.01$ m and $\eta = 0.05$, (c) $r_0 = 0.001$ m and $\eta = 0$, (d) $r_0 = 0.001$ m and $\eta = 0.05$. 55
2.8 Influence of the residual radius r_0 for fixed ABH order $m = 2$ and damping $\eta = 0.05$ on (a) the absolute value of the reflection coefficient, $|\mathcal{R}|$, (b) the sound pressure distribution within the ABH at 344.8 Hz. 57
2.9 Influence of the damping η for fixed ABH order $m = 2$ and residual radius $r_0 = 0.001$ m on (a) the absolute value of the reflection coefficient, $|\mathcal{R}|$, (b) the sound pressure distribution within the ABH at 383.2 Hz. 57

2.10 Influence of ABH order m for fixed residual radius $r_0 = 0.001$ m and damping $\eta = 0.05$ on (a) the absolute value of the reflection coefficient, $|\mathcal{R}|$, (b) the sound pressure distribution within the ABH at 364 Hz. 58
2.11 Comparison of the absolute value of the reflection coefficient, $|\mathcal{R}|$, for two quadratic ($m = 2$) ABHs of lengths $L = \{0.25, 0.5\}$ m and two quartic ($m = 4$) ABHs with $L = \{0.5, 1\}$ m. 59
2.12 ABH admittance Y_L depending on frequency for varying residual radius r_0 and damping η. 59
2.13 ABH admittance depending on frequency and location within the ABH for varying residual radius r_0 and damping η. (a) $r_0 = 0.01$ m and $\eta = 0$. (b) $r_0 = 0.01$ m and $\eta = 0.05$. (c) $r_0 = 0.001$ m and $\eta = 0.05$. (d) $r_0 = 0.0001$ m and $\eta = 0.05$. . 61
2.14 (a) Power-cosine profiles and (b) corresponding reflection coefficients for different values of m. 62
2.15 (a) Exponential profiles and (b) corresponding reflection coefficient for different values of β. 62
2.16 (a) Gaussian profiles and (b) corresponding reflection coefficients for different values of γ. 63

3.1 Sketch of a cylindrical duct with an ABH termination where a quarter of the cylinder has been removed in order to show the inner ABH structure made of rings and cavities. 69
3.2 Sketch of a cavity plus ring ensemble (Guasch *et al*, 2017). . . 73
3.3 Duct termination filled with metafluid whose governing equation is analogous to that of the ABH in Figure (3.1) 76
3.4 Division of the ABH termination into N layers of same width L/N and constant density in order to apply the TMM to describe wave propagation through the metafluid. 80
3.5 Comparison between analytical and TMM reflection coefficients for the linear (a)-(b) and quadratic (c)-(d) ABHs. . . . 87

4.1 Two-dimensional view of the computational domain. 94
4.2 Sketch of the circular duct with an ABH termination at its right end. 95
4.3 Tested geometries: linear and quadratic ABHs with $N = 20$ and $N = 40$ rings. 97

4.4 Influence of the number of rings on $|\mathcal{R}|$ for the linear (a) and quadratic (b) cases. 98
4.5 Influence of the boundary admittance coefficient μ on $|\mathcal{R}|$ for linear and quadratic ABHs. (a) Linear ABH with $N = 20$ rings, (b) Quadratic ABH with $N = 20$ rings, (c) Linear ABH with $N = 40$ rings, and (d) Quadratic ABH with $N = 40$ rings. 99
4.6 Influence of the ring thickness on the reflection coefficient for the linear case with $N = 20$ rings. 100
4.7 The points P_1 (in green), P_2 (in red) and P_3 (in black) located on the ABH center line. 101
4.8 (a) Pressure signals measured inside the ABH at points $P_1 = (-0.5, 0)$, $P_2 = (-0.237, 0)$ and $P_3 = (-0.062, 0)$ and (b) corresponding spectra. 101
4.9 Pressure evolution at different times. 102
4.10 Comparison between scaled reflection coefficient (in red) and pressure spectra for $\mu = 0.0005$ (a) Linear ABH with $N = 20$ rings, (b) Quadratic ABH with $N = 20$ rings, (c) Linear ABH with $N = 40$ rings, and (d) Quadratic ABH with $N = 40$ rings. 103
4.11 The wall at the end of the ABH termination has an influence only at low frequencies (the last cavities). 104
4.12 Two different views of the same geometry: linear ABH with 16 cavities and 4 occluded. 105
4.13 Comparison between reflection coefficients for configurations with 20 and 16 cavities (4 occluded), for linear (top) and quadratic (bottom) order, with $\mu = 0.005$ (left) and $\mu = 0.001$ (right). 106
4.14 Comparison between linear profile with absorption and without it. Linear ABHs with $\mu = 0.005$ and $\mu = 0.0005$. 106

Chapter 1

Introduction

1.1 Motivation and scope

The acoustic black hole (ABH) effect has gained many attention in the past two decades, although the pioneering works with its original theory dates back to the late 80s. Such an effect can be applied both to structural waves, for vibration reduction, and to acoustic waves, for sound control. The most interesting aspect of the ABH problem is that it is a mathematical, physical and engineering challenge simultaneously. Moreover, many resolution methods are available and can be used to tackle this problem, such as analytical, semi-analytical and numerical (like the Transfer Function Method and the Finite Element Method) methods. Approaching the ABH problem with any of these methods carries its advantages and its drawbacks. In fact, the analytical approach to the ABH problem is crucial to understand theoretical limitations, although it relies on many simplifications and assumptions that cannot be fulfilled in reality. The numerical study of this problem through TMM (Transfer Matrix Method) will be addressed, because it is much less computationally expensive and it allows to quickly analyze and study many configurations. In those analyses, many parameters such as number and thickness of rings, distance between rings, inner radius law and material properties can be studied and compared, so that only selected promising configuration can be furthered analyzed. But, the TMM will not allow to gain insights on the physics of the ABH and on the behavior of the cavities during the absorption process. Finally, the ABHs will be studied through FEM (Finite Element Method), which gives results much closer to the real design and helps in the comprehension of the physics of this phenomenon, although it has a high complexity and depends on many parameters. Above

all, the key aspect is the connection between results achieved through different methods.
It is at the aim of this work to contribute to the analytical and numerical characterization of an Acoustic Black Hole.

1.2 State of the art

1.2.1 ABH - Fundamental principle

The achievement of an efficient passive structural vibration control is a well-known challenge in mechanical engineering. While composite materials have been a first approach to this problem, later the concept of "metamaterial" started to be explored. A metamaterial consists in a material whose properties cannot be found in nature. Those physical properties, in fact, are achieved via strategic geometry placed in a convenient way. Finally, the consideration of acoustic black holes (ABHs), which are traps for flexural elastic waves, is also a recent endeavor.
The initial formulation of the concept of an ABH can be found in (Mironov, 1988), which is considered as the pioneering work of the whole research field. There, the propagation of flexural waves in a plate having a wedge whose thickness is decreasing by following a power-law (see Fig. 1.1(a)) is studied. By following an analytical approach, it was showed for the first time that a non-reflecting termination can be achieved, under the assumption of a vanishing wedge thickness. In this ideal case, in fact, the velocity of the incoming flexural wave is progressively diminishing to zero, so that the tip of the wedge will never be reached (the needed time will tend to infinity) and the wave will remain trapped inside the wedge, resulting in a perfect absorption. In (Mironov and Pislyakov, 2002) the same idea has been extended to the case of an acoustic tube with an axially varying wall impedance (see Fig. 1.1(b)). Later, the same concept of retarding structure was extended in (Krylov, 2007) to the context of plates, by the insertion of axisymmetric circular pits with power-law varying thickness (see Fig. 1.1(c)). The mentioned circular pits are playing the same role as the wedges in plates: they can slow down and trap flexural waves. It has to be underlined that the properties of such structures led Krylov to coin the term "acoustic black hole". Strictly speaking, it would be convenient to make a distinction between "Vibration Acoustic Black Holes", i.e the ones developed in the context of structural dynam-

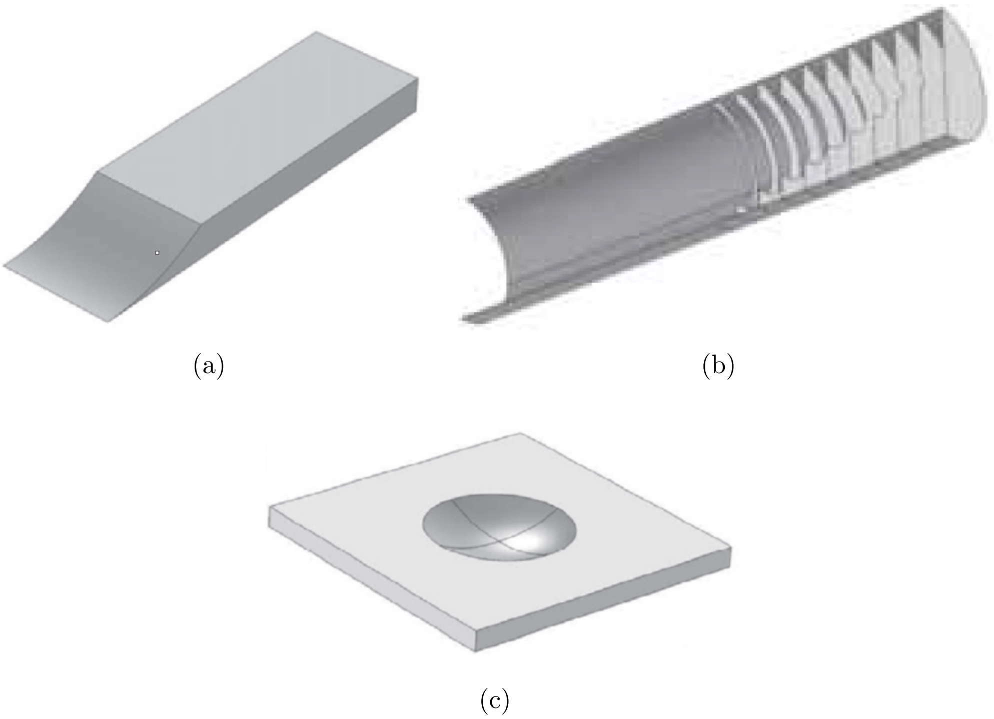

(a) (b)

(c)

Figure 1.1: (a) A beam with a wedge whose thickness is exponentially decreasing (Pelat *et al.*, 2020), (b) The two-dimensional view of an ABH termination for the case of a duct made of rings whose radii decrease by following a power-law (adapted from Deng, 2020) and (c) a two-dimensional circular ABH inserted in a plate (Pelat *et al.*, 2020).

ics, and "Sonic (acoustic) Black Holes" (SBH), which deals with acoustic ducts equipped with varying area terminations (as proposed in Mironov and Pislyakov, 2020). In any case, the more general expression ABH is very common and recognized by the scientific community to refer to power-law type absorbers and it will be used throughout the thesis.

Beyond the designs represented in Fig. 1.1 (that are: wedge, duct termination and circular), others have been proposed such as circular bar (Kralovic and Krylov, 2007; Kalkowski *et al.*, 2017; Zeng *et al.*, 2019), double-leaf (Tang and Cheng, 2017; Zhou *et al.*, 2017), spiral (Lee and Jeon, 2017; Park *et al.*, 2019), curved (Deng *et al.*, 2020), rectangular (Bowyer and Krylov, 2016; O'Boy and Krylov, 2016) and annular (Deng *et al.*, 2019).

Several review articles on ABHs can be found in literature (see e.g., Krylov, 2014; Pelat *et al.*, 2020).

1.2.2 ABH for beams and plates

One-dimensional ABHs

First of all, the case of ideal zero-reflection wedges is considered. In this context, a flexural wave propagating in a beam decreases its velocity when it enters into a wedge with a decreasing thickness. Therefore, a retarding structure can be achieved if the wedge thickness decreases smoothly to zero, resulting in an infinite time for the wave to reach its end. Such structure was originally proposed in (Mironov, 1988) and it was implemented in a tapered beam of power law profile whose thickness variation is given by $h(x) = \epsilon x^m$, where m is a real constant defining the ABH order, x stands for the axial coordinate along the wedge and ϵ is the so-called smoothness constant. In (Krylov, 1990) a quadratic profile was, the choice being motivated by a smoothness condition that needs to be satisfied. In a general case, the equation of motion for a flexural wave reads as

$$-\rho_L(x)\omega^2 w(x) + \frac{\partial^2}{\partial x^2} D(x) \frac{\partial^2 w(x)}{\partial x^2} = 0, \tag{1.1}$$

where $w(x)$ is the beam flexural displacement, ω the angular frequency, $\rho_L(x)$ the linear mass density and $D(x)$ the bending stiffness. Eq. (1.1) can be solved via the Wentzel, Kramers and Brillouin (WKB) method, that provides analytical solutions with different orders of approximation (Karlos *et al.*, 2019). The first-order WKB approximation provides the variation of the local phase velocity and it is observed that it tends to zero when the thickness tends to zero as well. Namely, the local phase velocity $c_\phi(x)$ and wavenumber $k(x)$ can be written as

$$c_\phi(x) = \left(\frac{E\omega^2}{12\rho(1-\nu^2)}\right)^{1/4} \sqrt{h(x)}, \tag{1.2}$$

$$k(x) = \frac{\omega}{c_\phi(x)} = \left(\frac{12\rho(1-\nu^2)}{E}\right)^{1/4} \sqrt{\frac{\omega}{h(x)}}, \tag{1.3}$$

where E stands for the Young's modulus, ν for the Poisson's ratio and ρ for the density of the material, and the local group velocity is $c_{gr}(x) = 2c_\phi(x)$. If the power-law $h(x) = \epsilon x^m$ is substituted into Eq. (1.2) and Eq. (1.3), one can get the following proportionality relationships for the phase velocity and the wavenumber respectively,

$$c_\phi(x) \propto \epsilon^{\frac{1}{2}} x^{\frac{m}{2}}, \tag{1.4}$$

$$k(x) \propto \epsilon^{-\frac{1}{2}} x^{-\frac{m}{2}}. \tag{1.5}$$

It can be observed that for $m \geq 2$ the wave speed tends to zero and the wavenumber goes to infinity at $x = 0$. Consequently, the wave would stay trapped inside the wedge and no reflection would occur since the travel time of a wave packet from a starting point to the wedge tip tends to infinity when the wave is approaching the tip. This mechanism implies that the energy accumulates inside the wedge and tends to infinity at its tip, which therefore turns out to be a point of singularity (see Fig. 1.2(a)). However, in practical structures it is not possible to build a wedge with zero residual thickness and a residual thickness needs to be introduced.

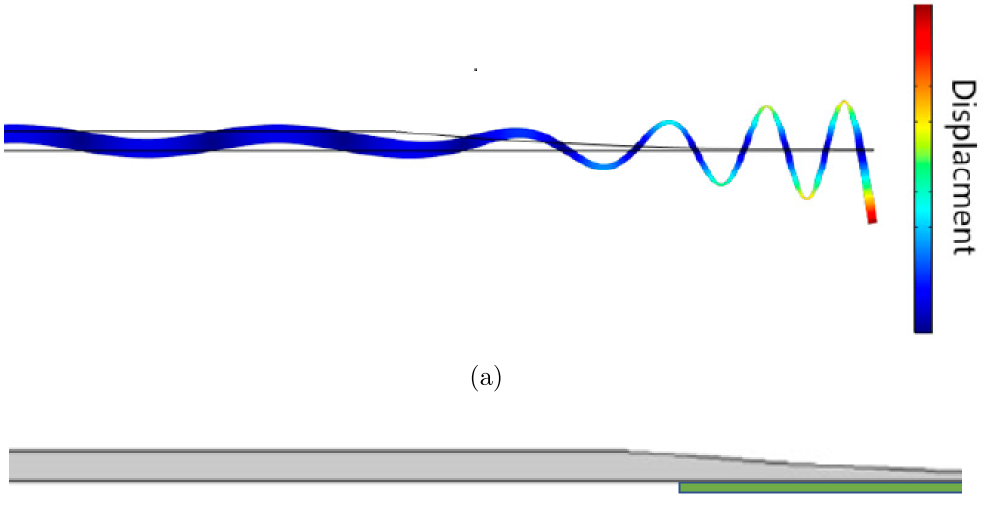

(a)

(b)

Figure 1.2: (a) Ideal ABH where the vibration energy concentrates at the end of the wedge (adapted from Zhao and Prasad, 2019), (b) practical realization of an ABH, where the power-law profile is truncated and an aborbing layer (in green) is added.

This fact establishes the difference between an ideal and a realistic implementation of the ABH and will have a strong impact on its performance. As an example, while an ideal ABH would result in perfect absorption (that is, zero reflection), a residual tip thickness equal to 0.1% can generate a reflection of 70% of the incoming wave (Mironov, 1988). Moreover, the case of an ideal ABH was first studied with the first order approximation of the WKB (Wentzel, Kramers, and Brillouin) method, known as the geometrical acoustic approach, and a zero reflection coefficient was obtained (Krylov, 1990). Considering the intrinsic limitations of the ideal ABH, practical wedges with damping layers applied to tapered wedges in order to mitigate the effects produced by the finite residual thickness (see Fig. 1.2(b)) have been explored (Krylov, 2004; Krylov and Tilman, 2004). Hereafter, the thickness of the added layer is considered thin with respect to the plate thickness and this leads to a simplification of the Ross-Ungar-Kerwin model (Ross *et al.*, 1959), used to describe sandwich structures. The viscoelastic layer turns out to be very effective in the reduction of the reflection coefficient even for the case of a truncated profile. In fact, in (Ji *et al.*, 2018) the incident and the reflected waves have been visualized separately with a laser scanning technique and the influence of the damping layer on the reflection process has been clarified (see Fig. 1.3). In Fig. 1.3(a) the incident wave is visualized in the time-space domain (t,x) and, in Fig. 1.3(b) the corresponding reflected wave is shown. In this case, damping layer is not considered and, therefore, it can be observed roughly the same amount of incident and reflected waves. In Fig. 1.3(c) and Fig. 1.3(d) the same visualization is presented, but with the addition of a damping layer. It is easy to notice that the damping layer plays a fundamental role in the absorption process, since the energy dissipation is much higher than the previous case.

Moreover, by applying a higher-order WKB model, it has been found in (Karlos *et al.*, 2019) that the reflection coefficient is the result not only of the effect of the truncation thickness, but also of the thickness mismatch at the junction of the host structure with the ABH wedge.

Finally, in (Tang and Cheng, 2017) locally resonant band gaps in a beam with multiple ABHs are observed. A new type of beam structure, equipped with two double-leaf acoustic black hole indentations, is proposed (see, Tang and Cheng, 2017c).

Two-dimensional ABHs

Due to the required boundary conditions, manufacturing an ABH at the edge of a structure is not a viable option. Therefore, the natural two-dimensional extension of the one-dimensional ABH arises and consists in an axisymmetric indentation with a radial power-law profile embedded in a thin plate.

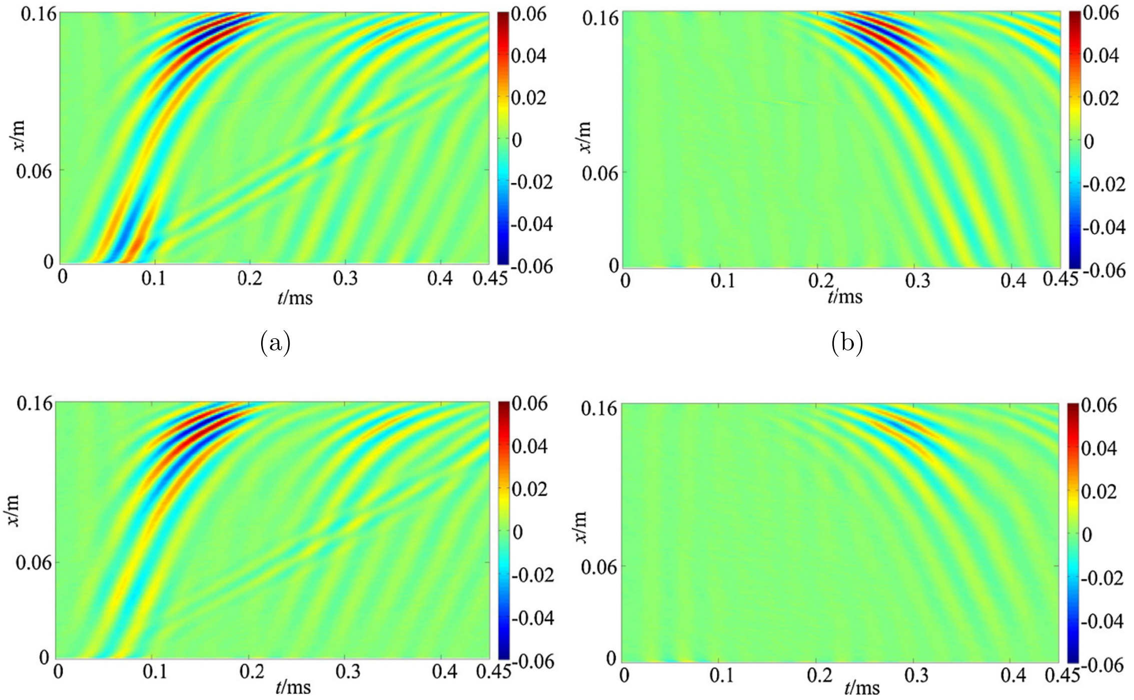

(a) (b)

(c) (d)

Figure 1.3: (a) Incident and (b) reflected wave without damping layer and (c) incident and (d) reflected wave with damping layer. The comparison between (b) and (d) shows that the reflected wave is much smaller when the damping layer is considered, as the energy dissipation is higher (from Ji *et al.*, 2018).

This structure has been proposed in (Krylov, 2007) and a first experimental demonstration of a 2D ABH can be found in (Georgiev *et al.*, 2011). Since then, many different geometrical designs have been proposed, such as 2D ABH with a central hole, a central plateau or a central added mass. In 2D circular ABHs, the focusing and lensing effects have been studied numerically (Climente *et al.*, 2014) and shown experimentally (Yan *et al.*, 2016). Following the analogy with the 1D ABH, the effect of 2D circular ABHs on flexural waves propagation in the high frequency regime has been studied using geometrical acoustic theory (Lomonosov *et al.*, 2016; Yan *et al.*, 2016). In (Tang and Cheng, 2019), by extending the design for the one-dimensional case, a new ABH design to generate directional band gaps for flexural waves was proposed, consisting of plates with periodically arranged tunneled double-leaf ABH. In (Tang and Cheng, 2020) this design is showed to achieve sound reduction at low frequencies without adding damping treatment.

1.2.3 ABH for duct terminations

In literature, most of the research has been dedicated to ABHs in beams and plates, while the fundamental theoretical principles of ABHs in ducts were formulated in (Mironov and Pislyakov, 2002). The retarding structure proposed to achieve an ABH effect is a termination of the cylindrical waveguide made of rings with power-law decreasing radii separated by air cavities (see Fig. 1.4).

Therefore, the walls have a variable admittance that, with the assumption of lumped-elements, reads as

$$Y = -\mathrm{j}k_0 Y_0 \frac{R^2 - r^2}{2r}, \tag{1.6}$$

where j is the imaginary unit, k_0 the wavenumber, Y_0 the characteristic admittance, R the duct radius and r the rings inner radius. The linear power-law has been considered for the computation of the inner radii of the rings, that is

$$r(x) = R\left(\frac{x}{L}\right)^m, \tag{1.7}$$

where R is the radius of the duct, L is the length of the retarding structure and $m = 1$. It is worth to observe that $r(L) = R$ and $r(0) = 0$. For this case, it has been proved that the time taken for a wave to propagate into the retarding structure would tend to infinity. In fact, the physical phenomenon under consideration is the wave propagation in an axisymmetric waveguide with varying cross section $A(x)$ and wall admittance $Y(x)$, which can be modelled with a generalized Webster equation for the acoustic pressure $p(x)$,

$$\frac{\mathrm{d}^2 p}{\mathrm{d}x^2} + \frac{\mathrm{d}p}{\mathrm{d}x}\frac{\mathrm{d}(\ln A)}{\mathrm{d}x} + p\left[k_0^2 + \mathrm{j}Z_0 k_0 \frac{2Y}{r}\right] = 0. \tag{1.8}$$

Eq. (1.8) is the starting point to derive two important results. First, by inserting Eq. (1.6) and Eq. (1.7), the equation will be referred to as "ABH equation" can be written, namely

$$\frac{\mathrm{d}^2 p}{\mathrm{d}x^2} + \frac{2m}{x}\frac{\mathrm{d}p}{\mathrm{d}x} + \left(\frac{k_0 L^m}{x^m}\right)^2 = 0. \tag{1.9}$$

Here, m is the order of the ABH. Therefore, equations for linear and quadratic configurations can be easily retrieved by substituting $m = 1$ or $m = 2$ respectively into Eq. (1.9). Second, it can be shown that the linear ABH follows

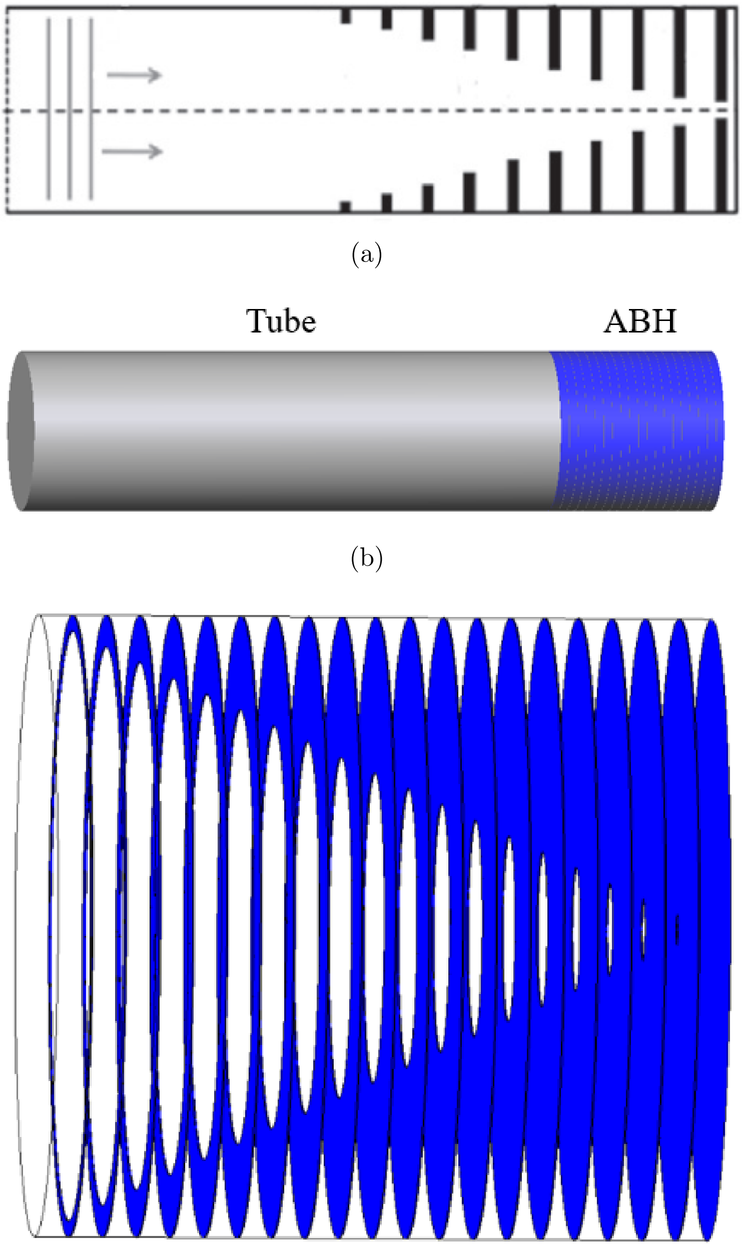

(a)

(b)

(c)

Figure 1.4: (a) Two-dimensional view of an incident wave travelling in a duct with an ABH termination made by rings separated by air cavitites (adapted from (Guasch *et al.*, 2017), (b) 3-D view of a duct (in grey) equipped with an ABH termination (in blue), (c) The ABH termination made of rings, separated by air cavities, whose inner radii decrease by following a power law is showed.

the acoustic black hole definition. In fact, from Eq. (1.8) and considering

Eq. (1.7) with $m = 1$, an expression for the wavenumber can be derived,

$$k(x) = \frac{1}{x}\sqrt{k_0^2 L^2 - 1}. \tag{1.10}$$

Making use of this expression for the wavenumber, phase velocity c_{ph}, group velocity c_{g} and the propagation time T inside the ABH structure (from $x = -L$ to $x_1 = -l$) can be computed,

$$c_{\mathrm{ph}} = \frac{\omega}{k} = -\frac{\omega}{\sqrt{k_0^2 L^2 - 1}} x, \tag{1.11}$$

$$c_{\mathrm{g}} = -\frac{c^2\sqrt{k_0^2 L^2 - 1}}{L^2 \omega} x, \tag{1.12}$$

$$T = \int_{-L}^{x_1} \frac{dx}{c_{\mathrm{g}}} = \frac{L^2 \omega}{c^2\sqrt{k_0^2 L^2 - 1}} \ln\left(\frac{L}{l}\right). \tag{1.13}$$

For $x \to 0$, which means approaching the ABH end, the wavenumber tends to infinity and, consequently, both velocities tend to zero. Moreover, for $x_1 = -l \to 0$, the propagation time tends to infinity. Therefore, it can be concluded that the structure taken into consideration behaves as an acoustic black hole, but, similarly to the case of ABHs for beams and plates, a small imperfection l needs to be introduced at the end of the ABH termination. This consideration will mark the difference between ideal ABHs and more realistic ones. Moreover, in (Mironov and Pislyakov, 2002) an overall reduction of the reflection coefficient is observed for a linear ABH and an exact solution is derived for this case. Finally, the above results have been derived for the quadratic case in (Guasch *et al.*, 2017). In this work it has been proven that, for $m = 2$ in Eq. (1.9), the group velocity tends to zero and the propagation time tends to infinity.

1.2.4 Resolution methods

Semi-analytical methods

The study of plates with ABH needs rapid and precise methods to analyze their behavior, which depends on many parameters such as the shape and size of the indentations. Many analytical methods (see Huang *et al.*, 2018; Li and

Ding, 2019; Georgiev *et al.*, 2011) rely on very strong simplifications, such as the consideration of semi-infinite structures. A semi-analytical method, considering realistic configuration made of finite structures with embedded ABHs and viscoelastic layers, was addressed for beams in (Tang *et al.*, 2016; Tang and Cheng, 2017b). In these works, the Rayleigh-Ritz method has been used with Mexican hat wavelets to expand the flexural displacement field. In (O'Boy and Krylov, 2016), the Rayleigh-Ritz framework has been applied with the use of trigonometric functions to expand the ABH plate bending displacements; this choice limited the extension of this analysis to high frequencies. In (Ma *et al.*, 2018), the performance at high frequencies was improved by using 2D-Daubechies wavelets, which unfortunately cannot be expressed in closed form, since recursive formulas are needed. Moreover, both Mexican hat and Daubechies wavelets are pron to singularities in the mass matrix, that needs to be addressed with special numerical methods. In order to avoid these numerical problems, the Gaussian expansion method (GEM) can be used to expand the bending variational field for beams. Expansions with Gaussian functions have been widely used in nuclear physics (see e.g., Hiyama *et al.*, 2003; Nakada, 2006), quantum chemistry (Baccarelli *et al.*, 2007) and also in acoustics (Cervenka and Bednarík, 2013). In (Deng *et al.*, 2019b), one dimensional Gaussians have been used to explore the benefits of passive constrained layers in ABH beams. This approach has been extended to two dimensions in (Deng *et al.*, 2019). Moreover, in (Deng *et al.*, 2021) the GEM is extended to deal with ABH phononic crystals on infinite plates.

The Transfer Matrix Method

The Transfer Matrix Method (TMM) has been widely used in many research fields in acoustics. It is historically linked to the study of mufflers (Munjal, 1987), but it has been applied also to the design of musical instruments (see e.g., Plitnik and Strong, 1979; Caussé *et al.*, 1984) and to articulatory speech synthesis (see Sondhi and Schroeter, 1987). In fact, the performance of a muffler can be obtained in terms of transfer matrix of the entire system. Transformation of classic state variables p and v (pressure and velocity) can be obtained via a transfer matrix (Munjal, 1987; Mechel, 2002). The downstream state variables (see index d in Fig. 1.5) can be related to the upstream

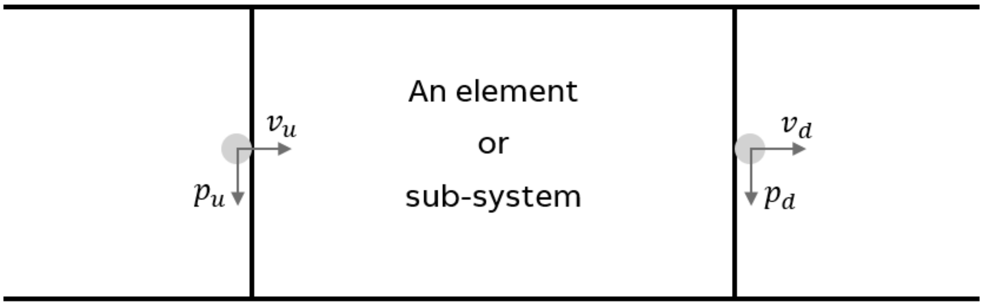

Figure 1.5: The basic setup for the application of the Transfer Matrix Method (TMM). The state variables v_d and p_d can be related to v_u and p_u by a matrix multiplication (figure inspired from (Mechel, 2002)).

ones (index u) via a matrix multiplication,

$$\begin{pmatrix} \mathrm{p_d} \\ \mathrm{v_d} \end{pmatrix} = \mathbf{T} \begin{pmatrix} \mathrm{p_u} \\ \mathrm{v_u} \end{pmatrix} \quad , \tag{1.14}$$

where **T** is the transfer matrix characterizing the element in Fig. 1.5. In (Mechel, 2002) many expression of transfer matrices are provided for different cases, such as sudden area changes, conical tubes and perforated ducts. In (Wang and Norris, 1995; Vemula *et al.*, 1996), exact solutions for the estimation of the wave field inside a medium, modeled as an inhomogeneous structural waveguide, were obtained by using the transfer matrix method. In (Li and Ding, 2018), the TMM has been applied to analyze the concentration of bending strain energy and kinetic energy of a one-dimensional wedge-shaped ABH beam. In (Li and Ding, 2019) the TMM is used to analyze the sound radiation of an ABH beam with a wedge-shaped edge, whose tip is truncated at a particular thickness.

The application of the TMM to an ABH in duct terminations is fairly new and it was initially explored in (Guasch *et al.*, 2017). In the cited work, ring plus cavity ensembles are considered as one element and acoustic pressure and velocity at the beginning and at the end of this structure are linked via a transfer matrix. The considered matrix is the results of a multiplication of three matrices taking into account the propagation in the ring, in the cavity and the influence of the cavity represented as a lumped element. By multiplying all the matrices corresponding to every ring plus cavity ensemble, the general behavior of the retarding structure can be computed. The influence of many parameters like the number of rings (see Fig. 1.6(a) and 1.6(b)) on

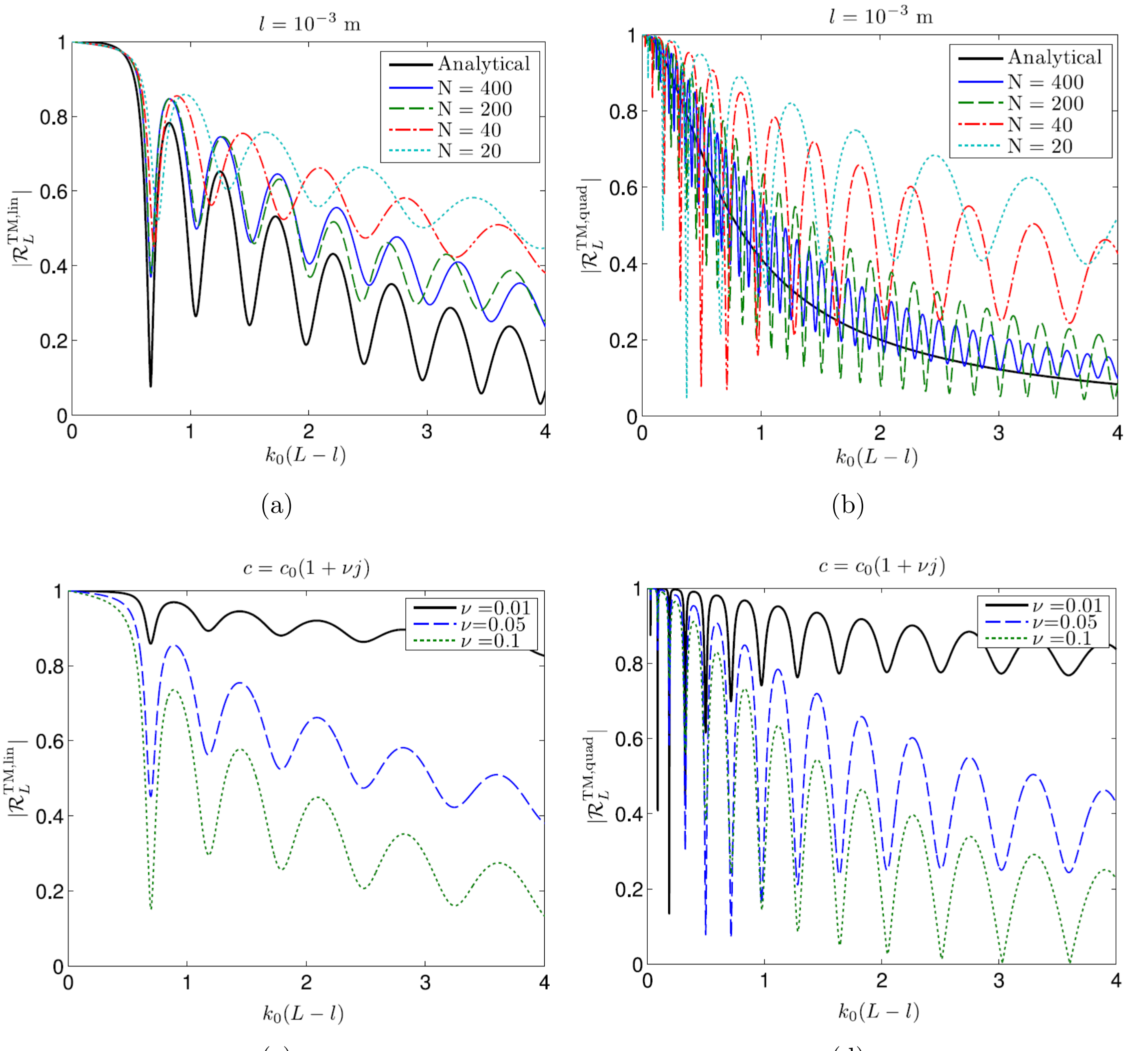

(a) (b)

(c) (d)

Figure 1.6: Influence of the number of rings on the reflection coefficient for linear (a) and quadratic (b) ABHs. Influence of damping with complex sound speed on the reflection coefficient for linear (c) and quadratic (d) cases (adapted from Guasch *et al.*, 2017).

the reflection coefficient of the ABH can be studied and the importance of damping in the absorption process is observed (Fig. 1.6(c) and 1.6(d)). Moreover, analytical expressions for reflection coefficients for linear and quadratic cases are provided, see also Section 3.4.

The Finite Element Method

The Finite Element Method (FEM) has been traditionally used to study the ABH effect in beams and plates and to make comparisons with experimental and analytical results. Finite element analysis have been carried out to study two dimensional ABH with damping layers (see, Conlon *et al.*, 2015; Feurtado and Conlon, 2016), periodic plates with tunneled ABHs (Tang and Cheng, 2019). In (Feurtado and Conlon, 2015), numerical models are applied to investigate reflection from ABHs in beams and it is showed that the reflection coefficient of bending waves follows the same behavior of the normalized wavenumber variation (which in this thesis will be referred to as smoothness condition, see Chapter 3 for more details). In (Hook *et al.*, 2019) a finite element model is developed to study the influence of many geometrical parameters on the reflection coefficient of a beam.

The finite element method has not been used very extensively to solve the ABH problem for acoustic waves in duct terminations. Very recently, some works have addressed this topic. In (Cervenka and Bednarík, 2022) the linearized Navier-Stokes equation (LNSE) are solved with FEM, taking into account thermoviscous losses, which allows a better understanding of the ABH effect. In fact, with the comparison between Fig. 1.7(a) and 1.7(b) it is showed that LNSE results are much more sensitive than the Helmholtz equation ones to geometrical parameters of the ABH. Therefore, LNSE should be used for quantitative studies of ABHs in ducts, which could lead to parametrical optimization. Moreover, in (Mousavi *et al.*, 2022) it is showed that pressure distribution inside ABH cavities is not uniform, leading to the appearance of cavity resonances. In addition, the roles of different loss mechanisms are analyzed (see Fig. 1.7(c) and 1.7(d)).

In Chapter 4, the Finite Element Method will be used to solve the wave equation in mixed form for waves propagating in a circular duct with an ABH termination at its end (Fig. 1.8). As previously commented, this will permits to obtain results much closer to the reality and to visualize the pressure distribution inside the duct. Moreover, the reflection coefficient of many different ABH terminations (influence of power-law profile, number of rings and absorption coefficient at walls will be considered) will be computed, thanks to a numerical adaptation of the two-microphone transfer function (TMTF) method (see Arnela and Guasch, 2013).

Finally, some remarks need to be made about numerical issues related to FEM. It is well-known that the standard Galerkin approach to solve partial differential equations may undergo numerical instabilities. For example, the Galerkin weak form of the Helmholtz equation suffers from the so-called pollution error due to the fact that it becomes non-positive definite for large

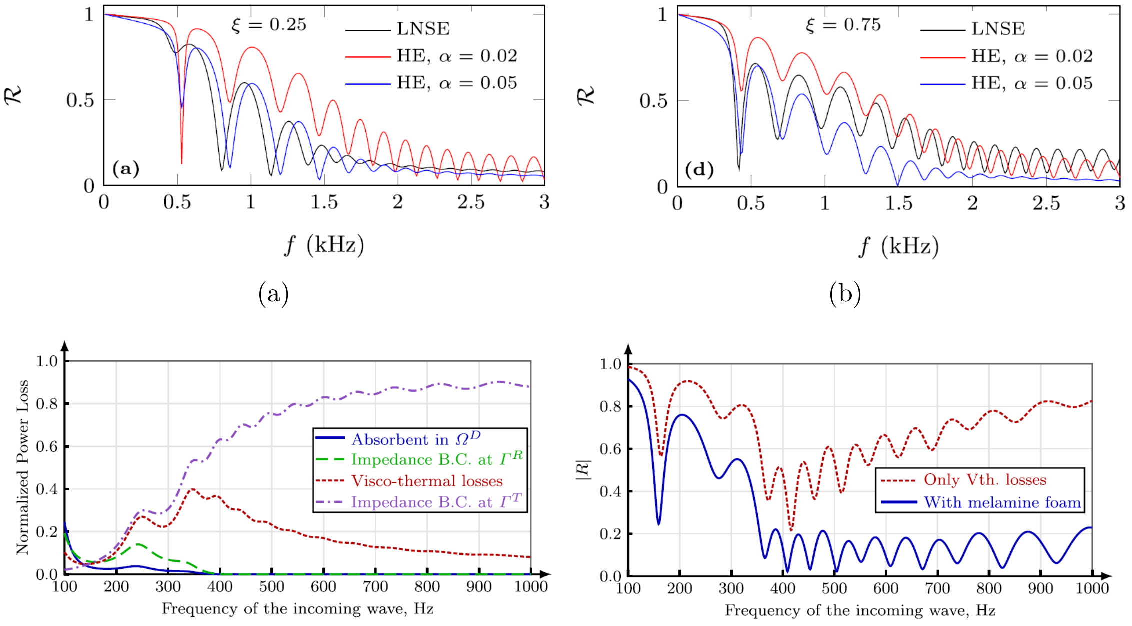

(a) (b)

(c) (d)

Figure 1.7: Comparison between reflection coefficients computed via Linearized Navier-Stokes Equations (LNSE) or Helmholtz Equation (HE) for a cavity width of 0.25m (a) and 0.75m (b) (Cervenka and Bednarík, 2022). The normalized power loss of all loss mechanisms (c) and magnitude of the reflection coefficient for two cases: only visco-thermal losses considered and layer of melamine foam added at the end of each cavity (outer tube) (Mousavi *et al.*, 2022).

wavenumbers, while the wave equation in mixed form must be stabilized to use equal interpolation for both, the acoustic pressure and particle velocity (see Codina, 2008). In the past decades, several numerical strategies have been proposed and used to overcome these numerical instabilities. A major progress was the development of stabilized finite element methods based on the subgrid scale approach (Hughes, 1995; Hughes *et al.*, 1998). This method consists in splitting the problem unknowns into a large scale that can be solved by the finite element mesh, and a fine scale (the subgrid scale, or subscale) that can be modeled. Applications of this stabilizing technique with subgrid scales for the Navier-Stokes equations can be found e.g., in (Codina, 2002; Codina *et al.*, 2007; Bazilevs *et al.*, 2007). Moreover, the wave equation and the convected wave equation with applications to aeroacoustics have been solved through stabilized finite element method with subscales (see e.g., Codina, 2008; Guasch and Codina, 2007). Finally, the same stabilization technique has been applied in acoustics for diphthongs production (see

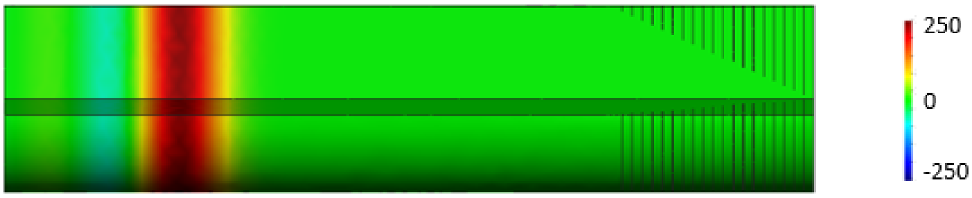

(a) $t = 0.0025$ s

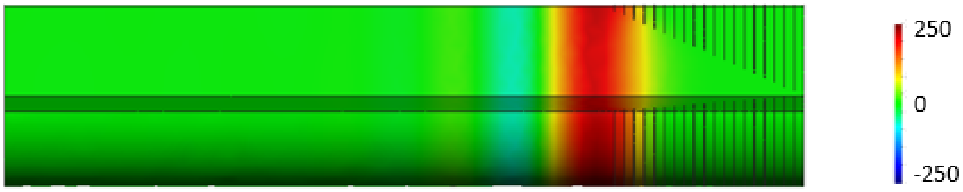

(b) $t = 0.005$ s

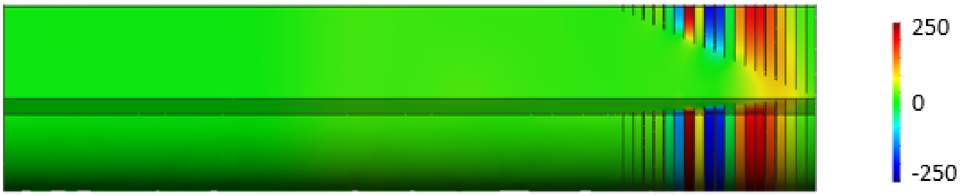

(c) $t = 0.0075$ s

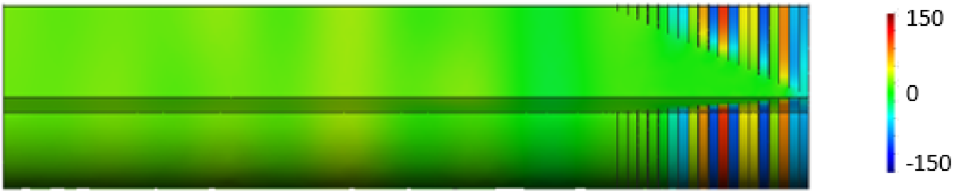

(d) $t = 0.0125$ s

Figure 1.8: Wave propagation and pressure distribution inside ABH cavities along time. Reflection can be appreciated in yellow in (d). See Chapter 4 for more details.

Guasch *et al.*, 2014; Guasch *et al.*, 2016; Arnela, 2015). Stabilization will be used throughout Chapter 4 whenever necessary.

1.2.5 Experimental results

The goal of the first experimental studies of the ABH effect in beams was the measurements of point mobility and the comparison between structures with and without ABHs. In (Krylov and Winward, 2007), a steel plate with a quadratic wedge is considered and differences between undamped and damped (via a strip of absorbing layer covering one edge) configurations are analyzed.

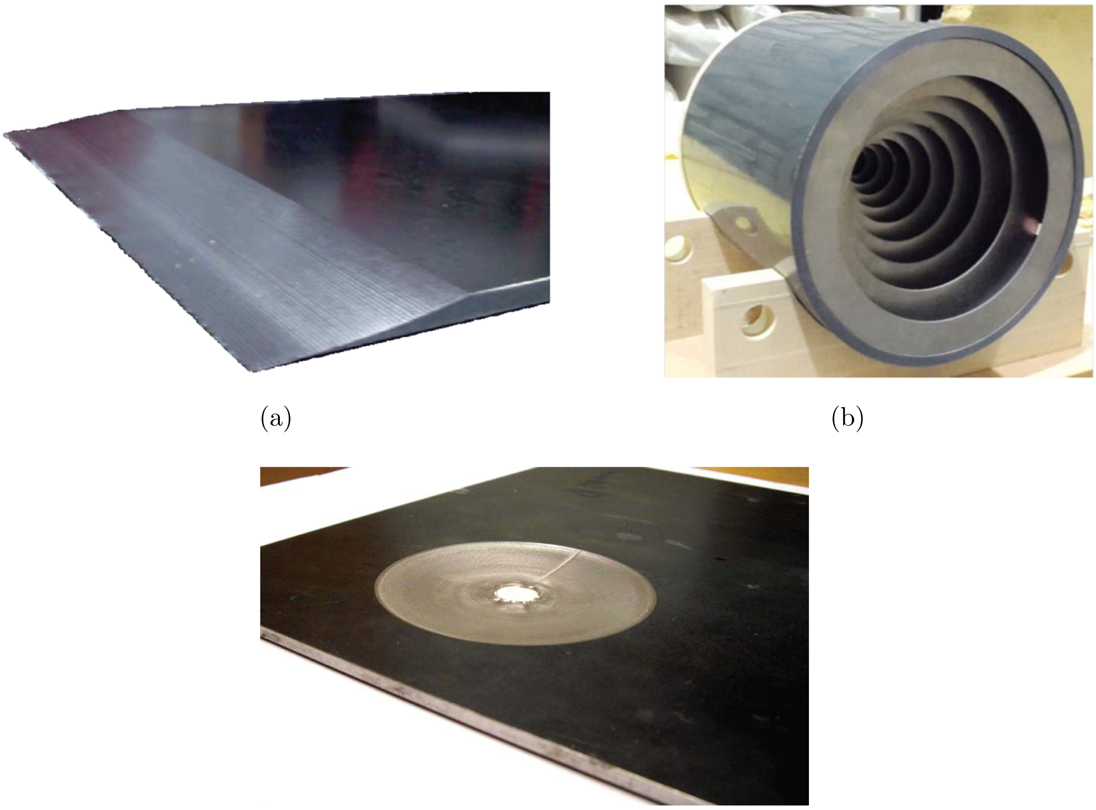
(a) (b)

(c)

Figure 1.9: (a) A rectangular plate with a power-lae profiled wedge, (b) practical realization of a quadratic ABH for a duct termination, (c) plate with a two-dimensional ABH realized through a circular indentation with a power-law profile.

In (Georgiev *et al.*, 2011; Bowyer *et al.*, 2013) the same comparison is carried out for tapered indentations of power-law profile, whose center was covered by a small quantity of absorbing material

Analytical and numerical methods described in previous sections are devoted to a better comprehension of the ABH effect for acoustic waves in ducts. In fact, with a good knowledge of the phenomenon, some particular and concrete configuration can be selected for manufacturing and experimental studies. The first experiments for ABHs in duct terminations were carried out in (El Ouahabi *et al.*, 2015; El Ouahabi *et al.*, 2015**b**). Here, linear and quadratic ABH termination were considered and their performance is studied by experimental measures of the reflection coefficient with the two microphone transfer function method. Moreover, damping materials are placed at the end of the waveguide, with the purpose of mitigating the effect of the truncation of the power-law profile. This choice was made by following analogous methods for structural ABHs, which consist in adding damping material at the thin part of the domain to reduce the truncation error. Quite surprisingly, it was found that the addition of damping has very little effect on the calculated reflection coefficients, while both configurations showed an agreement with the theory provided in (Mironov and Pislyakov, 2002) (see Fig. 1.10(a) and 1.10(b)). In (Mironov and Pislyakov, 2020) an experimental study showed that adding different damping materials to the last cavities has an influence on the reflection coefficients only at low frequencies (see Fig. 1.10(c) and 1.10(d)). In (Mi *et al.*, 2021), experimental results of a quadratic ABH based on the impedance tube measurement are presented and it is showed that both sound reflection and transmission are reduced (see Fig. 1.10(e) and 1.10(f)). Moreover, in (Bravo and Maury, 2023) a duct silencer is optimized with the achievement of the acoustic black hole effect and this can inspire new mufflers designs. Finally, in (Umnova, 2023) it is shown that ABHs with graded properties can be described as multi-resonant absorbers and a satisfactory agreement between semi-analytical, FEM and experimental results is found.

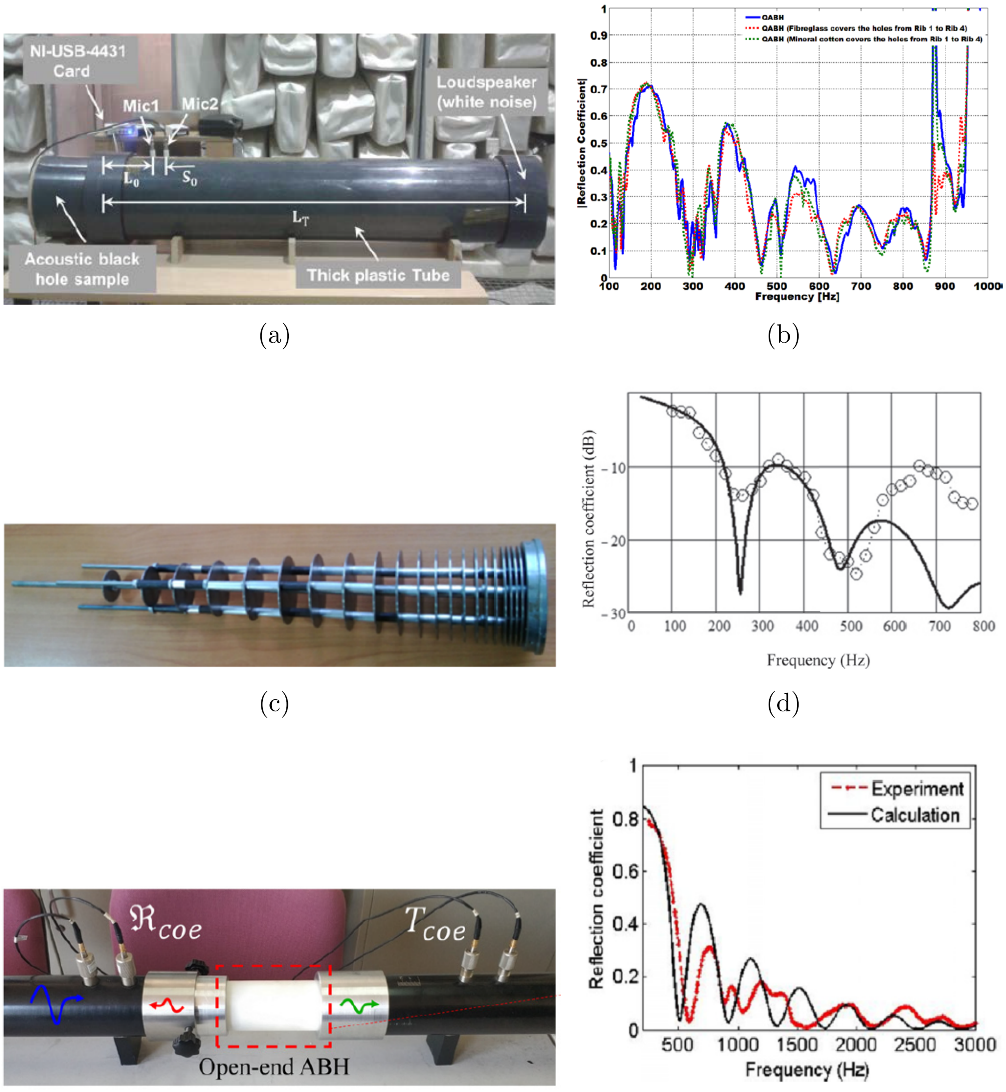

(a) (b)

(c) (d)

(e) (f)

Figure 1.10: (a) Experimental setup and (b) corresponding results for a quadratic ABH whose last ring holes are covered by different materials (El Ouahabi *et al.*, 2015), (c) experimental setup and (d) corresponding result for a quadratic ABH whose last cavities are filled with materials with increasing density (Mironov and Pislyakov, 2020), (e) experimental setup and (f) corresponding results for an open-end ABH (Mi *et al.*, 2021).

1.3 Aims of the thesis

The main purpose of this thesis is to provide a semi-analytical and a numerical characterization of acoustic black holes in duct terminations. As for the semi-analytical part, an expansion in terms of Gaussian functions is used to solve the Helmholtz equation. Moreover, the concept of metafluid will be used to prove the converge of analytical solutions to the numerical solutions. The numerical part of the work will be carried out through very different method: the Transfer Matrix Method, for characterizing ABHs with low computational cost and comparing with analytical results, and the Finite Element Method, which allows to simulate and the to visualize waves propagation inside the ABH in a more precise way.

The specific main goals of this work can be listed as follows:

1. Propose a theoretical framework to study the performance of theoretical ABHs via the variational formulation of the problem and its solution through Gaussian basis expansion of the unknown.
2. Analyze the performance of the theoretical ABH.
3. Show with a rigorous proof that the transfer matrix solution is consistent and formally tends to the solution of the continuous problem.
4. Study the effect of many parameters (i.e number of rings and absorption at walls) on the ABH performance, represented by the reflection coefficient computed via FEM results.
5. Provide a preliminary explanation of the role of ABH cavities in the absorption process.

These objectives are organized as described in the following Section 1.4.

1.4 Thesis organization

This thesis is organized as follows:

- In Chapter 2 a theoretical framework to analyze the performance of ABHs is presented through a Gaussian discretization of the variational formulation of the ABH problem. The solutions obtained with the proposed strategy are validated against FEM results. Finally, alternative ABH profiles to the power-law are studied.
- In Chapter 3 it is proved that the TMM solutions tend to the solution of the differential ABH equation, for an ABH of any order, when the

number of rings and cavities goes to infinity. This will be done by recurring to the concept of a metafluid and by identifying an analogy with the ABH configuration. Finally, numerical results comparing analytical and TMM reflection coefficients are presented

- In Chapter 4 preliminary FEM results of the ABH effect in duct terminations are presented. The performance of different ABHs is evaluated with the calculation of the corresponding reflection coefficient, which is computed by means of a numerical adaptation of the two-microphone transfer function method (TMTF). Finally, many numerical results show the influence on the ABH performance of many parameters such as number of rings, ABH order, and absorption at walls.

Conclusions and future research lines are finally exposed in Chapter 5.

Chapter 2

Solution and analysis of theoretical acoustic black holes in duct terminations by Gaussian functions

In this chapter a rigorous analysis of theoretical black holes in duct termination will be presented. The acoustic black hole (ABH) made of rings separated by cavities whose inner radii decrease by following a power-law will be considered. Therefore, the singularity at the ABH termination will be removed by considering a rigid residual surface, analogously to the residual thickness usually considered for ABHs in beams and plates. As a first step of the theoretical framework proposed, the generalized Webster equation for the acoustic pressure inside the ABH will be transformed into a Helmholtz equation with spatially varying wavenumber. Then, the variational formulation of the Helmholtz equation will be derived and solved by expanding the unknown scaled pressure with a basis of Gaussian functions. With the same method, an eigenvalue problem that provides the ABHs modes will be presented. The modal decomposition will show that the ABH modes are very sensitive to changes in the residual radius and damping, clarifying the occurrence of oscillations in the reflection coefficient and input admittance at different frequencies. The results obtained with the aforementioned theoretical approach will be validated against FEM results and an extensive parametric analysis of the reflection coefficient will be carried out. Finally, alternative profiles to power law will be investigated and reflection coefficients values similar to the classical ABH will be showed.

Concerning implementation aspects, the FEM model considered in this chapter has been built using the Comsol 1D *Pressure Acoustic* module.

This chapter is mainly based on the following works:

- Jie Deng, Oriol Guasch and Davide Ghilardi (2023), "Solution and analysis of theoretical sonic black holes in duct terminations", Journal of Sound and Vibration, Submitted.
- Jie Deng, Oriol Guasch and Davide Ghilardi (2023), "Gaussian series for sonic black holes in duct terminations", Forum Acusticum 2023, Submitted.

2.1 Introduction

Aerial acoustic black holes (ABHs), simply known as ABHs in duct terminations, were proposed in (Mironov and Pislyakov, 2002), several years after their equivalents for beams and plates (see Mironov 1988; Pelat *et al.*, 2020). While various designs for the latter have been proposed, only a few ABHs have been developed to date. The most well-known of these is the design suggested in (Mironov and Pislyakov, 2002), which comprises a series of rings separated by air cavities, with an inner radius profile that decays according to a power-law. In the case of a large number of rings and small cavities, wave propagation inside the ABH can be described by a generalized Webster equation, and thermoviscous losses can be considered by means of a complex speed of sound. As an acoustic wave enters an ABH, it slows down, while its amplitude grows and its wavelength decreases towards the termination of the ABH. Analytically, it has been shown that for an ideal linear ABH (Mironov and Pislyakov, 2002) and a quadratic one (Guasch *et al.*, 2017), a wave travelling within the ABH will never reach its end, and therefore, no reflection can take place. Recently, the classical ring-cavity ABH design has inspired new slow-sound designs consisting of truss lattices that can be built using additive manufacturing techniques (Chua *et al.*, 2023). Alternatively, one might take advantage of the fact that the generalized Webster equation governing acoustic plane wave propagation in the ring/cavity ABH is identical to the wave equation for a metafluid with a power-law varying density (Guasch *et al.*, 2020). An ABH based on this equivalence was recently tested in (Mironov and Pislyakov, 2020). It is important to differentiate between theoretical or ideal ABHs, which can typically be described using partial differential equations at the continuum level, and their practical realizations. While most research has focused on the latter, this chapter specifically addresses the former, as it has been done in (Karlos *et al.*, 2019; Lee and Jeon, 2019) for ABH beams. In fact, exploring a deeper understanding of theoretical ABHs could aid in their designs for practical applications. To improve our comprehension of theoretical ABHs, the generalized Webster equation governing acoustic wave propagation inside the ABH will be transformed into a Helmholtz equation with spatially varying wavenumber for a new locally scaled pressure (Guasch *et al.*, 2020; Robins, 1991; Brekhovskikh, 2012). It is worth noting that the ABH in (Mironov and Pislyakov, 2002) exhibits a singularity at the origin (that is, its termination). In that pioneering work, a length imperfection was introduced to terminate the waveguide before reaching the origin of the ABH. However, in this chapter, the problem is formulated more naturally by considering a rigid residual surface (with a corresponding residual radius) at the termination point of the ABH. This approach will be shown to be analogous to the use of residual thickness in ABH beams and plates (Krylov and Tilman, 2004; Krylov, 2004; O'Boy and Krylov, 2011; Deng *et al.*, 2019; Deng *et al.*, 2019b). In order to solve the Helmholtz equation with spatially varying wavenumber, a high-order WKB (Wentzel, Kramers and Brillouin) expansion could be used, as done in (Karlos *et al.*, 2019). But, dealing with high-order terms of the WKB expansion can be difficult to handle, because eventually the series tends to diverge. Another suitable option could be the more robust Bremmer series for the equation at hand (Bremmer, 1951; Bellman and Kalaba, 1959; Atkinson, 1960; Doc *et al.*, 2016). Nevertheless, this case requires the evaluation of nontrivial numerical integrals to derive the terms of the series and the imposition of complex boundary conditions on it. Hence, a simpler method to solve the Helmholtz equation has been chosen. Initially, its variational formulation is derived and the relevant boundary conditions are imposed, which include zero acoustic particle velocity at the residual surface and pressure and velocity continuity at the entrance of the ABH. Then, a Gaussian functions basis is used to expand the scaled pressure, which becomes more refined as it approaches the end of the ABH. Substituting this into the weak form results in an algebraic system to calculate the expansion coefficients. Also, a similar approach is followed to derive an eigenvalue problem for computing the ABH modes. Thereafter, the suggested theoretical approach is validated against FEM simulations. Various aspects of the ABH are analyzed, beginning with the changes in sound speed and wavenumber within it, for both normal and scaled pressure (which is the normal acoustic pressure multiplied by the square root of the section of the waveguide, a change of variable that will be crucial for following developments). Then, a modal analysis is performed to observe how the mode shapes and their concentration within the ABH are influenced by damping and the residual radius. This analysis provides insights into the formation and disappearance of peaks and dips in input impedance and reflection coefficient of the ABH, which can be helpful for the design process. Lastly, beside the power-law, other options for the ABH profile are investigated: analytical functions such as power-cosine, exponential and Gaussian profiles will be considered, as was done for beams in (Karlos *et al.*, 2019).

This chapter is organized as follows. In Section 2.2 the theoretical framework is presented and several steps are followed. The Helmholtz equation for the scaled pressure is derived and the ABH problem is formulated. The variational formulation of the problem is presented, the discretization is carried out by introducing the Gaussian basis and the discrete variational form of the equation is derived. Then, Section 2.2 concludes with introducing the eigenvalue problem that permits to compute the ABH modes and to perform a modal expansion of the acoustic pressure. In Section 2.3, numerical results are presented. First, the proposed solution strategy is validated against FEM simulations. Second, the variations of the speed of sound and the wavenumber inside the ABH are shown and a modal decomposition for the acoustic pressure is introduced. Third, an analysis of the influence of various parameters on the reflection coefficient and input admittance is performed and alternative profiles are discussed. Conclusions finally close the chapter in Section 2.4.

2.2 Theoretical framework

2.2.1 Generalized Webster equation in waveguides as a Helmholtz equation in an inhomogeneous medium

Prior to formulating and solving the exact problem of a wave travelling in a radially symmetric duct, impinging on and propagating inside an acoustic black hole (ABH) retarding guide, some preliminary results need to be derived and presented. Firstly, it is necessary to show that the generalized Webster equation, which describes the propagation of plane waves in a waveguide of varying radius and wall impedance (not necessarily an ABH), can be expressed as a problem of wave propagation in an inhomogeneous medium, characterized by a Helmholtz-type equation with spatially varying wavenumber. It has to be noted that since the irreducible form of the equations will be taken into account, the time dependent term $\exp(\mathrm{j}\omega t)$ will be omitted in all expressions. The starting point is the generalized Webster equation (Eq. (4) in (Mironov and Pislyakov, 2002)), for the case of plane wave propagation in a radially symmetric waveguide with section $S(x)$, local radius $r(x)$, and wall impedance $Y(x)$. The equation reads,

$$\frac{\mathrm{d}^2\hat{p}}{\mathrm{d}x^2} + \frac{\mathrm{d}}{\mathrm{d}x}\big(\ln S\big)\frac{\mathrm{d}\hat{p}}{\mathrm{d}x} + \Big[k_0^2 + \mathrm{j}Z_0\frac{2Y}{r}k_0\Big]\hat{p} = 0, \tag{2.1}$$

where $\hat{p}(x)$ stands for the acoustic pressure, $k_0 = \omega/c_0$ for the wavenumber, ω is the radial frequency, c_0 the speed of sound and $\mathrm{j} = \sqrt{-1}$. $Z_0 = \rho_0 c_0$ is the air characteristic impedance with ρ_0 denoting the air density. The complex wavenumber $k_Y(x)$, dependent on the impedance $Y(x)$, is defined such that

$$k_Y^2 \equiv k_0^2 + \mathrm{j}Z_0\frac{2Y}{r}k_0 \tag{2.2}$$

and some slight manipulations allow to rewrite Eq. (2.1) as

$$\frac{\mathrm{d}^2\hat{p}}{\mathrm{d}x^2} + \frac{S'}{S}\frac{\mathrm{d}\hat{p}}{\mathrm{d}x} + k_Y^2\hat{p} = 0, \tag{2.3}$$

where, for brevity, this notation is introduced: $S' \equiv \mathrm{d}S/\mathrm{d}x$. Taking into account that $S(S^{-1})' = -S'S^{-1}$ and introducing the change of variables $\phi = S^{1/2}\hat{p}$, Eq. (2.1) can be transformed into

$$-\frac{\mathrm{d}^2\phi}{\mathrm{d}x^2} - \kappa^2(x)\phi = 0, \tag{2.4}$$

which is a Helmholtz equation for the locally scaled acoustic pressure ϕ with spatially varying squared wavenumber given by,

$$\kappa^2 = k_Y^2 - \frac{1}{2}\frac{S''}{S} + \frac{1}{4}\frac{S'^2}{S^2}. \tag{2.5}$$

It has to be noted that, if the waveguide walls are rigid (i.e., $Y = 0$), $k_Y^2 = k_0^2$ and Eq. (2.1), Eq. (2.3) and Eq. (2.4) provide the original Webster equation.

Also, if the waveguide has constant section (i.e., $S' = 0$) then $\kappa^2 = k_Y^2 = k_0^2$ and the standard Helmholtz equation is recovered. Moreover, it needs to be underlined that Eq. (2.4) with wavenumber in Eq. (2.5) is very general and it can be applied to solve the generalized Webster equation in many different circumstances, when proper specification of the boundary conditions (BCs) and waveguide geometry are provided. However, in the following formulation ABHs will be considered and some simplifications for the wavenumber $\kappa^2(x)$ in Eq. (2.5) introduced. First, the lumped formula proposed for the wall admittance $Y(x)$ in (Mironov, 2002) (see also Guasch *et al.*, 2017) will be used,

$$Y(x) = -\mathrm{j}\frac{k_0}{Z_0}\frac{R^2 - r^2}{2r}, \tag{2.6}$$

which corresponds to the ideal realization of an ABH consisting of a large number of rings and cavities, when the thicknesses of the inner rings is negligible compared to that of the air cavities. Inserting Eq. (2.6) into Eq. (2.2) leads to a simplification of k_Y^2 to

$$k_Y^2 = k_0^2\frac{R^2}{r^2}. \tag{2.7}$$

On the other hand, the assumption of radial symmetry implies $S(x) = \pi r(x)^2$. The first and second derivatives of $S(x)$ are given by $S' = 2\pi r r'$ and $S'' = 2\pi(r')^2 + 2\pi r r''$. Substituting these expressions, together with Eq. (2.7), into Eq. (2.5), leads to

$$\kappa^2 = k_0^2\frac{R^2}{r^2} - \frac{r''}{r}, \tag{2.8}$$

which is a significant simplification of Eq. (2.5).

2.2.2 Formulation of the acoustic black hole problem in a finite duct termination

Now, attention is given to the problem of having an ABH with radial symmetry at the end of a uniform duct (see Fig. 2.1). To keep the notation used in previous works (see Mironov and Pislyakov, 2002; Guasch *et al.*, 2017; Guasch *et al.*, 2020), an incident plane wave that enters an ABH of length L and cross section $S(x)$ from the left is considered. The acoustic pressure

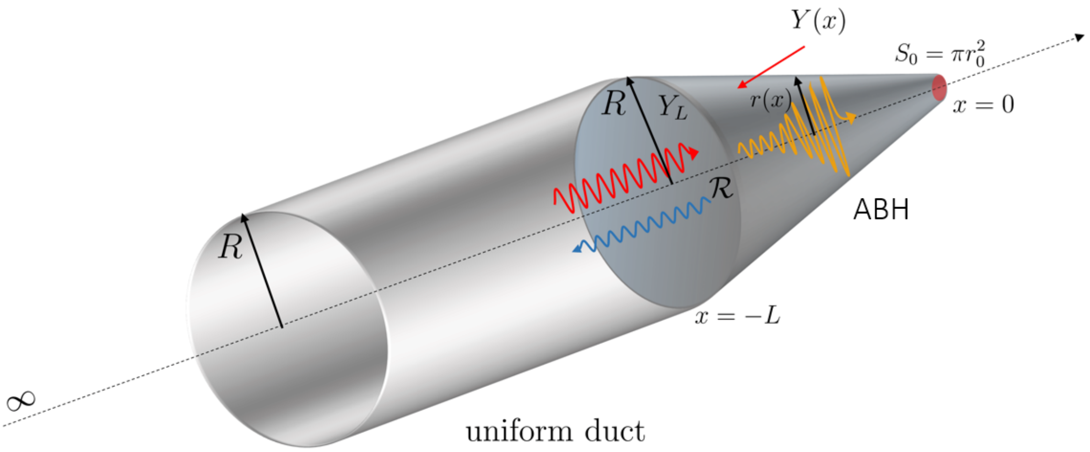

Figure 2.1: Schematic of the ABH problem. A wave propagating inside the uniform duct impinges on an ABH of length L, which is characterized by a small reflection coefficient $\mathcal{R}$ with corresponding inlet admittance Y_L. The wave within the ABH slows down, while its amplitude grows and its wavelength diminishes as it approaches the termination of the ABH. The profile of the ABH is defined by its radius $r(x)$, which varies from that of the uniform duct at the input, R, to the residual r_0. The residual cross-section $S_0 = \pi r_0^2$ is considered to be perfectly rigid. The ABH has a wall admittance $Y(x)$.

distribution inside the ABH and the reflection coefficient, $\mathcal{R}$, at its entrance (among other issues to be detailed in subsequent sections) are the magnitudes of interest. For brevity, the notation $S_L \equiv S(-L)$ is introduced to denote the constant cross section of the uniform duct in front of the ABH and $R \equiv r(-L)$ to denote its radius. Likewise, $S_0 \equiv S(0)$ is the residual cross section at the ABH termination and $r_0 \equiv r(0)$ its corresponding residual radius.

The problem to be addressed can be formulated as finding $\phi(x)$ such that,

$$-\frac{\mathrm{d}^2\phi}{\mathrm{d}x^2} - k_0^2\phi = 0, \quad \forall\, x \in (-\infty, -L] \tag{2.9a}$$

$$-\frac{\mathrm{d}^2\phi}{\mathrm{d}x^2} - \kappa^2(x)\phi = 0, \quad \forall\, x \in [-L, 0] \tag{2.9b}$$

where $\kappa^2(x)$ is given by Eq. (2.8). The solution to Eq. (2.9a) is

$$\phi(x) = \mathrm{e}^{-\mathrm{j}k_0 x} + \mathcal{R}\mathrm{e}^{\mathrm{j}k_0 x} \quad \forall\, x \in (-\infty, -L], \tag{2.10}$$

where $\mathcal{R}$ is the unknown reflection coefficient at $x = -L$. Eqs. (2.9a) and (2.9b) must be complemented with a boundary condition at $x = 0$ (we assume S_0 to be perfectly rigid) and continuity conditions for the acoustic pressure and particle velocity at $x = -L$. The imposition of a rigid wall at $x = 0$ implies $\mathrm{d}\hat{p}(0)/\mathrm{d}x = 0$, so that

$$\frac{\mathrm{d}\phi}{\mathrm{d}x}(0) - \frac{S'}{2S}(0)\phi(0) = 0. \tag{2.11}$$

On the other hand, the pressure and velocity continuity at $x = -L$ requires, respectively,

$$\phi(-L) = \mathrm{e}^{\mathrm{j}k_0 L} + \mathcal{R}\mathrm{e}^{-\mathrm{j}k_0 L}, \tag{2.12a}$$

$$\frac{\mathrm{d}}{\mathrm{d}x}\phi(-L) - \frac{S'}{2S}(-L)\phi(-L) = -\mathrm{j}k_0\left(\mathrm{e}^{\mathrm{j}k_0 L} - \mathcal{R}\mathrm{e}^{-\mathrm{j}k_0 L}\right). \tag{2.12b}$$

In order to find the solution to Eq. (2.9b), its variational formulation will be derived and then solved by means of a basis of Gaussian functions. As a concluding remark for this section, it has to be noted that Eq. (2.3) is singular at $x = 0$ for an ideal ABH for which $S(0) = 0$. In (Mironov and Pislyakov, 2002) this singularity was avoided by introducing a small length imperfection l so that the ABH ends slightly before reaching the origin. In the current formulation, this problem is avoided in a more natural way by assuming a rigid residual cross-section $S(0) = S_0$ at $x = 0$, with residual radius r_0. The effects of r_0 on the ABH performance will be discussed in detail in later sections.

2.2.3 Variational formulation of the Helmholtz equation for the scaled pressure inside a ABH

The usual technique to find a variational form for Eq. (2.9b) consists in multiplying the equation by a test function $\psi^*(x)$ (where $*$ denotes complex conjugate) and integrating over the domain $[-L, 0]$. Then the term containing the second derivative of the unknown scaled acoustic pressure $\phi(x)$ is integrated by parts and this allows one to arrive at,

$$\int_{-L}^{0} \frac{\mathrm{d}\psi^*}{\mathrm{d}x}\frac{\mathrm{d}\phi}{\mathrm{d}x}\mathrm{d}x - \int_{-L}^{0} \kappa^2(x)\psi^*\phi\mathrm{d}x - \psi^*\frac{\mathrm{d}\phi}{\mathrm{d}x}\Big|_{-L}^{0} = 0. \tag{2.13}$$

With respect to the boundary conditions in the third term, Eq. (2.11) implies that

$$\frac{\mathrm{d}\phi}{\mathrm{d}x}(0) = \frac{S'}{2S}(0)\phi(0), \tag{2.14}$$

while Eq. (2.12a) can be solved for $\mathcal{R}$, i.e.,

$$\mathcal{R} = \mathrm{e}^{\mathrm{j}k_0 L}\phi(-L) - \mathrm{e}^{2\mathrm{j}k_0 L}, \tag{2.15}$$

and substitute it into Eq. (2.12b) to get

$$\frac{\mathrm{d}\phi}{\mathrm{d}x}(-L) = \mathrm{j}k_0[\phi(-L) - 2\mathrm{e}^{\mathrm{j}k_0 L}] + \frac{S'}{2S}(-L)\phi(-L). \tag{2.16}$$

Inserting $\frac{\mathrm{d}\phi}{\mathrm{d}x}(0)$ and $\frac{\mathrm{d}\phi}{\mathrm{d}x}(-L)$ in Eq. (2.13) provides the final expression for the variational form of the problem,

$$\begin{aligned}
&\int_{-L}^{0} \frac{\mathrm{d}\psi^*}{\mathrm{d}x}\frac{\mathrm{d}\phi}{\mathrm{d}x}\mathrm{d}x - \int_{-L}^{0} \kappa^2(x)\psi^*\phi\mathrm{d}x + \mathrm{j}k_0\psi^*(-L)\phi(-L) + \\
&\frac{S'}{2S}(-L)\psi^*(-L)\phi(-L) - \frac{S'}{2S}(0)\psi^*(0)\phi(0) \\
&= 2\mathrm{j}k_0\mathrm{e}^{\mathrm{j}k_0 L}\psi^*(-L).
\end{aligned} \tag{2.17}$$

2.2.4 Gaussian expansion of the locally scaled acoustic pressure and test function

Now, Eq. (2.17) will be discretized and solved by expanding the unknown locally scaled pressure $\phi(x)$ and the test function $\psi^*(x)$ in terms of Gaussian functions like in (Deng, 2019; Deng, 2019a), but with some variations detailed below. The procedure for $\phi(x)$ will be developed, as the one for $\psi^*(x)$ will be the same. Consider

$$\phi(x) = \sum_{i=1}^{n} a_i\varphi_i(x), \tag{2.18}$$

where a_i are coefficients to be determined and $\varphi_i(x)$ are the Gaussian functions of compact support in a domain Ω_i, given by

$$\varphi_i(x) = \begin{cases} \exp\left\{-\frac{[2^{j(x_i)}(x-x_i)]^2}{2}\right\} & \forall x \in \Omega_i = [-8\sigma_i, 8\sigma_i], \\ 0 & \forall x \in (-\infty, -8\sigma_i) \cup (8\sigma_i, +\infty). \end{cases} \tag{2.19}$$

Note that $\varphi_i(x)$ has unit amplitude, is centered at x_i (which can be identified as a translating parameter) and has standard deviation $\sigma_i = 1/2^{j(x_i)}$. Here $j(x_i)$ is identified as the scaling parameter which depends on x_i to guarantee a higher accuracy of $\phi(x)$ (this was not contemplated in the Gaussian basis of

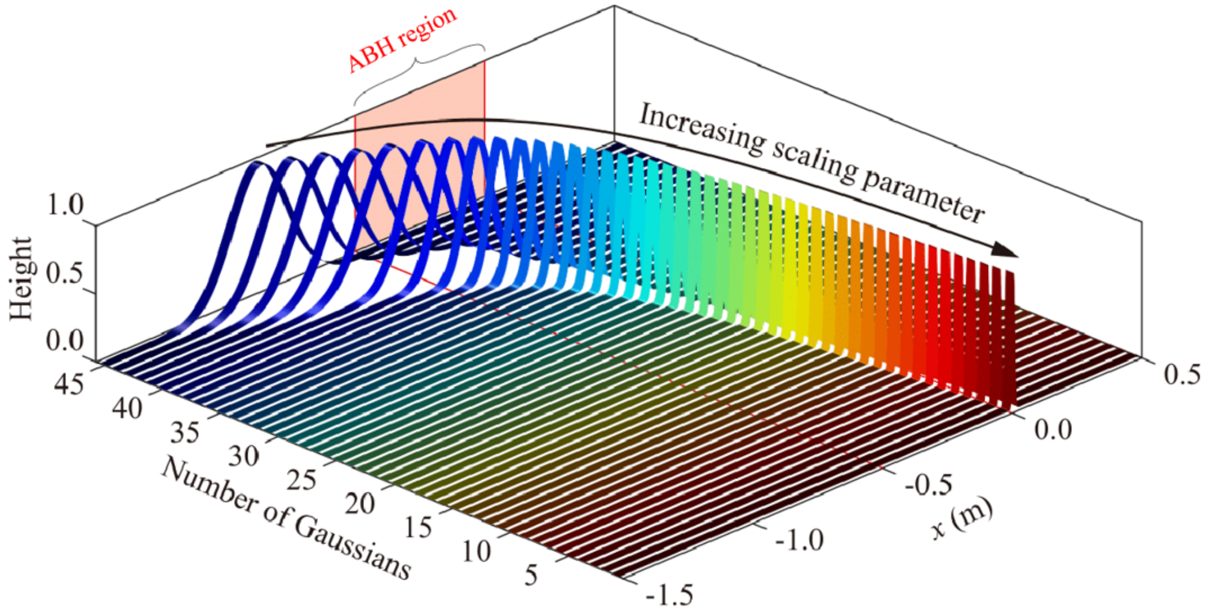

Figure 2.2: Gaussian basis functions distributed along the ABH termination.

(Deng, 2019a)). Given that the wavelength of the wave propagating inside an ABH decreases when approaching the termination (see Fig. 2.2) it is convenient that the Gaussian functions become sharper there. To be specific, $\Omega_i/2$ must be less than the local wavelength, $\lambda(x_i) = 2\pi/k(x_i)$, (i.e., $\Omega_i \leq \lambda(x_i)$), which implies $j(x_i) \geq 2 + \log_2[k(x_i)/\pi]$. In the standard wavelet transform, the scaling parameter j, not to be confused with the imaginary unit j, is constant and is defined such that the distance between the centers of two successive wavelets satisfies the relation $x_{i+1} - x_i = -1/2^j$. In the current case, we keep the similar condition $x_{i+1} - x_i = -\alpha/2^{j(x_i)}$ where $\alpha \in (0, 1]$ is a safety coefficient that improves the stability of the method and, as already mentioned, j is no longer constant but depends on x_i. Therefore, to build the basis of Gaussian functions for the ABH the following procedure is used. By starting from the ABH termination, the first Gaussian is centered at $x_1 = 0$ and prescribe $j(x_1)$ considering the condition induced by the local wavenumber, $k(x_1)$, introduced above. The second function of the basis is chosen to have its center at $x_2 = x_1 - \Delta x_1$, with $\Delta x_1 = \alpha/2^{j(x_1)}$. The third Gaussian is located at $x_3 = x_2 - \Delta x_2$ with $\Delta x_2 = \alpha/2^{j(x_2)}$ and so on. In general, the $i+1$ Gaussian $\varphi_{i+1}(x)$ will be centered at $x_{i+1} = x_i - \Delta x_i$, with $\Delta x_i = \alpha/2^{j(x_i)}$. The iteration ends when $x_i < -L$. To complete the basis for proper resolution at the end points, $x = \{-L, 0\}$, the first and last Gaussians are repeated four times with constant translation and scaling parameters. The final basis is represented in Fig. 2.2. For the developments in the following sections it is advisable to arrange all the unknown coefficients a_i in a single vector $\boldsymbol{A}$ and all the Gaussian basis functions $\varphi_i(x)$ in a vector $\boldsymbol{\varphi}$, so that Eq. (2.18) can be rewritten in a compact form as

$$\phi(x) = \boldsymbol{\varphi}^\top(x)\boldsymbol{A}. \tag{2.20}$$

2.2.5 Discretization and solution of the variational problem in terms of Gaussian functions

Consider the expansions $\phi(x) = \boldsymbol{\varphi}^\top(x)\boldsymbol{A}$ and $\psi^*(x) = [\boldsymbol{\varphi}^\top(x)\boldsymbol{B}]^{\mathrm{H}} = \boldsymbol{B}^{\mathrm{H}}\boldsymbol{\varphi}$, where H denotes the Hermitian. Substitution into Eq. (2.17) provides the quadratic form,

$$\begin{aligned}
&\boldsymbol{B}^{\mathrm{H}}\left[\int_{-L}^{0}\frac{\mathrm{d}\boldsymbol{\varphi}}{\mathrm{d}x}\frac{\mathrm{d}\boldsymbol{\varphi}^\top}{\mathrm{d}x}\mathrm{d}x\right]\boldsymbol{A} - \boldsymbol{B}^{\mathrm{H}}\left[\int_{-L}^{0}\kappa^2(x)\boldsymbol{\varphi}\boldsymbol{\varphi}^\top\mathrm{d}x\right]\boldsymbol{A}\\
&+\boldsymbol{B}^{\mathrm{H}}\left[\mathrm{j}k_0\boldsymbol{\varphi}(-L)\boldsymbol{\varphi}^\top(-L) + \frac{S'}{2S}(-L)\boldsymbol{\varphi}(-L)\boldsymbol{\varphi}^\top(-L) - \frac{S'}{2S}(0)\boldsymbol{\varphi}(0)\boldsymbol{\varphi}^\top(0)\right]\boldsymbol{A}\\
&= 2\mathrm{j}k_0\mathrm{e}^{\mathrm{j}k_0L}\boldsymbol{B}^{\mathrm{H}}\boldsymbol{\varphi}(-L),
\end{aligned} \tag{2.21}$$

and dropping $\boldsymbol{B}^{\mathrm{H}}$ the algebraic matrix system is obtained,

$$(\boldsymbol{K} - \boldsymbol{M} + \boldsymbol{C}_{\mathrm{BC}})\,\boldsymbol{A} = \boldsymbol{F}, \tag{2.22}$$

where the subscript BC stands for "boundary conditions".
The matrices $\boldsymbol{M}$, $\boldsymbol{K}$ and $\boldsymbol{C}_{\mathrm{BC}}$ are given by

$$\boldsymbol{K} := \int_{-L}^{0}\frac{\mathrm{d}\boldsymbol{\varphi}}{\mathrm{d}x}\frac{\mathrm{d}\boldsymbol{\varphi}^\top}{\mathrm{d}x}\mathrm{d}x, \tag{2.23a}$$

$$\boldsymbol{M} := \int_{-L}^{0}\kappa^2(x)\boldsymbol{\varphi}\boldsymbol{\varphi}^\top\mathrm{d}x, \tag{2.23b}$$

$$\begin{aligned}
\boldsymbol{C}_{\mathrm{BC}} &:= \mathrm{j}\frac{\omega}{c_0}\boldsymbol{\varphi}(-L)\boldsymbol{\varphi}^\top(-L) + \frac{S'}{2S}(-L)\boldsymbol{\varphi}(-L)\boldsymbol{\varphi}^\top(-L) - \frac{S'}{2S}(0)\boldsymbol{\varphi}(0)\boldsymbol{\varphi}^\top(0)\\
&=: \mathrm{j}\omega\boldsymbol{C}_{\mathrm{BCI}} + \boldsymbol{C}_{\mathrm{BCII}},
\end{aligned} \tag{2.23c}$$

where $\boldsymbol{C}_{\mathrm{BCI}}$ and $\boldsymbol{C}_{\mathrm{BCII}}$ have been defined for convenience in subsequent developments. The force vector $\boldsymbol{F}$ in Eq. (2.22) is

$$\boldsymbol{F} := 2\mathrm{j}k_0\mathrm{e}^{\mathrm{j}k_0L}\boldsymbol{\varphi}(-L). \tag{2.23d}$$

The solution of Eq. (2.22) provides the coefficient vector $\boldsymbol{A}$ from which the scaled pressure $\phi(x) = \boldsymbol{\varphi}^\top(x)\boldsymbol{A}$ inside the ABH can be calculated, as well as the acoustic pressure $\hat{p}(x) = S^{-1/2}(x)\boldsymbol{\varphi}^\top(x)\boldsymbol{A}$. In what follows, the above procedure of computing $\phi(x)$ and $\hat{p}(x)$ will be referred to as the Gaussian expansion method (GEM).

2.2.6 Quadratic eigenvalue problem and modal participation factors for the forced problem

In addition to solving the ABH problem defined in Eq. (2.17), finding the pressure modes within the ABH is also very interesting. To do so, the variational form in Eq. (2.17) can be rearranged into an eigenvalue problem. By separating $\kappa^2(x)$ in Eq. (2.8) into its frequency-containing component $\omega^2 R^2/c_0^2 r^2$ and its non-frequency-containing component r''/r, Eq. (2.17) can be rewritten as,

$$\begin{aligned}
&-\omega^2\frac{R^2}{c_0^2}\int_{-L}^{0}\frac{1}{r^2}\psi^*\phi\mathrm{d}x + \mathrm{j}\omega\frac{1}{c_0}\psi^*(-L)\phi(-L) + \int_{-L}^{0}\frac{r''}{r}\psi^*\phi\mathrm{d}x + \int_{-L}^{0}\frac{\mathrm{d}\psi^*}{\mathrm{d}x}\frac{\mathrm{d}\phi}{\mathrm{d}x}\mathrm{d}x \\
&+\frac{S'}{2S}(-L)\psi^*(-L)\phi(-L) - \frac{S'}{2S}(0)\psi^*(0)\phi(0) = 2\mathrm{j}k_0\mathrm{e}^{\mathrm{j}k_0L}\psi^*(-L). \qquad (2.24)
\end{aligned}$$

Taking $\phi(x) = \boldsymbol{\varphi}^\top(x)\boldsymbol{A}$ and $\psi^*(x) = \boldsymbol{B}^{\mathrm{H}}\boldsymbol{\varphi}$ its matrix counterpart is obtained,

$$\left(-\omega^2\boldsymbol{M}_{\mathrm{I}} + \mathrm{j}\omega\boldsymbol{C}_{\mathrm{BCI}} + \boldsymbol{M}_{\mathrm{II}} + \boldsymbol{K} + \boldsymbol{C}_{\mathrm{BCII}}\right)\boldsymbol{A} = \boldsymbol{F}, \qquad (2.25)$$

with

$$\boldsymbol{M}_{\mathrm{I}} := \frac{R^2}{c_0^2}\int_{-L}^{0}\frac{1}{r^2}\boldsymbol{\varphi}\boldsymbol{\varphi}^\top\mathrm{d}x, \qquad (2.26\text{a})$$

$$\boldsymbol{M}_{\mathrm{II}} := \int_{-L}^{0}\frac{r''}{r}\boldsymbol{\varphi}\boldsymbol{\varphi}^\top\mathrm{d}x. \qquad (2.26\text{b})$$

From Eq. (2.25) it becomes evident that $\boldsymbol{C}_{\mathrm{BCI}}$ plays the role of a damping matrix, which accounts for reflected waves leaving the ABH and propagating to the left of the uniform duct. On the other hand, the force term supplies the incident wave on the ABH, as seen from Eq. (2.10). By setting $\boldsymbol{F} = \boldsymbol{0}$ in Eq. (2.25) a quadratic eigenvalue problem is obtained (see, Tisseur and Meerbergen, 2001), which can be solved via linearization by introducing the first-order derivatives of $\boldsymbol{A}$ as independent variables or by an iterative approach such as Newton's eigenvalue iteration method (see, Singh and Ram, 2002; Deng *et al.*, 2023). The solution to the eigenvalue problem will provide the modal matrix of eigenvectors $\boldsymbol{P}$ and the matrix of eigenvalues $\boldsymbol{\Lambda}$.

If the scaled pressure $\phi(x)$ is needed to be expressed in terms of the modes of the system under an external force excitation like $\boldsymbol{F} = 2\mathrm{j}k_0\mathrm{e}^{\mathrm{j}k_0L}\boldsymbol{\varphi}(-L)$, the next procedure can be followed. Take $\boldsymbol{A} = \boldsymbol{P}\boldsymbol{\xi}$, where $\boldsymbol{\xi}$ is a vector whose entries are the modal participation factors and insert it into Eq. (2.25). Then pre-multiply by $\boldsymbol{P}^{\mathrm{H}}$ on the left-hand side of the equation to get

$$\boldsymbol{P}^{\mathrm{H}}\left(-\omega^2\boldsymbol{M}_{\mathrm{I}} + \mathrm{j}\omega\boldsymbol{C}_{\mathrm{BCI}} + \boldsymbol{M}_{\mathrm{II}} + \boldsymbol{K} + \boldsymbol{C}_{\mathrm{BCII}}\right)\boldsymbol{P}\boldsymbol{\xi} = \boldsymbol{P}^{\mathrm{H}}\boldsymbol{F}. \tag{2.27}$$

Solving Eq. (2.27) the modal participation vector $\boldsymbol{\xi}$ is obtained and finally, from Eq. (2.20), $\phi(x)$ can be expanded as

$$\phi(x) = \boldsymbol{\varphi}(x)^{\top}\boldsymbol{A} = \boldsymbol{\varphi}(x)^{\top}\boldsymbol{P}\boldsymbol{\xi}. \tag{2.28}$$

In Eq. (2.28), $\phi(x)$ is expressed as the superposition of all system modes. The contribution of each particular mode to $\phi(x)$ is given by,

$$\phi_i(x) = \boldsymbol{\varphi}(x)^{\top}\boldsymbol{P}_i\xi_i, \tag{2.29}$$

where $\phi_i(x)$ is the scaled sound pressure due to the i-th mode, $\boldsymbol{P}_i$ is the i-th modal vector and ξ_i the i-th modal participation factor. The total scaled pressure is given by the sum of all $\phi_i(x)$, i.e., by Eq. (2.28). Reverting from scaled pressure to acoustic pressure, the modal decomposition and contributions are obtained,

$$\hat{p}(x) = S(x)^{-1/2}\boldsymbol{\varphi}(x)^{\top}\boldsymbol{P}\boldsymbol{\xi}, \tag{2.30a}$$

$$\hat{p}_i(x) = S(x)^{-1/2}\boldsymbol{\varphi}(x)^{\top}\boldsymbol{P}_i\xi_i. \tag{2.30b}$$

2.3 Simulation results

2.3.1 Validation with FEM: a quadratic ABH

In this section, the theoretical approaches presented in the previous sections will be validated by comparing them with finite element simulations, before analyzing the behavior of theoretical ABHs. For this purpose a quadratic ABH (see e.g., Guasch *et al.*, 2017; Guasch *et al.*, 2020) is considered, which has a radius that follows the parabolic profile

$$r(x) = \frac{R - r_0}{L^2}x^2 + r_0, \tag{2.31}$$

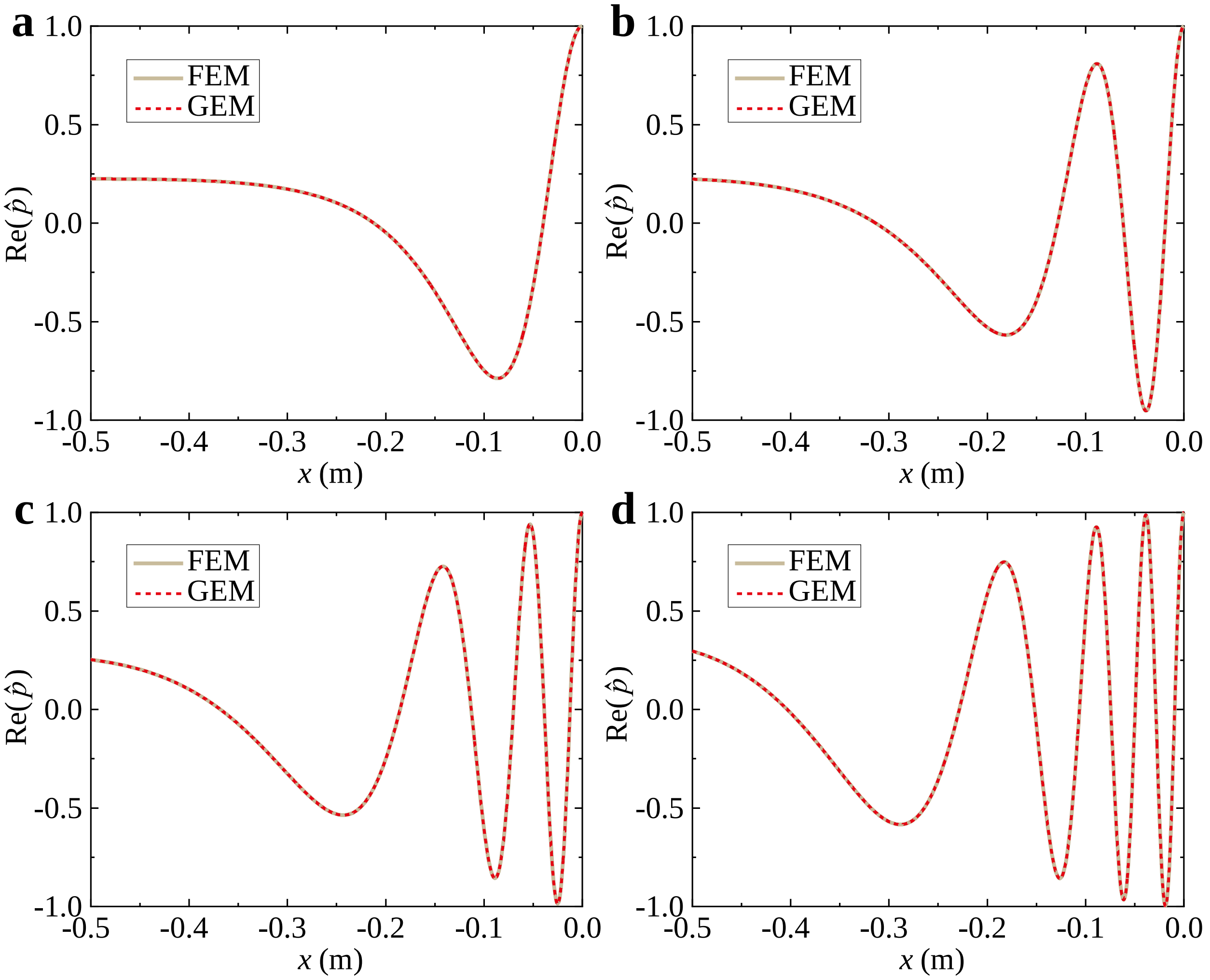

Figure 2.3: Real part of acoustic pressure, Re($\hat{p}$), computed with the FEM and GEM at (a) 100 Hz, (b) 200 Hz, (c) 300 Hz, and (d) 400 Hz. The pressure has been normalized to unity at the ABH termination $x = 0$ to facilitate comparisons.

so that,

$$S(x) = \pi r(x)^2 = \pi \frac{(R - r_0)^2}{L^4} x^4 + 2\pi \frac{R - r_0}{L^2} r_0 x^2 + \pi r_0^2. \tag{2.32}$$

It can easily be checked that $S(x = -L) = \pi R^2 \equiv S_L$ and that $S(x = 0) = \pi r_0^2 \equiv s_0$. For the case $r_0 = 0$ the ideal ABH waveguide profile in (Mironov and Pislyakov, 2002) of radius $r(x) = (R/L^2)x^2$ and cross-section $S(x) = (\pi R^2/L^4)x^4$ is recovered.

In what concerns the wavenumber κ, from Eqs. (2.8) and (2.31) it can be

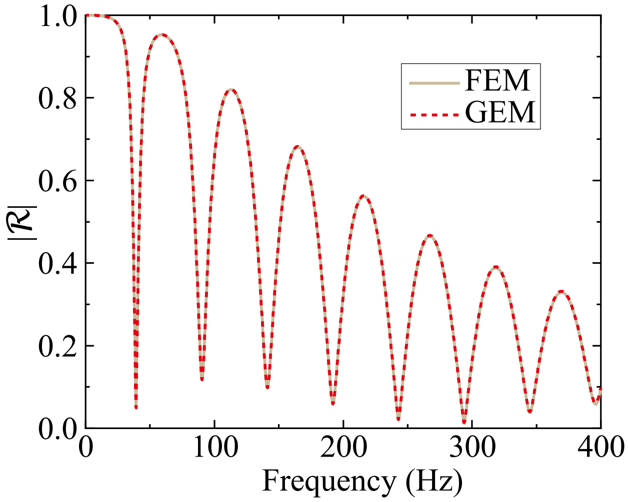

Figure 2.4: Comparison of the reflection coefficient for the quadratic ABH calculated with FEM and GEM.

written,

$$\kappa^2 = \frac{k_0^2 L^4}{\left[\left(1-\frac{r_0}{R}\right)x^2 + \frac{r_0}{R}L^2\right]^2} - \frac{2}{x^2 + \frac{r_0}{R-r_0}L^2}. \tag{2.33}$$

In the ideal case of $r_0 = 0$ or if $(r_0/R) \ll 1$ this expression becomes

$$\kappa^2 = \frac{k_0^2 L^4}{x^4} - \frac{2}{x^2}, \tag{2.34}$$

which is nothing but Eq. (18) in (Guasch *et al.*, 2020) with $m = 2$.

In all computations it is considered an ABH of length $L = 0.5$ m, input radius $R = 0.23$ m and residual radius $r_0 = 0.01$ m. The sound speed is $c_0 = c_a(1 + \mathrm{j}\eta)$ with $c_a = 343$ m/s and $\eta = 0.05$. The consideration of a complex speed of sound consists in a rough approximation to thermoviscous losses. The cutoff frequency of the tube is $f_c = 1.84 c_a/2\pi R = 445$ Hz, beyond which non-plane waves can propagate. Therefore the analysis will be restricted to the frequency range $[0, 400]$ Hz. For the simulations, and as follows from Eq. (2.10), an incident wave $\exp(-\mathrm{j}k_0 x)$ impinging on the ABH input is considered.

A total of $n = 45$ Gaussian functions have been used for the expansion in Eq. (2.20) and subsequent calculations (37 of them inside the ABH and 8 additional ones for the boundaries, see Fig. 2.2). The FEM model has been built using the Comsol 1D *Pressure Acoustic* module, with the mesh size decreasing from 0.002 m at the ABH input to 0.0001 m at the termination,

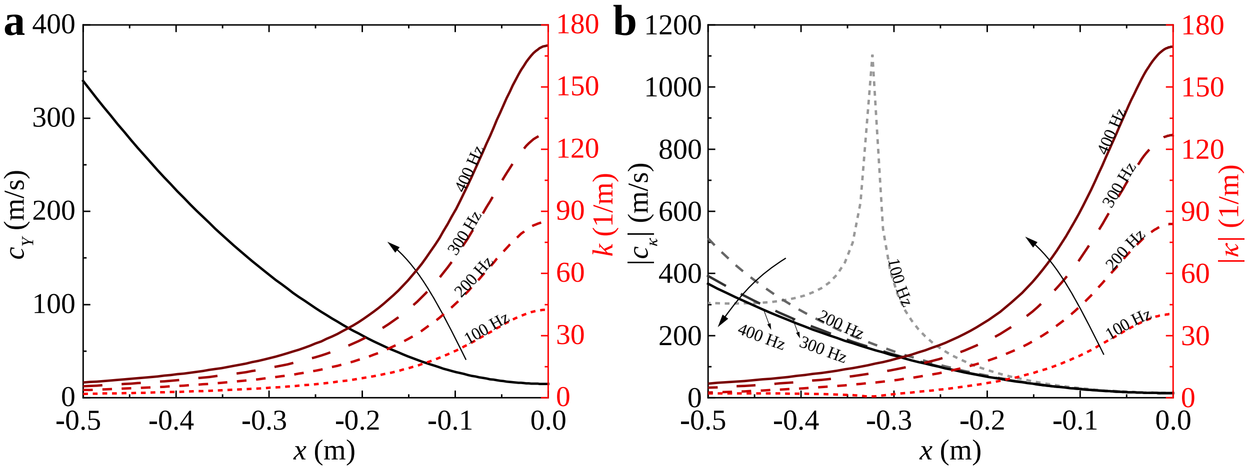

Figure 2.5: (a) Sound speed $c_Y(x) = c_0 r(x)/R$ and wavenumber $k(x) = k_0 R/r(x)$ for acoustic pressure waves $\hat{p}$ propagating within the ABH. (b) $|c_\kappa(x)|$ and $|\kappa(x)|$ for scaled pressure waves ϕ propagating inside the ABH.

resulting in a total of 1100 line elements. To simulate a half free space, a perfectly matched layer (PML) is prescribed at the left end of the uniform duct. For validation purposes, only the results within the ABH, which is the region of interest, will be presented.

In Fig. 2.3, the distribution of the real part of the acoustic pressure, $\mathrm{Re}(\hat{p}) = S^{-1/2}\mathrm{Re}(\phi)$, is plotted inside the ABH for four different frequencies of the input wave, namely, 100 Hz, 200 Hz, 300 Hz and 400 Hz. It has to be noted that the pressure has been normalized to unity in the ABH termination to facilitate comparison between figures. One initial observation is how the ABH effect takes place. As the wave approaches $x = 0$ the amplitude grows and the wavelength decreases as expected (Mironov and Pislyakov, 2002; Guasch *et al.*, 2017; Mousavi *et al.*, 2022). This becomes very evident for the higher frequencies in Figs. 2.3c and 2.3d. Most importantly for this section, a perfect match between the GEM results and the FEM ones is observed. The same degree of agreement between FEM and GEM is found for the absolute value of the ABH reflection coefficient $|\mathcal{R}|$ in Fig. 2.4. The influence of several parameters on $|\mathcal{R}|$ and its relation with the admittance will be consequently addressed in Section 2.3.4.

2.3.2 Sound speed and wavenumber within the ABH

As explained in the Introduction, when an acoustic wave enters a ABH its amplitude increases while its wavelength diminishes when approaching the

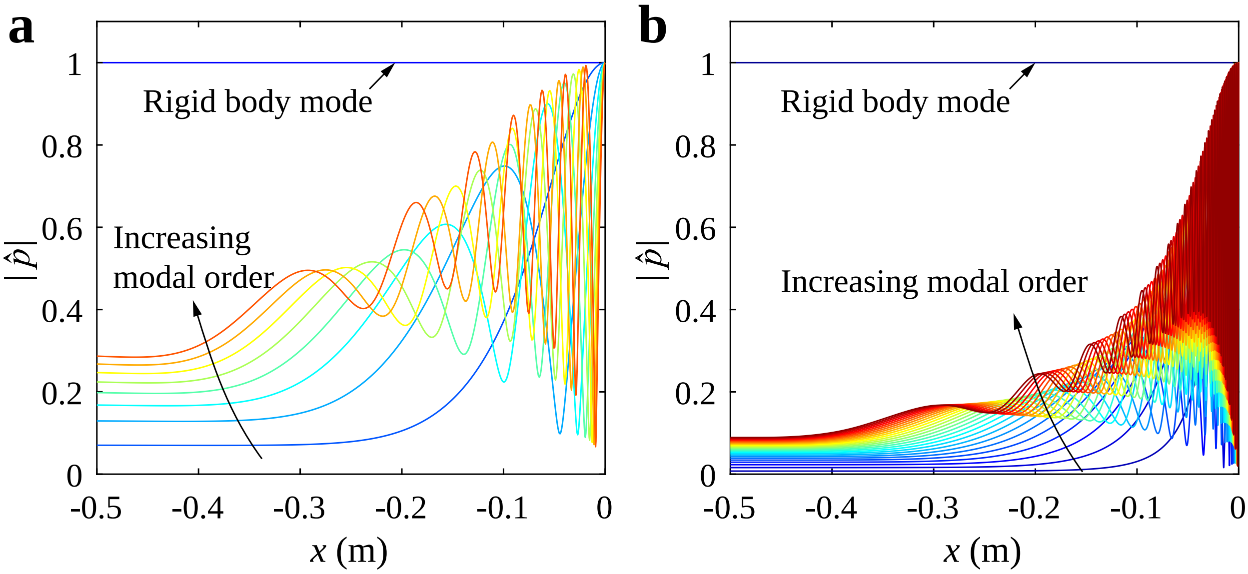

Figure 2.6: Mode shapes for (a) $r_0 = 0.01$ m and (b) $r_0 = 0.001$ m. For both cases we have considered damping with $\eta = 0.05$.

termination, as already observed in Fig. 2.3. At the same time, the wave sound speed slows down. As was demonstrated in (Mironov and Pislyakov, 2002) for a linear ABH and in (Guasch *et al.*, 2017) for a quadratic one, in the ideal case of a zero residual radius, the sound speed would become zero at the ABH termination; this means that the wave would take an infinite amount of time to reach $x = 0$ and no reflection would occur. However, if $r_0 \neq 0$, the effective sound speed $c(x)$ will decrease along the ABH but differ from zero at $x = 0$. Therefore, it is interesting to show how $c(x)$ and the wavenumber can vary within the ABH for the example presented in the previous section. In Fig. 2.5a, the sound speed $c_Y = c_0 r(x)/R$ of an acoustic wave satisfying Eq. (2.1) for the acoustic pressure $\hat{p}$ and the problem at hand is plotted. This is obtained from the wavenumber $k_Y = k_0 R/r(x)$ in Eq. (2.2), which is also shown in the same figure. The sound speed does not depend on the frequency of the incident wave and is modified from its initial value of $c_0 = 343$ m/s at the entrance of the ABH to ~ 25 m/s at its termination, by a decreasing factor $r(x)/R$. The opposite trend is observed in the wavenumber, which increases towards the end of the ABH due to being corrected by the inverse factor $R/r(x)$. Also, the higher the frequency the higher it is k because of their direct proportion, as $k_0 = \omega/c_0$ indicates.

The absolute value of the wavenumber for the scaled pressure ϕ, i.e., $\kappa(x)$ given by the square root of Eq. (2.5) and of Eq. (2.33) for the current example, along with its corresponding sound speed, c_κ, have been plotted in Fig. 2.5b. Its behaviour is somewhat more complicated than in the previous case. The main difference is that, while $|\kappa(x)|$ closely resembles $k_Y(x)$ in Fig. 2.5a, the absolute value of the sound speed, $|c_\kappa(x)|$ is now frequency dependent. At the ABH entrance $|c_\kappa(x)|$ is larger for higher frequencies, but at the termination of the ABH all curves tend to the same value. At low frequencies $\kappa(x)$ can become purely imaginary, which is the reason for the peak of the 100 Hz curve in Fig. 2.5b.

2.3.3 Modal decomposition

The method described in Section 2.2.6 can be used to compute the modes for the quadratic ABH. In Fig. 2.6 the modal shapes are plotted for two different values of the residual radius, namely $r_0 = 0.01$ m and $r_0 = 0.001$ m. By considering Fig. 2.6a, ($r_0 = 0.01$ m) it can be observed that the acoustic pressure distribution of the first mode (apart from the rigid body mode at 0 Hz) is almost constant within the ABH until $x = -0.2$ m where it starts to grow reaching its maximum at the ABH termination (note that once again the pressure has been normalized to 1 at $x = 0$ for ease of comparisons). As the modal order increases, the number of peaks grows, as one would expect, but they remain primarily concentrated at the end of the ABH.

If the residual radius is reduced by a factor of 10, i.e. $r_0 = 0.001$ (meaning that the residual surface is reduced by a factor of 100) the ABH modes become notably affected. First, and as it can be seen from Fig. 2.6b, the number of modes in the frequency range of interest, $[0, 400]$ Hz, increases significantly. Furthermore, as the modal order grows, the number of peaks and dips of the modes, as well as their amplitude, augment, and they progressively approach the ABH termination. Comparing Figs. 2.6a and 2.6b, it is already evident that the residual radius will have a critical impact on the performance of the ABH.

In Fig. 2.7 the modal decomposition of the real part of the acoustic pressure at $x = -L$ according to Eqs. (2.30a)-(2.30b) and as a function of frequency is presented and two cases are considered. In the first the residual radius is taken as $r_0 = 0.01$ m and two different scenarios are considered: with a real sound speed (by considering $\eta = 0$ in $c_0 = c_a(1 + \mathrm{j}\eta)$, see Fig. 2.7a) and with a complex sound speed, (by taking $\eta = 0.05$, see Fig. 2.7b). The second case presents the same results but for $r_0 = 0.001$ m (see Figs. 2.7c

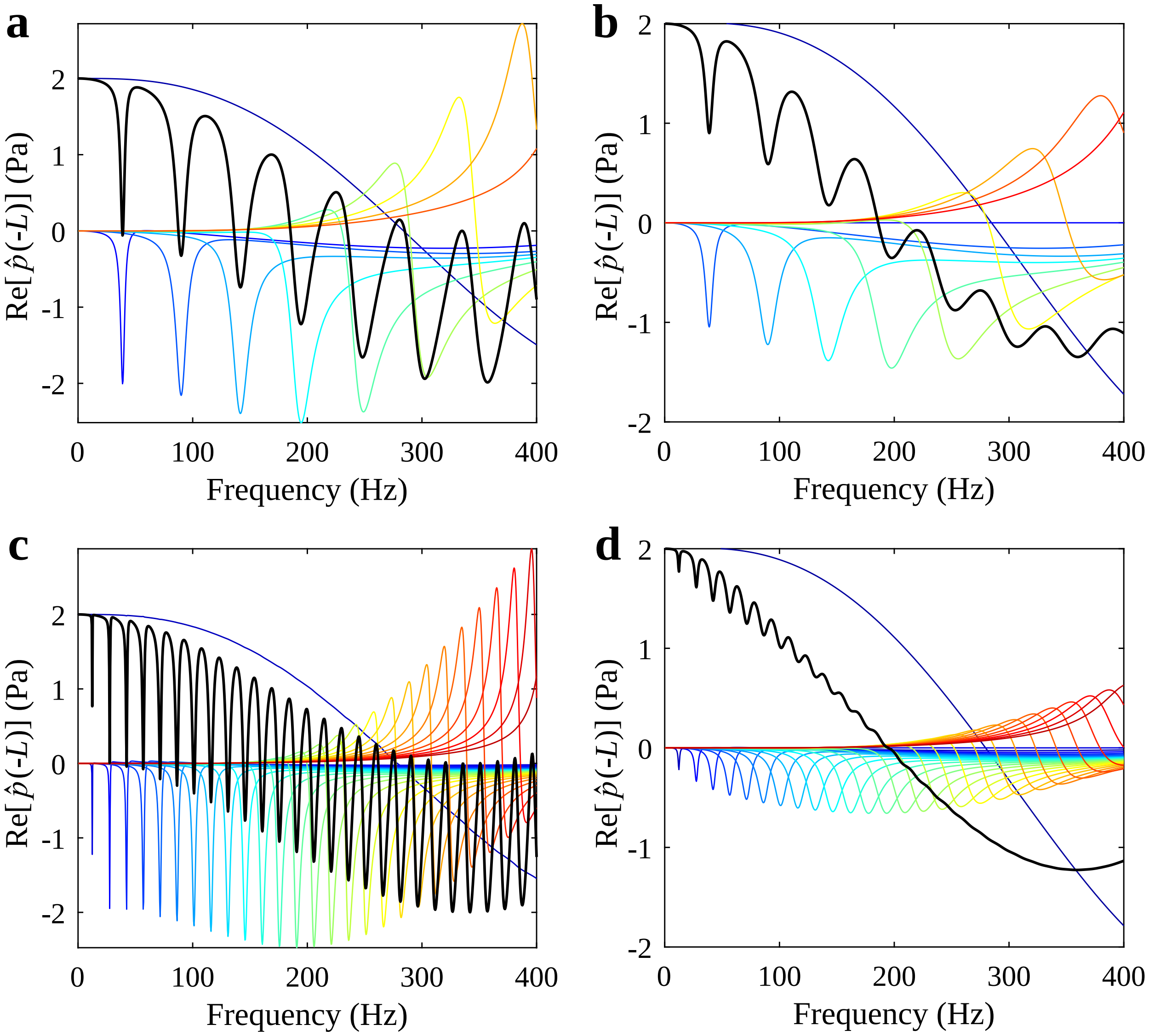

Figure 2.7: Black line: real part of the sound pressure at $x = -L$, $\mathrm{Re}[\hat{p}(-L)]$. Colored lines: modal contributions to $\mathrm{Re}[\hat{p}(-L)]$. (a) $r_0 = 0.01$ m and $\eta = 0$, (b) $r_0 = 0.01$ m and $\eta = 0.05$, (c) $r_0 = 0.001$ m and $\eta = 0$, (d) $r_0 = 0.001$ m and $\eta = 0.05$.

and 2.7d). The black curves in all subfigures are showing the real part of the acoustic pressure at the ABH entrance, i.e., $\mathrm{Re}[\hat{p}(-L)]$, while the colored ones correspond to individual mode contributions. Note that the higher order modes do not contribute at low frequencies while lower order modes have non-negligible values at the higher-frequencies. As seen in Fig. 2.7a, the acoustic pressure decays with frequency but exhibits strong oscillations of similar amplitude for the entire frequency range. When damping is introduced, the peaks of the high-frequency contributions become smoothed resulting in smaller fluctuations at these frequencies (see Fig. 2.7b). This effect becomes drastic when the residual radius is reduced to $r_0 = 0.001$ m. On the one hand, it is observed that the larger number of modes already reported in Fig. 2.6b significantly increases the number of peaks and dips of $\mathrm{Re}[\hat{p}(-L)]$ (compare Fig. 2.7c with Fig. 2.7a). On the other hand, damping has a marked effect on these modes. Their amplitude decreases strongly and, as a consequence, almost no fluctuation is observed beyond ~ 200 Hz. As will be explained in the next section, the same behavior will be observed for the reflection coefficient and the input impedance of the ABH.

2.3.4 Reflection coefficient and admittance at the ABH entrance

The most relevant parameter associated to an ABH is its reflection coefficient. In this section its dependence on several parameters, as well as that of its admittance, will be studied. The normalized impedance at the ABH entrance is given by the quotient between the acoustic pressure and the acoustic particle velocity so that $Z_L \equiv Z_n(-L) = \mathrm{j}(Z_0 k_0)^{-1}\hat{p}(-L)/\frac{\mathrm{d}}{\mathrm{d}x}\hat{p}(-L)$, while the normalized admittance is defined as $Y_L = Z_L^{-1}$. From Eqs. (2.12a) and (2.12b) it is easily seen that

$$\mathcal{R} = \mathrm{e}^{\mathrm{j}2k_0 L}\left[\frac{Z_L - 1}{Z_L + 1}\right] = \mathrm{e}^{\mathrm{j}2k_0 L}\left[\frac{1 - Y_L}{Y_L + 1}\right]. \tag{2.35}$$

From the knowledge of any of the three parameters, $\mathcal{R}$, Z_L or Y_L the other two can be computed.

2.3.4.1 Influence of the residual radius, the damping and the ABH order on the reflection coefficient

In this section, it is analyzed the influence of several parameters on the reflection coefficient of an ideal ABH with a power-law profile radius,

$$r(x) = \frac{R - r_0}{L^m}|x|^m + r_0, \tag{2.36}$$

where m is the order of the ABH.

In Fig. 2.8 the values $m = 2$ (quadratic ABH) and $\eta = 0.05$ are considered, and the impact of the residual radius is analyzed. As already noticed in the modal analysis of the previous section, it is very significant. Three values of r_0 are considered, namely $r_0 = \{0.01, 0.001, 0.0001\}$ m. The absolute value

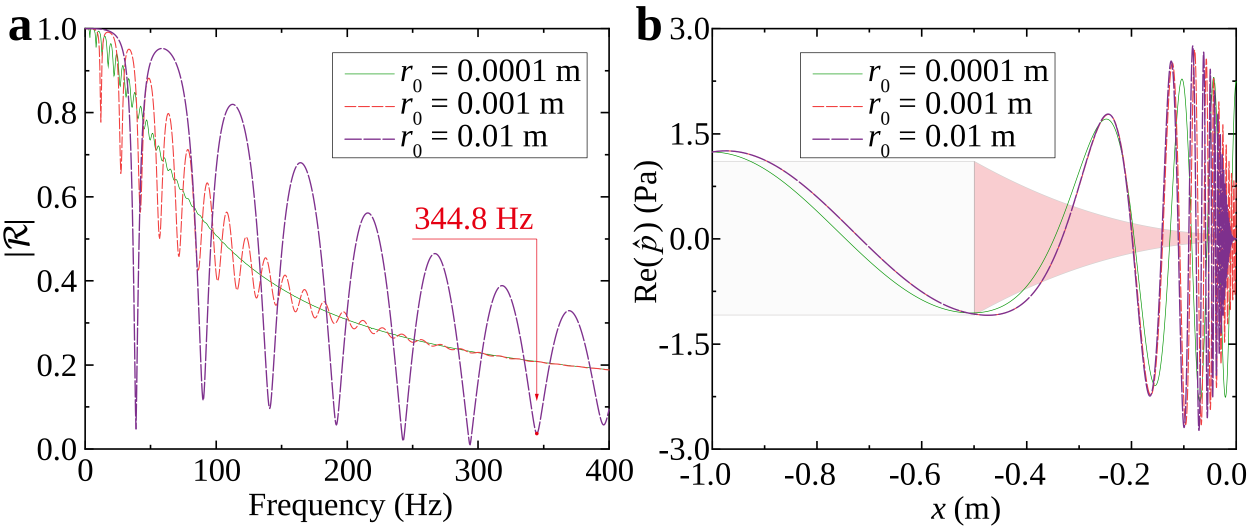

Figure 2.8: Influence of the residual radius r_0 for fixed ABH order $m = 2$ and damping $\eta = 0.05$ on (a) the absolute value of the reflection coefficient, $|\mathcal{R}|$, (b) the sound pressure distribution within the ABH at 344.8 Hz.

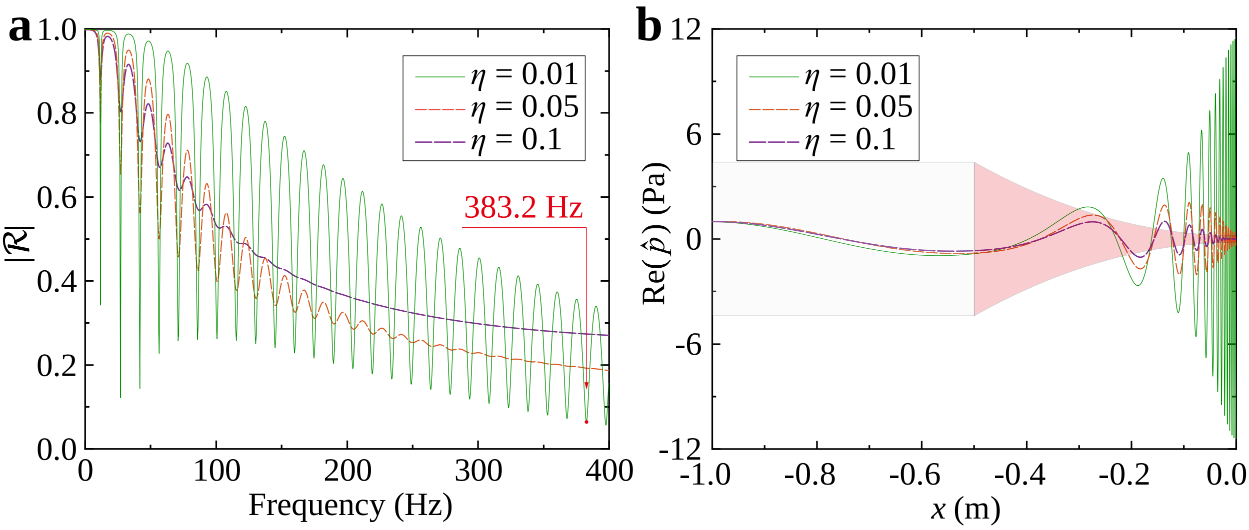

Figure 2.9: Influence of the damping η for fixed ABH order $m = 2$ and residual radius $r_0 = 0.001$ m on (a) the absolute value of the reflection coefficient, $|\mathcal{R}|$, (b) the sound pressure distribution within the ABH at 383.2 Hz.

of the reflection coefficient $|\mathcal{R}|$ shows the trend already observed in Fig. 2.6 for the real part of the pressure at $x = -L$. For large r_0, $|\mathcal{R}|$ exhibits large peaks and dips. Their number increases for decreasing r_0, whereas their values become negligible at higher frequencies because damping is very effective in dissipating the energy of the higher order modes (see Fig. 2.8a). The residual radius for ABHs in ducts plays a very similar role to that of the residual thickness in ABHs in beams and plates (Krylov and Tilman, 2004; Krylov, 2004; O'Boy and Krylov, 2011; Deng *et al.*, 2019; Deng *et al.*, 2019a). The lower its value, the more effective the ABH effect. In Fig. 2.8b, the distribution of the real pressure within the ABH at the frequency of 344.8 Hz, which corresponds to the minimum highlighted in Fig. 2.8a, is plotted. At this particular frequency the reflection coefficient is smaller for $r_0 = 0.01$ m due to specific cancellation effects between modes, than for smaller values of r_0. This is reflected in Fig. 2.8a where it can be seen that the amplitude of the oscillations for $r_0 = 0.01$ m rapidly diminishes when approaching the ABH termination, where the pressure has zero value, which is not the case for $r_0 = 0.001$ m.

In Fig. 2.9, the effects of the viscothermal losses, represented by η, on the quadratic ABH for a fixed residual radius of $r_0 = 0.001$ m are analyzed. The values $\eta = \{0.1, 0.05, 0.01\}$ are examined. The red curve corresponding to $\eta = 0.05$ is that already shown in Fig. 2.8a. If η is reduced to 0.01 the amplitude of the oscillations sharply grows over the whole frequency range (see green curve in Fig. 2.9a). However, it has to be noted that since r_0 is kept as constant, the number of oscillations is also constant for the three curves in the figure. If the damping is increased to 0.1 the oscillations of $|\mathcal{R}|$ disappear at high frequencies, but their average value becomes larger. This is not the case if η is fixed and r_0 diminishes (compare Fig. 2.8a with

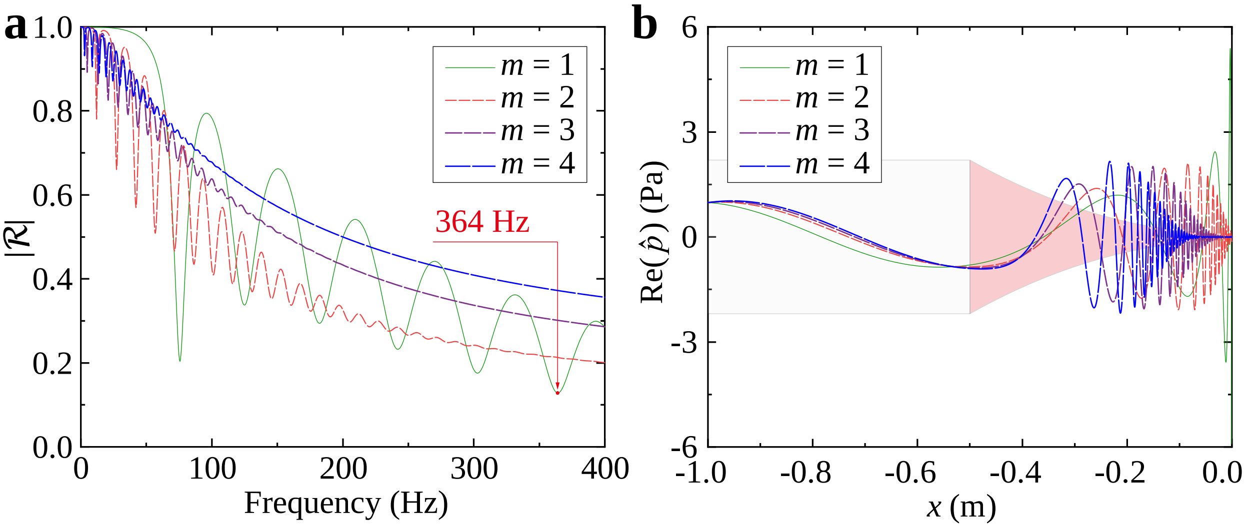

Figure 2.10: Influence of ABH order m for fixed residual radius $r_0 = 0.001$ m and damping $\eta = 0.05$ on (a) the absolute value of the reflection coefficient, $|\mathcal{R}|$, (b) the sound pressure distribution within the ABH at 364 Hz.

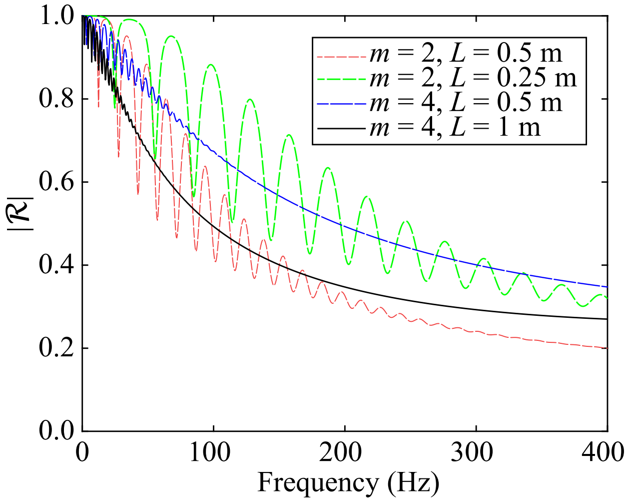

Figure 2.11: Comparison of the absolute value of the reflection coefficient, $|\mathcal{R}|$, for two quadratic ($m = 2$) ABHs of lengths $L = \{0.25, 0.5\}$ m and two quartic ($m = 4$) ABHs with $L = \{0.5, 1\}$ m.

Fig. 2.9a). The real pressure inside the ABH is plotted for the three values of η at the dip of 383.2 Hz in Fig. 2.9b. It is clearly seen how the amplitude of the oscillations decrease for larger values of η within the ABH, the effect being very remarkable as long as the termination of the ABH is approached.

The effects of varying the ABH order, m (see Eq.(2.36)), on $|\mathcal{R}|$ for fixed $r_0 = 0.001$ m and $\eta = 0.05$ are presented in Fig. 2.10. The most evident

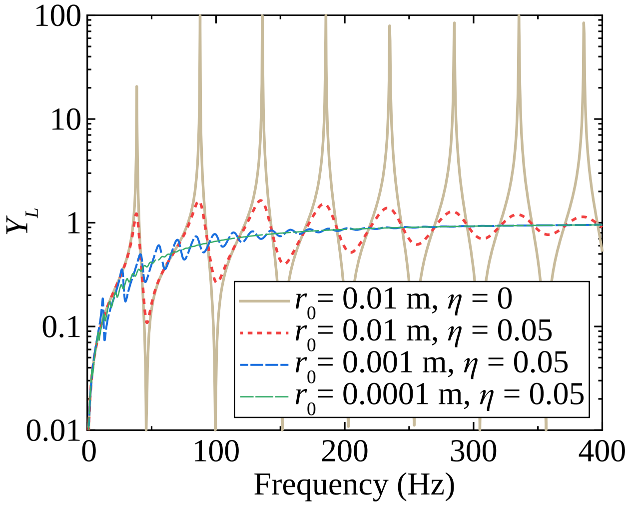

Figure 2.12: ABH admittance Y_L depending on frequency for varying residual radius r_0 and damping η.

effect in Fig. 2.10a is that a certain balance must be found between the number of oscillations of $|\mathcal{R}|$ and its mean value. For example, for $m = 1$ (linear ABH) the oscillations are very large, while for $m = 4$ they are almost non-existent (except for very low frequencies). However, the average value of $|\mathcal{R}|$ for $m = 4$ is considerable at all frequencies. A good trade-off seems to be provided by the quadratic case ($m = 2$), see the red curve in Fig. 2.10a. Again, the distribution of the real pressure at a dip of $|\mathcal{R}|$ in this case 364 Hz for $m = 1$ is shown (see Fig. 2.10b). A clear pattern can be identified in the figure. For large values of m, the impinging waves encounter a steeper *obstacle* in front of them, which prevents a smooth impedance matching and favours reflection. The radius of the ABH profile for $m = 4$ approaches the residual one sooner than for $m = 3, 2, 1$ and, consequently, the pressure amplitude decreases farther from the ABH termination for $m = 4$ than for smaller values of m. An ABH of higher-order needs a longer length L for a better impedance matching of the incident wave. This is shown in Fig. 2.11, where $|\mathcal{R}|$ is presented for two quadratic ABHs with lengths $L = \{0.25, 0.5\}$ m and two quartic ($m = 4$) ABHs with $L = \{0.5, 1\}$ m. As can be seen, the reflection coefficient for the quartic ABH of length $L = 0.5$ m is close to that of the quadratic ABH with $L = 0.25$ m, but does not exhibit oscillations. Similarly, $|\mathcal{R}|$ for the quartic ABH with $L = 1$ m is on average similar to the quadratic one, again with much less oscillations.

2.3.4.2 Influence of the residual radius and damping on the admittance

As shown in Eq. (2.35) the reflection coefficient $\mathcal{R}$, the normalized impedance Z_L and the admittance Y_L at the ABH inlet are directly related. To complete the results for $\mathcal{R}$ presented in the previous section, it is worth taking a look at the behaviour of Y_L.

In Fig. 2.12 the dependence of Y_L on frequency is plotted for different values of r_0 and η. If the residual radius r_0 is kept fixed and η increases, the strong peaks of the brown curve in the figure decrease significantly, the effect being more marked at higher frequencies. For fixed η, the high-frequency peaks disappear completely if r_0 decreases. This is in full agreement with the previous results for $\mathcal{R}$, and can be explained by the distribution of modes within the ABH and the effect of damping on them.

In Fig. 2.13 results for Y depending on frequency and the location inside the ABH are presented for four different combinations of (r_0, η), namely $(r_0, \eta) =$

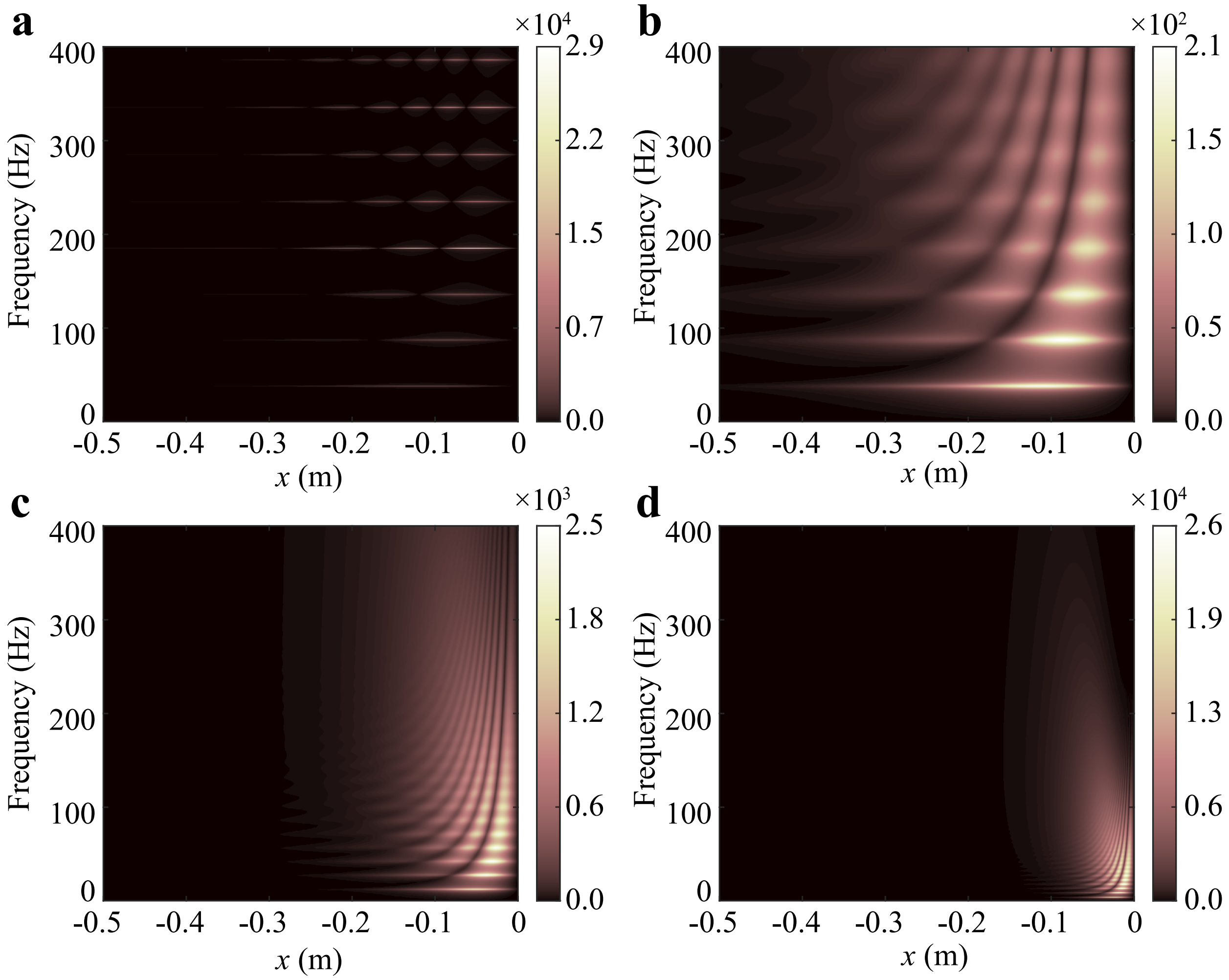

Figure 2.13: ABH admittance depending on frequency and location within the ABH for varying residual radius r_0 and damping η. (a) $r_0 = 0.01$ m and $\eta = 0$. (b) $r_0 = 0.01$ m and $\eta = 0.05$. (c) $r_0 = 0.001$ m and $\eta = 0.05$. (d) $r_0 = 0.0001$ m and $\eta = 0.05$.

$\{(0.01, 0), (0.01, 0.05), (0.001, 0.05), (0.0001, 0.05)\}$. Note that a vertical cut at $x = -L = -0.5$ m in each of the subfigures in Fig. 2.13 would correspond to the curves in Fig. 2.12. However, no peaks are visible because of the color scale used for the figures, as the admittance at the ABH termination is much higher than at its input. In Fig. 2.13a, the same peaks already found in Fig. 2.12 (brown curve) appear all along the ABH with some amplitude variations and with much higher values when approaching the termination at $x = 0$. These peaks become strongly attenuated and their width widens when damping is introduced (see Fig. 2.13b, where the color scale has been reduced by two orders of magnitude to facilitate comparison with Fig. 2.13a). Decreasing the residual radius r_0 to 0.001 m raises the number of peaks, as

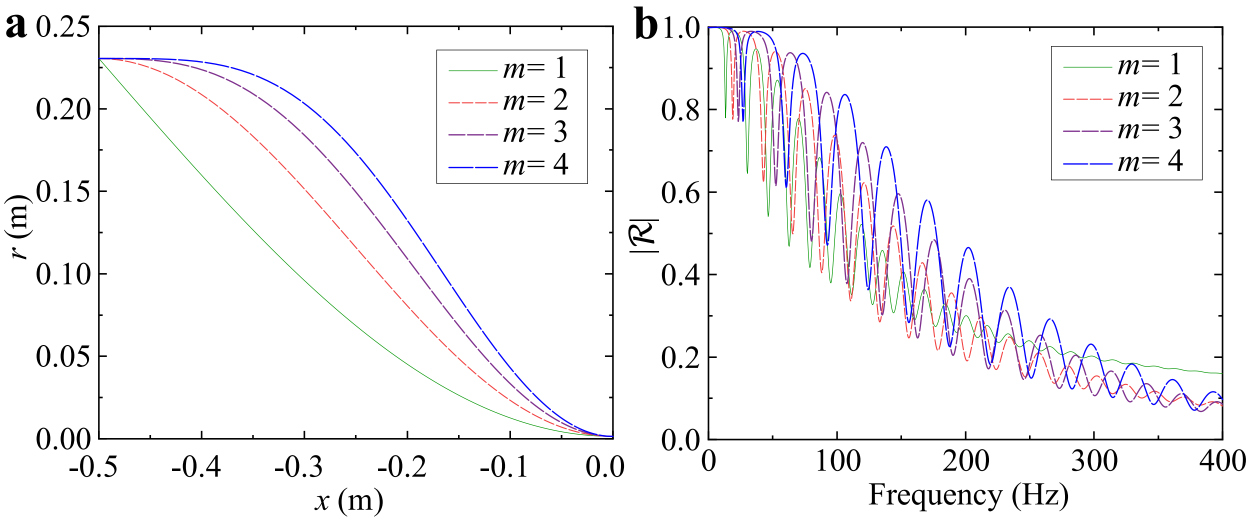

Figure 2.14: (a) Power-cosine profiles and (b) corresponding reflection coefficients for different values of m.

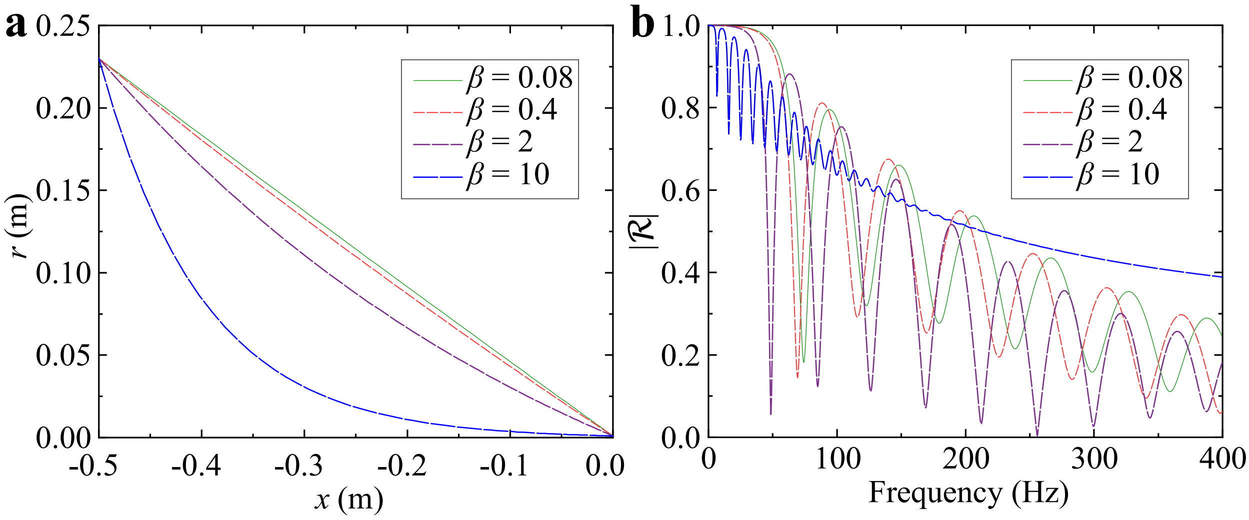

Figure 2.15: (a) Exponential profiles and (b) corresponding reflection coefficient for different values of β.

already observed in previous figures, increases their amplitude near the ABH termination at low frequencies and suppresses the peaks for higher frequencies (compare Fig. 2.13c with Fig. 2.13b). The effect is more pronounced the smaller the residual radius (see Fig. 2.13d).

2.3.5 Alternative ABH profiles to the power-law: power-cosine, exponential and Gaussian.

To conclude this study on the behaviour of ideal ABHs, alternative waveguide profiles to the power-law one of Eq. (2.36) will be analyzed, taking inspiration from those tested for ABH beam wedges in (Karlos *et al.*, 2019). In particular, the following options for the monotonically decreasing radius of the waveguide are considered,

- The power cosine profile: $r(x) = (R - r_0)\left[1 - \cos^m(\frac{\pi x}{2L})\right] + r_0$, with $m \geq 1$,
- The exponential profile: $r(x) = \frac{R-r_0}{1-\mathrm{e}^{\beta L}}(1 - \mathrm{e}^{-\beta x}) + r_0$, with $\beta > 0$,
- The Gaussian profile: $r(x) = \frac{R-r_0}{1-\mathrm{e}^{-\gamma L^2}}(1 - \mathrm{e}^{-\gamma x^2}) + r_0$, with $\gamma > 0$

In all the simulations the same values for R and L as in preceding sections are taken, and a damping of $\eta = 0.05$ and a residual radius of $r_0 = 0.001$ m are considered.
In Fig. 2.14a power-cosine profiles for the waveguide radius $r(x)$ of orders $m = 1, 2, 3, 4$ are shown. It has to be noted that if a first order Taylor expansion for the cosine at $x = 0$ for $m = 1$ is performed, a quadratic power-law ABH with an effective length $L' = 2\sqrt{2}L/\pi \simeq 0.9L$ is recovered, so the two cases should behave very similarly. In fact, this is confirmed in Fig. 2.14b,

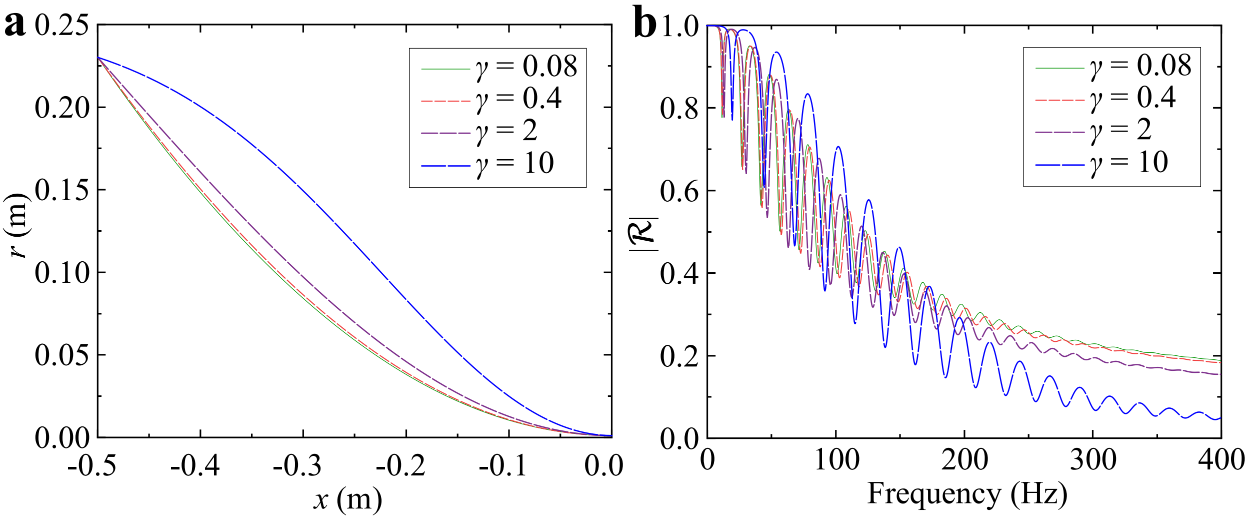

Figure 2.16: (a) Gaussian profiles and (b) corresponding reflection coefficients for different values of γ.

where $|\mathcal{R}|$ for the four power-cosine cases is plotted. It can be seen that the green curve corresponding to $m = 1$ closely resembles the red one in Fig. 2.10. As for the rest of the orders, it is observed from Fig. 2.14a that the higher the m the steeper the profile and, therefore, the worse the $|\mathcal{R}|$ in Fig. 2.14b. The situation is analogous to power-law profiles but with inverse concavity.
The results for the exponential case are plotted in Fig. 2.15 for the exponents $\beta = \{0.08, 0.4, 2, 10\}$. A first order Taylor expansion at $x = 0$ directly results in the radius of a linear ABH (Eq. (2.36) with $m = 1$). Looking at Fig. 2.15a it can be realised that the profiles do not change significantly for $\beta = \{0.08, 0.4\}$ and that to obtain a steep profile it is necessary to have $\beta = 10$. The curves for $|\mathcal{R}|$ in Fig. 2.15b reveal that for $\beta = \{0.08, 0.4\}$ the reflection coefficient is similar to that of a linear ABH (see the green curve in Fig. 2.10), while for $\beta = 10$, $|\mathcal{R}|$ is closer to those found for higher-order power-law profiles (see the blue line in Fig. 2.10), but with stronger oscillations at low frequencies and higher average value over the whole frequency range (at least for the tested case).
In Fig. 2.16, the performance of the Gaussian profiles with $\gamma = \{0.08, 0.4, 2, 10\}$ (i.e., the same values tested for β in the exponential case of Fig. 2.15) are presented. A Taylor expansion at $x = 0$ shows now that the quadratic ABH is recovered for $\gamma = 1$. Indeed, it is observed in Fig. 2.16a that the profiles do not change significantly from each other for $\gamma = \{0.08, 0.4, 2\}$. Their respective reflection coefficients in Fig. 2.16b are similar to that of the quadratic ABH in Fig. 2.10, while for $\gamma = 10$ we have much more oscillations across the whole spectrum, yet a smaller average value at high frequencies.
From Figs. 2.14b-2.16b it is clear that, with accurate design, low-order cosine-power and Gaussian profiles could produce reflection coefficients as good as the power law ones. This is true at least for short ABHs where Taylor expansions of the profiles give very similar geometries.

2.4 Conclusions

This chapter proposes a theoretical framework for analyzing the performance of theoretical ABHs. The first step involves transforming the generalized Webster equation for acoustic wave propagation inside the ABH into a Helmholtz equation with spatially varying wavenumber for a locally scaled pressure. The variational formulation of this equation is introduced and solved using a

Gaussian basis to expand the unknown scaled pressure. The basis of Gaussian functions is refined near the ABH termination to better capture the wavelength decrease and amplitude increase produced by the ABH effect. A quadratic eigenvalue problem is derived by splitting the wavenumber of the weak form of the Helmholtz equation into its frequency-dependent and non-frequency-dependent parts. This allows to compute the eigenmodes of the ABH and to decompose the scaled acoustic pressure in terms of them. Moreover, a thorough analysis of the theoretical ABH is provided. It is shown that the speed of sound slows down inside the ABH, and the wavenumber is frequency-dependent and increases towards the ABH termination. The modal analysis of the ABH reveals that the mode shapes are strongly affected by the residual radius, with smaller residual radii resulting in a greater number of modes and higher frequency modes concentrated near the ABH end. Damping has a strong impact on the modes, and decreasing the residual radius suppresses high-frequency peaks and dips. Overall, long, high-order ABHs are found to achieve nearly oscillation-free reflection coefficients. Finally, alternative ABH profiles are explored, including power cosine, exponential, and Gaussian profiles. The results show that reflection coefficients similar to the power-law ones can be obtained with appropriate choice of order and exponent values.

Chapter 3

The Transfer Matrix Method applied to acoustic black hole duct terminations

The aim of this chapter is to prove that the Transfer Matrix Method (TMM), widely used in many areas of acoustics and science, can be used consistently to solve the ABH equation for duct terminations. By making a comparison with the theoretical framework exposed in Chapter 2, the TMM will rely on further assumptions, which will make its study more complex but, on the other side, closer to a real setup. In fact, one of the purposes of using the TMM is to analyze a finite realization of an ABH, that is with a finite and limited number of rings and cavities, which will be important from a manufacturing point of view. Moreover, the TMM is very performant for the quick analysis of many different configurations, obtained by letting parameters varying their values; once promising configurations are identified with the TMM, other methods more computationally expensive can be used to carry out a more detailed analysis. For the purpose of demonstrating the TMM consistency, the ABH equation in a duct termination will be showed to be equivalent to the equation describing wave propagation in a metafluid with layers whose density changes along with the position. Finally, it will be proved that, when the number of layers tends to infinity, the TMM solution for the metafluid case tends to the solution of the continuous problem.

Concerning development aspects, all the analytical calculations of this chapter have been done firstly by hand and then double-checked via numeric symbolic calculation using PARI-GP (`https://pari.math.u-bordeaux.fr/`).

Moreover, the calculation of the reflection coefficient for many different configurations has been implemented within an internal Matlab code.

This chapter is mainly based on the following work:

- Oriol Guasch, Patricia Sánchez-Martín and Davide Ghilardi (2020), "Application of the transfer matrix approximation for wave propagation in a metafluid representing an acoustic black hole duct termination", Applied Mathematical Modelling, 77, pp. 1881-1893.

3.1 Introduction

As explained in the introductory chapter, most research in the field of acoustic black holes has been devoted to structural ABHs, by considering flexural waves propagating in beams or plates. In (Mironov, 1988), which is considered as the pioneer work of the field, a beam equipped with a wedge whose thickness decreases following a power law was considered and it was showed that a wave propagating in such a wedge would progressively be absorbed. For an ideal case of a beam with zero end thickness, the wave would never reach the end of the wedge and perfect absorption would be achieved. Nevertheless, for practical ABH realization, a small truncation in the wedge profile needs to be introduced, which causes detrimental effects on the ABH performance. However, it has been showed that the ABH effect can be achieved also for the case of acoustic waves propagating in ducts (see e.g., Mironov and Pislyakov, 2002). In the aforementioned work, the design of a retarding structure made of separated cavities and rings with power-law decaying inner radii was proposed. Moreover, a one-dimensional differential equation that describes the wave propagation inside the ABH was derived. Years later, linear and quadratic ABHs were built and experimental measurements reported, not fully clarifying the efficiency of absorption materials in such retarding structure (see e.g., El Ouahabi *et al.*, 2015; El Ouahabi *et al.*, 2015b; Mi *et al.*, 2021). Then, it has been proposed to use the transfer matrix method (TMM) to analyze finite realizations of ABHs, particularly useful from a practical manufacturing point of view, since the number of rings and cavities should be rather reduced (see e.g., Guasch *et al.*, 2017). Finally, in (Bravo and Maury, 2023), the TMM is used to model the acoustic performance of a widely-opened ABH and thermoviscous losses are taken into account; a good

agreement with FEM and experimental results is found.
In this chapter, it will be proved that the TMM solutions tend to the solution of the differential ABH equation, for an ABH of any order $n \geq 1$, when the number of rings and cavities goes to infinity. In fact, although the TMM is widely used in may research field, no attention has been put on the limit behavior of the TMM when the number of the required layers tends to infinity (that is, their thickness tends to zero). First, the derivation of the ABH equation will be reviewed in Section 3.2 and a one-dimensional wave equation for inhomogeneous fluids with varying density will be introduced as well. Furthermore, an introduction to the classical transfer matrix method (TMM) and its application to the retarding structure context will be provided. Then, in Section 3.3, the metafluid analogy, the smoothness condition and the TMM approximation for the metafluid will be introduced. The metafluid analogy will consist in the equivalence of three equations: the governing equation of an acoustic wave propagating inside a duct with inner radius decreasing to zero by following a power law, the equation of wave propagation in a duct filled with a metafluid with power-law increasing density and a Helmholtz equation for a wave with spatially varying wavenumber. This will be a key element for the demonstration of the consistency of the TMM solution, that will be consequently addressed. It will be showed that the TMM solution formally tends to the solution of the ABH equation, making use of the metafluid analogy. In fact, this is the main result of this chapter and the main contribution of the related work. In Section 3.4, the analytical expressions of reflection coefficients for linear and quadratic cases will be introduced. Finally, numerical results comparing the analytical and the TMM reflection coefficients will be presented and discussed. It is showed that the analytical solution tends to the numerical one when increasing the number of layers of the metafluid. Moreover, the quadratic ABH performs better than the linear one, because its convergence is faster and its stability with respect to the small truncation that needs to be introduced is much higher.

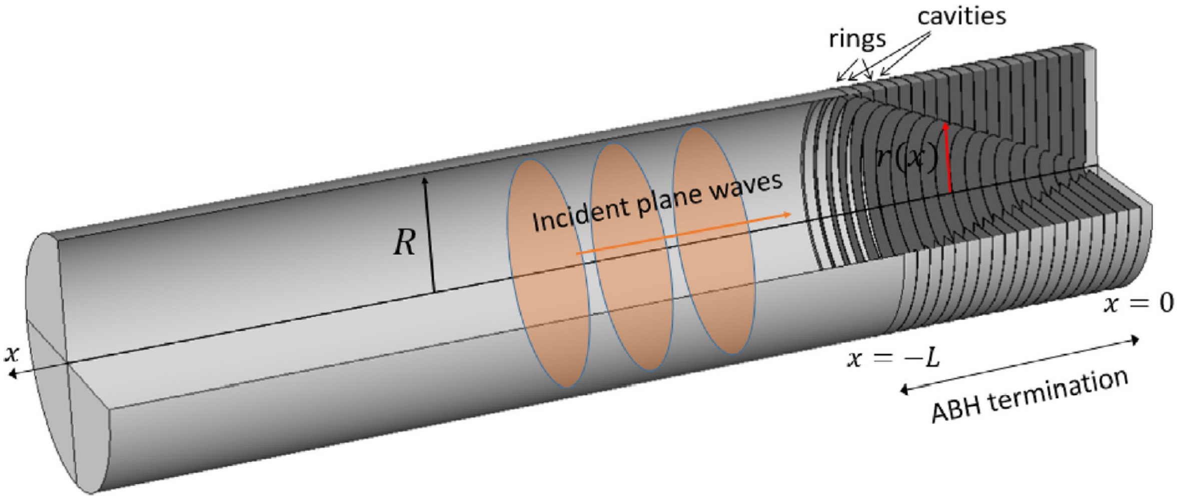

Figure 3.1: Sketch of a cylindrical duct with an ABH termination where a quarter of the cylinder has been removed in order to show the inner ABH structure made of rings and cavities.

3.2 Governing differential equations and TMM approximation

3.2.1 Governing equation for the ABH in a duct termination

As mentioned in the Introduction, a duct with circular cross-section and a termination consisting of a retarding structure that produces the ABH effect for plane wave propagation are considered. The retarding structure of length L is made of a set of rigid rings, separated by air cavities, whose inner radii $r(x)$ decrease by following a power-law decay. Throughout the development of our formulation, x denotes the longitudinal axis coordinate with the origin placed at the end of the duct termination (see Figure 3.1). Therefore, the ABH is comprised between $x = -L$ (where the wave enters the retarding structure) and $x = 0$ (duct end). Considering the limit case of a very high number of ring-cavity ensembles, such system can be described by the continuity and momentum equations for a isentropic wave propagation in an axisymmetric duct of varying cross section $S(x) = \pi r^2(x)$ and wall admittance $Y(x)$. These equations are (see Mironov and Pislyakov, 2002),

$$\frac{\partial \rho}{\partial t} + \frac{\partial(\rho u)}{\partial x} + \rho u \frac{1}{S}\frac{\partial S}{\partial x} + \frac{2\rho Y p}{r} = 0, \tag{3.1a}$$

$$\rho\frac{\partial u}{\partial t} + \rho u \frac{\partial u}{\partial x} + \frac{\partial p}{\partial x} = 0, \tag{3.1b}$$

where $\rho(x,t)$ denotes the air density, $p(x,t)$ the air pressure and $u(x,t)$ the velocity. For small acoustic perturbations, it can be considered $\rho(x,t) = \rho_0 + \rho'(x,t)$, ρ_0 standing for the mean air density, $p(x,t) = p_0 + p'(x,t)$, p_0 being the ambient pressure and $u(x,t) = u'(x,t)$, meaning that zero mean air velocity inside the duct is taken into account. Therefore, p_0 and ρ_0 are the mean values, while the prime terms $\rho'(x,t)$, $p'(x,t)$ and $u'(x,t)$ are the small perturbations considered. Since the case of isentropic wave propagation inside the duct is contemplated, the density and pressure fluctuations are related through $p'(x,t) = c_0^2\rho'(x,t)$, where c_0 denotes the sound speed. After the linearization of equations (3.1), taking the difference between the time derivative of (3.1a) and the space derivative of (3.1b), one arrives at,

$$\frac{1}{c_0^2}\frac{\partial^2 p'}{\partial t^2} + \frac{2\rho_0 Y}{r}\frac{\partial p'}{\partial t} - \frac{\partial^2 p'}{\partial x^2} + \left[S(x)\frac{\partial}{\partial x}\Big(\frac{1}{S(x)}\Big)\right]\frac{\partial p'}{\partial x} = 0, \tag{3.2}$$

which is a generalization of the Webster's wave equation for the case of non-rigid duct walls. Considering a harmonic time dependence for p, that is $p(x,t) = \hat{p}(x)e^{-\mathrm{j}\omega t}$, it is possible to rewrite (3.2) in the frequency domain as,

$$-\frac{\partial^2 \hat{p}}{\partial x^2} - \Big[k_0^2 + \mathrm{j}Z_0\frac{2Y}{r}k_0\Big]\hat{p} + \left[S(x)\frac{\partial}{\partial x}\Big(\frac{1}{S(x)}\Big)\right]\frac{\partial \hat{p}}{\partial x} = 0, \tag{3.3}$$

where $k_0 = \omega/c_0$ is the wavenumber, ω being the radial frequency and $Z_0 = \rho_0 c_0$ the air characteristic impedance.

The power-law decay for the inner radius $r(x)$ of the rings composing the retarding structure, slightly mentioned at the beginning of the section, is introduced

$$r(x) = \frac{R}{L^m}\left|x\right|^m, \tag{3.4}$$

where m is a real number that is referred to as order of the ABH. It is to be noted that $r(-L) = R$ (corresponding to the entrance of the retarding structure) and $r(0) = 0$ (corresponding to the end of the retarding structure and of the duct): while a wave propagates from the beginning to the end of the ABH, the inner radii of the rings are decreasing and, consequently, the areas of the annulus increase. Furthermore, in order to achieve the ABH effect, the wall admittance $Y(x)$ needs to show a dependence on $r(x)$. In (Mironov and Pislyakov, 2002) it is implicitly supposed that if only the air cavities thickness is considered, while neglecting the inner rings ones, a continuous wall admittance can be built as a limit case of a TMM cavity lumped admittance,

$$Y(x) = -\mathrm{j}\frac{k_0}{Z_0}\frac{R^2 - r^2}{2r}. \tag{3.5}$$

Finally, substituting (3.4) and (3.5) in (3.3), and by considering $S = \pi r^2$, the ABH governing equation is obtained

$$\frac{\partial^2 \hat{p}}{\partial x^2} + \frac{2m}{x}\frac{\partial \hat{p}}{\partial x} + \left(\frac{k_0 L^m}{x^m}\right)^2 \hat{p} = 0. \tag{3.6}$$

The equation (3.6) is the general equation of an ABH of order m. In particular, especially in Chapter 4, it will be given attention and detailed consideration to the specific cases where $m = 1$

$$\frac{\partial^2 p}{\partial x^2} + \frac{2}{x}\frac{\partial p}{\partial x} + \left(\frac{k_0^2 L^2}{x^2}\right) p = 0, \tag{3.7}$$

and where $m = 2$

$$\frac{\partial^2 p}{\partial x^2} + \frac{4}{x}\frac{\partial p}{\partial x} + \left(\frac{k_0^2 L^4}{x^4}\right) p = 0, \tag{3.8}$$

that will be respectively referred to as linear ABH and quadratic ABH.

3.2.2 Governing equation of plane waves in a duct filled with a non-homogeneous fluid

The plane wave propagation in a duct filled with a non-homogeneous fluid with varying density is considered. The one-dimensional continuity and momentum equations of the fluid are

$$\frac{\partial \rho}{\partial t} + \frac{\partial(\rho u)}{\partial x} = 0, \tag{3.9a}$$

$$\rho\frac{\partial u}{\partial t} + \rho u\frac{\partial u}{\partial x} + \frac{\partial p}{\partial x} = 0, \tag{3.9b}$$

where $\rho(x,t)$, $p(x,t)$ and $u(x,t)$ respectively stand for the air density, pressure and velocity. The state equation is given by (see, Bergmann, 1946; Climente, 2015)

$$\frac{\partial p}{\partial t} - \frac{B_s}{\rho}\left(\frac{\partial \rho}{\partial t} + u\frac{\partial \rho}{\partial x}\right) = 0, \tag{3.10}$$

where the flow compressibility $B_s(x)$ depending only on the position x is assumed. The combination of (3.9a) and (3.10) leads to

$$\frac{\partial p}{\partial t} + B_s \frac{\partial u}{\partial x} = 0. \tag{3.11}$$

Once again, small perturbations $\rho(x,t) = \rho_0 + \rho'(x,t)$, $p(x,t) = p_0 + p'(x,t)$ and $u(x,t) = u'(x,t)$ (zero mean fluid velocity inside the duct) are considered in (3.9b) and (3.10). After linearization, we can write

$$\frac{\partial p'}{\partial t} + B_s(x)\frac{\partial u'}{\partial x} = 0, \tag{3.12a}$$

$$\rho_s(x)\frac{\partial u'}{\partial t} + \frac{\partial p'}{\partial x} = 0. \tag{3.12b}$$

Finally, a wave equation can be written by taking the difference between the partial time derivative of (3.12a) and the spatial derivative of $B_s(x)$ times (3.12b). After some simple mathematical manipulations this can be expressed as

$$\rho_s(x)\frac{\partial^2 p'}{\partial t^2} - B_s(x)\frac{\partial^2 p'}{\partial x^2} + \left[\frac{B_s(x)}{\rho_s(x)}\frac{\partial \rho_s(x)}{\partial x}\right]\frac{\partial p'}{\partial x} = 0. \tag{3.13}$$

Introducing the definition of the space dependent wave speed as $c_s(x) := [B_s(x)/\rho_s(x)]^{1/2}$, (3.13) can be rewritten in the following way

$$\frac{1}{c_s^2(x)}\frac{\partial^2 p'}{\partial t^2} - \frac{\partial^2 p'}{\partial x^2} + \left[\frac{1}{\rho_s(x)}\frac{\partial \rho_s(x)}{\partial x}\right]\frac{\partial p'}{\partial x} = 0. \tag{3.14}$$

Eq. (3.14) describes the one-dimensional wave propagation in a non-homogeneous medium and it can be expressed in the frequency domain as

$$-\frac{\partial^2 \hat{p}}{\partial x^2} - k_s^2(x)\hat{p} + \left[\frac{1}{\rho_s(x)}\frac{\partial \rho_s(x)}{\partial x}\right]\frac{\partial \hat{p}}{\partial x} = 0, \tag{3.15}$$

where $k_s(x) := \omega/c_s(x)$ is the space dependent wave number.

3.2.3 The Transfer Matrix Method (TMM) for ABHs

As it has been mentioned in the Introduction, the Transfer Matrix Method (TMM) is commonly used to analyze wave propagation through multilayered media. In fact, when trying to perform a practical realization of an ABH, many limitations rise up. These are related to the number and size of rings and cavities, as well as their thickness, their profile and the material used to build the structure. By utilizing the TMM, it is possible to identify the parameters that offer the most promising ABH configurations, which can be further analyzed through more detailed numerical simulations. Nonetheless, the classical TMM for acoustic filters can provide a reliable model to describe the behavior of linear and quadratic retarding structures in a way closer to reality than the analytical one. To this purpose, the ABH structure can be thought as a set of ring plus cavity ensembles, that is nothing but two cylindrical ducts, one of them with a decreasing radius (see Figure 3.2). The TMM allows one to relate the state vector for the acoustic pressure and acoustic particle velocity at a point x_m in the waveguide, namely $(p_m, v_m)^{\mathrm{T}}$, with the state vector at any other point inside the duct. Nevertheless, the acoustic volume velocity u_m is being considered instead of the particle velocity v_m because this will allow us to use transfer matrices with easier expressions. This will be beneficial for the formulation, but it will not affect the results, since it is always possible to switch between u_m and v_m simply by considering the expression $u_m = S_m v_m$, where S_m stands for the section of the waveguide at the location x_m. By referring to Figure 3.2, the state vector $(p_{i+2}, u_{i+2})^{\mathrm{T}}$ at x_{i+2} (end of the inner ring edge) can be related to $(p_{i+1}, u_{i+1})^{\mathrm{T}}$ at x_{i+1} (beginning of the inner ring edge) by means of a propagation transfer matrix $\mathbf{T}_{i+1}^{\text{ring}}$. Analogously, the acoustic pressure and acoustic volume velocity $(p_{i+1}, u_{i+1})^{\mathrm{T}}$ at x_{i+1}, which also corresponds to the end of the lateral cavity,

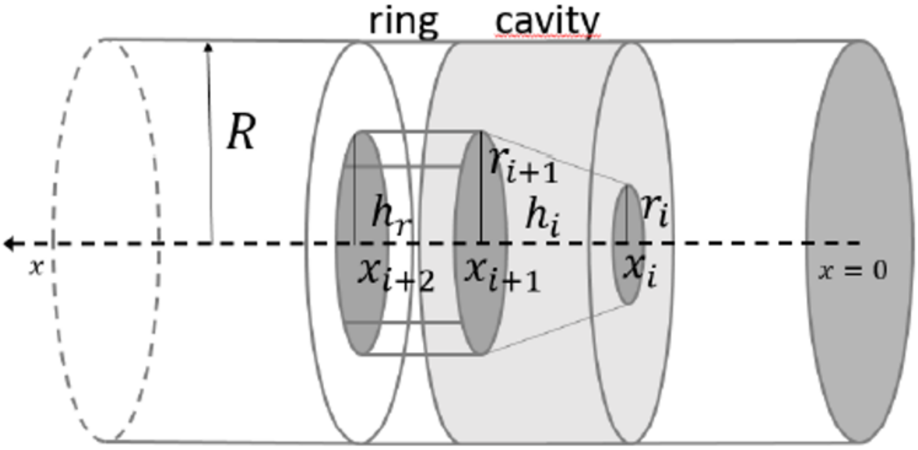

Figure 3.2: Sketch of a cavity plus ring ensemble (Guasch *et al*, 2017).

can be related to those at its beginning, $(p_i, u_i)^{\mathrm{T}}$, through another transfer matrix $\mathbf{T}_i^{\mathrm{cav}}$. $\mathbf{T}_i^{\mathrm{cav}}$ takes into account three different effects. First, the influence of the cavity itself, which can be represented as a lumped element with transfer matrix $\mathbf{T}_i^{\mathrm{lm}}$. Second, the change of section between the beginning and the end of the cavity which, by considering the acoustic volume velocity, is intrinsically considered. Third, its finite width, which can be included by means of a propagating matrix, $\mathbf{T}_i^{\mathrm{p}}$. This whole formulation, including explicit expressions for the aforementioned matrices $\mathbf{T}_{i+1}^{\mathrm{ring}}$, $\mathbf{T}_i^{\mathrm{p}}$ and $\mathbf{T}_i^{\mathrm{lm}}$, reads as it follows (see Guasch *et al*, 2017),

$$
\begin{aligned}
&\begin{pmatrix} p_{i+2} \\ u_{i+2} \end{pmatrix} = \mathbf{T}_{i+1}^{\mathrm{ring}} \begin{pmatrix} p_{i+1} \\ u_{i+1} \end{pmatrix} = \mathbf{T}_{i+1}^{\mathrm{ring}} \mathbf{T}_i^{\mathrm{cav}} \begin{pmatrix} p_i \\ u_i \end{pmatrix} = \mathbf{T}_{i+1}^{\mathrm{ring}} \mathbf{T}_i^{\mathrm{p}} \mathbf{T}_i^{\mathrm{lm}} \begin{pmatrix} p_i \\ u_i \end{pmatrix} \\
&= \begin{pmatrix} \cos(k_0 h_r) & \mathrm{j}\frac{Z_0}{S_{i+1}} \sin(k_0 h_r) \\ \mathrm{j}\frac{S_{i+1}}{Z_0} \sin(k_0 h_r) & \cos(k_0 h_r) \end{pmatrix} \begin{pmatrix} \cos(k_0 h_i) & \mathrm{j}\frac{Z_0}{S_{i+1}} \sin(k_0 h_i) \\ \mathrm{j}\frac{S_{i+1}}{Z_0} \sin(k_0 h_i) & \cos(k_0 h_i) \end{pmatrix} \\
&\begin{pmatrix} 1 & 0 \\ Y_i^{\mathrm{cav}} & 1 \end{pmatrix} \begin{pmatrix} p_i \\ u_i \end{pmatrix} = \\
&= \begin{pmatrix} \cos[k_0(h_r + h_i)] + \mathrm{j}\frac{Z_0 Y_i^{\mathrm{cav}}}{S_{i+1}} \sin[k_0(h_r + h_i)] & \mathrm{j}\frac{Z_0}{S_{i+1}} \sin[k_0(h_r + h_i)] \\ \mathrm{j}\frac{S_{i+1}}{Z_0} \sin[k_0(h_r + h_i)] + Y_i^{\mathrm{cav}} \cos[k_0(h_r + h_i)] & Y_i^{\mathrm{cav}} \cos[k_0(h_r + h_i)] \end{pmatrix} \begin{pmatrix} p_i \\ u_i \end{pmatrix} \\
&\equiv \mathbf{T}_{i+1}^{\mathrm{rc}} \begin{pmatrix} p_i \\ u_i \end{pmatrix}
\end{aligned}
\tag{3.16}
$$

where the last line contains the definition of the matrix $\mathbf{T}_{i+1}^{\mathrm{rc}}$ that characterizes the effect of the ring plus cavity ensemble on the propagation of the acoustic pressure and the acoustic volume velocity. In (3.16), $h_i = |x_{i+1} - x_i|$ represents the cavity width and $h_r = |x_{i+2} - x_{i+1}|$ the ring thickness, which in the formulation is assumed to be constant for all rings. It has to be noted that, in the limit case of a negligible thickness, that is $h_r \approx 0$, $\mathbf{T}_{i+1}^{\mathrm{ring}}$ reduces to the identity matrix and, consequently, the ring has no influence on the behavior of the retarding structure. Moreover, $S_{i+1} = \pi r_{i+1}$, where r_{i+1} stands for the inner radius of the ring at x_{i+1}, and the admittance Y_i of the cavity is approximated as

$$Y_i^{\mathrm{cav}} = \mathrm{j}\frac{k_0}{Z_0} V_i \ . \tag{3.17}$$

The variable V_i is the volume of the truncated cone which extends from x_i to x_{i+1} (see Figure 3.2)

$$V_i = \pi h_i \Big[R^2 - \frac{1}{3}\Big(r_{i+1}^2 + r_i^2 + r_{i+1}r_i\Big)\Big] \ , \tag{3.18}$$

whose inner surface is given by

$$S_i^{\mathrm{con}} = \pi(r_{i+1} + r_i)\sqrt{h_i^2 + (r_{i+1} - r_i)^2} \ . \tag{3.19}$$

Now, by taking the limit

$$\lim_{x_{i+1}\to x_i} \frac{Y_i^{\mathrm{cav}}}{S_i^{\mathrm{con}}} = -\mathrm{j}\frac{k_0}{Z_0} \lim_{x_{i+1}\to x_i} \frac{\pi h_i \Big[R^2 - \frac{1}{3}\Big(r_{i+1}^2 + r_i^2 + r_{i+1}r_i\Big)\Big]}{\pi(r_{i+1} + r_i)\sqrt{h_i^2 + (r_{i+1} - r_i)^2}} = -\mathrm{j}\frac{k_0}{Z_0}\frac{R^2 - r_i^2}{2r_i} \tag{3.20}$$

which is the value of the local admittance (3.5) used in the governing equation of the ABH. In (3.17) it is implicitly assumed that $k_0 r_i \ll 1$. Taking into account the sizes of the rings and cavities, it is also possible to consider the approximations $\cos(k_0 h_r) \sim \cos(k_0 h_i) \sim 1$, $\sin(k_0 h_r) \sim k_0 h_r$ and $\sin(k_0 h_i) \sim k_0 h_i$ in (3.16).

Finally, given all the obtained results, it is straightforward to relate the state vector at an arbitrary section x_{k+2} with that at $x_i, (k \geq i)$, by means of successive products of matrices $\mathbf{T}_{i+1}^{\mathrm{rc}}$. Given the definition of the transfer matrix,

$$\mathbf{A}(k+2, i) \equiv \prod_{m=1}^{k} \mathbf{T}_{m+1}^{\mathrm{rc}} \ , \tag{3.21}$$

the following can be deduced,

$$\begin{pmatrix} p_{k+2} \\ u_{k+2} \end{pmatrix} = \mathbf{A}(k+2, i) \begin{pmatrix} p_i \\ u_i \end{pmatrix} \ . \tag{3.22}$$

This permits characterizing the whole retarding structure. In fact, if a total number N of rings is considered, the state vector at the entrance $x_N = -L$ of the retarding structure can be linked to that at its termination $x_0 = 0$ through

$$\begin{pmatrix} p_N \\ u_N \end{pmatrix} = \mathbf{A}(N, 0) \begin{pmatrix} p_0 \\ u_0 \end{pmatrix} \ . \tag{3.23}$$

3.3 Consistency of the TMM

3.3.1 The metafluid analogy

The ABH as a power-law density metafluid

Although apparently there is no general consensus on the definition of a metamaterial, or a metafluid, here the one presented in (Cummer *et al*, 2016) will be adopted. In that work, a metafluid is defined as a fluid whose physical properties are built on-demand and without the constraints imposed by nature. This will apply to the considered study. In fact, the particular case of a duct filled with a metafluid (so, non-existent in nature) is introduced. It is taken into consideration a metafluid such that its density increases while approaching the duct end by following the power law (see Figure (3.3))

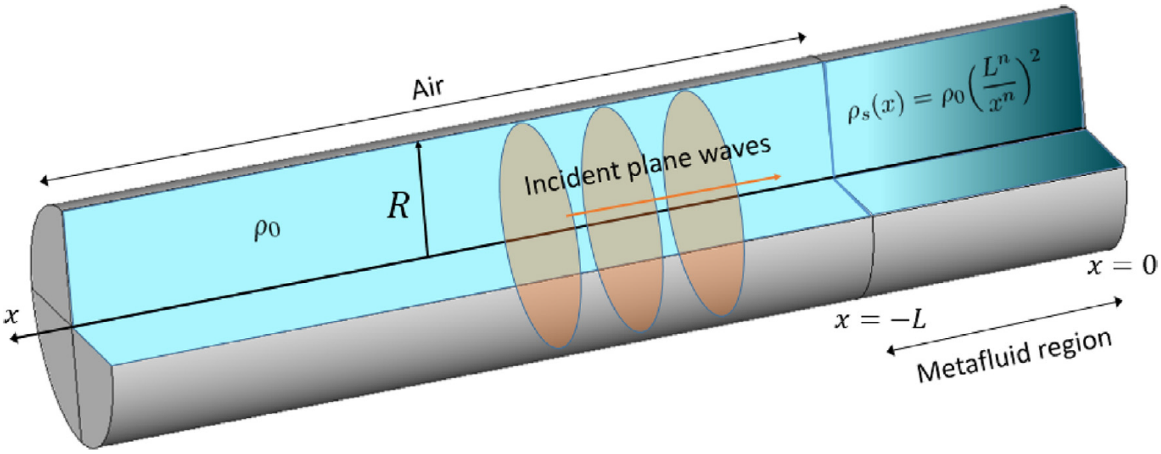

Figure 3.3: Duct termination filled with metafluid whose governing equation is analogous to that of the ABH in Figure (3.1)

$$\rho_s(x) = \rho_0 \left(\frac{L^m}{x^m} \right)^2 . \tag{3.24}$$

It is worth to be noted that the density turns out to be singular at the origin $x = 0$. Next, a constant metafluid compressibility $B_s(x) = B_0$ is assumed, which leads to a sound speed $c_s(x) = \sqrt{B_0/\rho_0(x)}$. Therefore, by making use of the power law (3.24), the squared wavenumber

$$k_s^2(x) = \omega^2 \frac{\rho_s(x)}{B_0} = \left(\frac{k_0 L^m}{x^m} \right)^2 , \tag{3.25}$$

is recovered, where, moreover, the relationship $c_o = \sqrt{B_0/\rho_0}$ has been taken into account. Finally, with the insertion of (3.24) and (3.25) into the equation (3.15) derived in the precedent section, the general ABH equation (3.6) is achieved,

$$\frac{\partial^2 \hat{p}}{\partial x^2} + \frac{2m}{x}\frac{\partial \hat{p}}{\partial x} + \left(\frac{k_0 L^m}{x^m}\right)^2 \hat{p} = 0. \tag{3.26}$$

Thanks to this finding, it can be stated that the governing equation of acoustic wave propagation inside a duct with an inner radius decreasing to zero by following the power law (3.4) and whose wall impedance is given by (3.5), is exactly the same equation describing wave propagation in a metafluid with power-law density (3.24).

On the other hand, an *ad hoc* change of variable is introduced in order to express (3.26) as a Helmholtz equation with space-dependent wavenumber. To this purpose, by considering $\hat{p} = \rho_s^{1/2}\phi$ in (3.15) it is obtained

$$\frac{\partial^2 \phi}{\partial x^2} + k^2(x)\phi = 0 \ , \tag{3.27}$$

where the expression for the wavenumber is

$$k^2(x) = k_s^2(x) - \frac{3}{4\rho_s^2}\left(\frac{\partial \rho_s}{\partial x}\right)^2 + \frac{1}{2\rho_s}\frac{\partial^2 \rho_s}{\partial x^2} \ . \tag{3.28}$$

After performing the substitution of (3.24) and (3.25) into (3.28), the squared wavenumber

$$k^2(x) = \left(\frac{k_0 L^m}{x^m}\right)^2 + \frac{m - m^2}{x^2} \tag{3.29}$$

is obtained. Therefore, solving the ABH (and, as derived and discussed, the metafluid) equation (3.26) is practically the same as solving the Helmholtz equation (3.27) for ϕ, with spatially varying wavenumber (3.29) and, then, the acoustic pressure can be recovered from the change of variable previously introduced, $\hat{p} = \rho_s^{1/2}\phi$.

The smoothness condition for ABHs

A further aspect that has a direct impact on the performance and good functioning of a duct ABH waveguide is now considered. Essentially, if the ABH length L is too short and the power law decay is too steep, a wave entering the ABH volume will not perceive a smooth matching of impedance and, because of the abrupt change of slope, the wave will be partially reflected back. In other words, the ABH waveguide would not be properly functioning. The WKB analysis in (Mironov, 1988) demands the condition

$$\frac{1}{k^2}\frac{dk}{dx} \ll 1 \tag{3.30}$$

to be considered. Inserting (3.29) into (3.30), results in

$$\frac{k_0^2 L^{2m}}{x^{2m}} \gg \frac{m^2}{x^2} \tag{3.31}$$

When $x = L$, which is the most critical case, the smoothness condition implies $k_0 L \gg m$. Such a condition states the logical fact that, in order to get a good impedance matching, the termination length L must be large if the order m of the ABH is high, and vice versa.

As seen, in the case of acoustic wave propagation in an ABH duct termination, the smoothness condition is dictated by the condition required for applying the WKB approximation to the problem (see, Mironov and Pislyakov, 2002). Those are summarized in the fulfillment of

$$|k| \gg \frac{1}{x} \; . \tag{3.32}$$

From (3.29), the wavenuber k is given by

$$k(x) = (-1)^m \frac{L^m}{x^m}\sqrt{k_0^2 - \frac{m^2 x^{2m-2}}{L^{2m}}} \; , \tag{3.33}$$

which, once inserted in (3.32), yields

$$\frac{k_0^2 L^{2m}}{x^{2m}} \gg \frac{m^2+1}{x^2} \; . \tag{3.34}$$

This expression is a slightly more restrictive condition than (3.31). For the proof purpose, a weaker requirement than (3.31) or (3.34) is enough, namely

$$\frac{k_0^2 L^{2m}}{x^{2m}} \gg \frac{m^2-m}{x^2} \; . \tag{3.35}$$

This will become clear in the Section 3.3.3 devoted to the demonstration. Condition (3.35) will be very useful to perform some approximations and make algebraic calculations easier.

3.3.2 The TMM for multilayered media

As mentioned in the Introduction, the TMM is widely used in many areas of physics to study, analyze and simulate the propagation of waves through multilayered media. Therefore, the TMM is an optimum candidate to analyze the performance of the ABH waveguides. However, in many applications of the TMM, the propagation medium exhibits constant physical properties within clearly distinct regions. On the contrary, in the considered case, the physical properties are gradually changing by following a continuous variation. In the next Section it will be proved that such an homogenization process is possible and that the TMM solution of an ABH satisfies a differential equation like (3.6), in the limit of increasing the number of rings-cavity ensembles.

The purpose is to solve the Helmholtz equation (3.27) with varying wavenumber (3.29) making use of the TMM. The region of increasing density is included between $x = -L$ and $x = 0$ and divided into N layers of width L/N and constant physical parameters, as depicted in Figure 3.4. Therefore, the n-th layer is centered at x_n and has constant density ρ_n, speed of sound c_n and characteristic impedance $z_n = \rho_n c_n$. In what follows, the approximate value of any function $g(x)$ at x_n will be indicated as $g_n \approx g(x_n)$. By following the hypotheses and assumptions above, the propagating waves in a layer n will satisfy a standard Helmholtz equation with fixed wavenumber k_n. The solution inside the layer will combine planar incident waves ϕ^i_n and reflected waves ϕ^i_r, whose expressions are

$$\phi^i_n = A_n \mathrm{e}^{\mathrm{j}(\omega t - k_n x_n)}, \quad \phi^r_n = B_n \mathrm{e}^{\mathrm{j}(\omega t + k_n x_n)}, \tag{3.36}$$

and corresponding velocities ϕ^i_n/z_n and $-\phi^r_n/z_n$. The amplitudes $(A_n, B_n)^T$ at the n-th layer can be related to those at the $(n+1)$-th layer $(A_{n+1}, B_{n+1})^T$ by imposing the continuity of ϕ^i, ϕ^r and their velocity at the boundary (see, Carbó, 1997). The mentioned relation is accomplished through a transfer matrix $\mathbf{T}_n$ such that,

$$\begin{pmatrix} A_n \\ B_n \end{pmatrix} = \mathbf{T}_n \begin{pmatrix} A_{n+1} \\ B_{n+1} \end{pmatrix}, \tag{3.37}$$

where $\mathbf{T}_n$ is defined as

$$\mathbf{T}_n = \frac{1}{2z_{n+1}} \begin{pmatrix} (z_{n+1} + z_n)\mathrm{e}^{-\mathrm{j}(k_{n+1} - k_n)x_n} & (z_{n+1} - z_n)\mathrm{e}^{\mathrm{j}(k_{n+1} + k_n)x_n} \\ (z_{n+1} - z_n)\mathrm{e}^{-\mathrm{j}(k_{n+1} + k_n)x_n} & (z_{n+1} + z_n)\mathrm{e}^{\mathrm{j}(k_{n+1} - k_n)x_n} \end{pmatrix}. \tag{3.38}$$

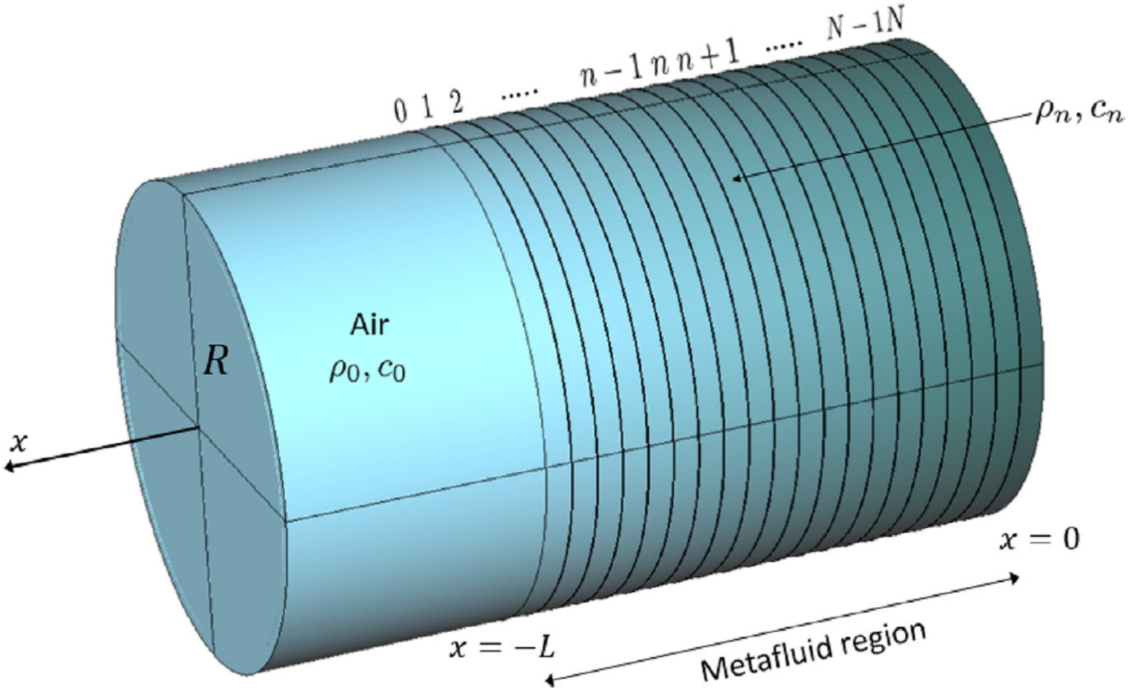

Figure 3.4: Division of the ABH termination into N layers of same width L/N and constant density in order to apply the TMM to describe wave propagation through the metafluid.

Furthermore, a matrix $\bar{\mathbf{T}}_{(n,n+m)}$ that allows one to relate amplitudes between arbitrary layers n and $n+m$ can be defined as

$$\bar{\mathbf{T}}_{(n,n+m)} \equiv \prod_{i=0}^{m-1} \bar{\mathbf{T}}_{(n+i)}, \tag{3.39}$$

from which follows

$$\begin{pmatrix} A_n \\ B_n \end{pmatrix} = \bar{\mathbf{T}}_{(n,n+m)} \begin{pmatrix} A_{n+m} \\ B_{n+m} \end{pmatrix}. \tag{3.40}$$

In particular, the amplitudes $(A_N, B_N)^T$ at the duct termination ($x = 0$) can be related to the amplitudes $(A_0, B_0)^T$ at the entrance of the ABH waveguide ($x = -L$) via

$$\begin{pmatrix} A_0 \\ B_0 \end{pmatrix} = \bar{\mathbf{T}}_{(0,N)} \begin{pmatrix} A_N \\ B_N \end{pmatrix}, \qquad \begin{pmatrix} A_N \\ B_N \end{pmatrix} = \bar{\mathbf{T}}^{\mathbf{-1}}_{(0,N)} \begin{pmatrix} A_0 \\ B_0 \end{pmatrix}. \tag{3.41}$$

3.3.3 Proof of consistency of the TMM solution

Finally, with all the hypotheses, reasoning and developments from the previous sections, the TMM solution can be proved to formally tend to the solution of the ABH equation. First of all, the vector $\tilde{\boldsymbol{\phi}}_n$ for the n-th layer is defined by omitting the factor $\mathrm{e}^{\mathrm{j}\omega t}$ in (3.36),

$$\tilde{\boldsymbol{\phi}}_n = \begin{pmatrix} \phi_n^i \\ \phi_n^r \end{pmatrix} = \begin{pmatrix} A_n \mathrm{e}^{-\mathrm{j}k_n x_n} \\ B_n \mathrm{e}^{\mathrm{j}k_n x_n} \end{pmatrix} = \begin{pmatrix} \mathrm{e}^{-\mathrm{j}k_n x_n} & 0 \\ 0 & \mathrm{e}^{\mathrm{j}k_n x_n} \end{pmatrix} \begin{pmatrix} A_n \\ B_n \end{pmatrix} \equiv \mathbf{D}_n \begin{pmatrix} A_n \\ B_n \end{pmatrix} . \quad (3.42)$$

Now, a relation between $\tilde{\boldsymbol{\phi}}_n$ and $\tilde{\boldsymbol{\phi}}_{n+1}$ is derived through the combination of (3.37) and (3.42),

$$\tilde{\boldsymbol{\phi}}_n = \begin{pmatrix} \phi_n^i \\ \phi_n^r \end{pmatrix} = \mathbf{D}_n \mathbf{T}_n \mathbf{D}_{n+1}^{-1} \begin{pmatrix} \phi_{n+1}^i \\ \phi_{n+1}^r \end{pmatrix} = \mathbf{D}_n \mathbf{T}_n \mathbf{D}_{n+1}^{-1} \tilde{\boldsymbol{\phi}}_{n+1} \; . \quad (3.43)$$

Since the solution ϕ_n at the n-th layer consists of the summation of the incident and the reflected waves, Equation (3.43) permits to write

$$\phi_n = \phi_n^i + \phi_n^r = (1,1) \begin{pmatrix} \phi_n^i \\ \phi_n^r \end{pmatrix} = (1,1)\tilde{\boldsymbol{\phi}}_n = (1,1)\mathbf{D}_n \mathbf{T}_n \mathbf{D}_{n+1}^{-1} \tilde{\boldsymbol{\phi}}_{n+1} \; . \quad (3.44)$$

Next, a second order finite difference scheme for the approximation of the Helmholtz equation (3.27) at point x_{n-1} is considered,

$$\frac{\phi_n - 2\phi_{n-1} + \phi_{n-2}}{(\Delta x)^2} + k_{n-1}^2 \phi_{n-1} = 0, \quad (3.45)$$

where the infinitesimal Δx is taken to coincide with the layer width L/N. The finite difference approximation for the second order derivative of ϕ at x_{n-1}, combined with (3.44), can be expressed as

$$\left.\frac{\partial^2 \phi}{\partial x^2}\right|_{n-1} \approx \frac{\phi_n - 2\phi_{n-1} + \phi_{n-2}}{(\Delta x)^2} = (1,1) \frac{\tilde{\boldsymbol{\phi}}_n - 2\tilde{\boldsymbol{\phi}}_{n-1} + \tilde{\boldsymbol{\phi}}_{n-2}}{(\Delta x)^2}, \quad (3.46)$$

while from (3.43) we derive

$$\tilde{\boldsymbol{\phi}}_{n-1} = \mathbf{D}_{n-1} \mathbf{T}_{n-1} \mathbf{D}_n^{-1} \tilde{\boldsymbol{\phi}}_n \quad (3.47)$$

and

$$\tilde{\boldsymbol{\phi}}_{n-2} = \mathbf{D}_{n-2} \mathbf{T}_{n-2} \mathbf{T}_{n-1} \mathbf{D}_n^{-1} \tilde{\boldsymbol{\phi}}_n \quad (3.48)$$

which, once inserted into (3.46), lead to

$$\left.\frac{\partial^2 \phi}{\partial x^2}\right|_{n-1} \approx \frac{1}{(\Delta x)^2} (1,1)(\mathbf{I} - 2\mathbf{D}_{n-1} \mathbf{T}_{n-1} \mathbf{D}_n^{-1} + \mathbf{D}_{n-2} \mathbf{T}_{n-2} \mathbf{T}_{n-1} \mathbf{D}_n^{-1}) \tilde{\boldsymbol{\phi}}_n, \quad (3.49)$$

where $\mathbf{I}$ stands for the identity matrix. On the other hand, the second term of the discretized Helmholtz equation (3.27) becomes,

$$\begin{aligned} k^2(x_{n-1})\phi_{n-1} &= \left[\left(\frac{k_0 L^m}{x_{n-1}^m}\right)^2 + \frac{m-m^2}{x_{n-1}^2}\right](1,1)\tilde{\boldsymbol{\phi}}_{n-1} = \\ &= \left[\left(\frac{k_0 L^m}{x_{n-1}^m}\right)^2 + \frac{m-m^2}{x_{n-1}^2}\right]\mathbf{D}_{n-1}\mathbf{T}_{n-1}\mathbf{D}_n^{-1}\tilde{\boldsymbol{\phi}}_n. \end{aligned} \tag{3.50}$$

It is already known that the finite difference solution to the Helmholtz equation (3.45) tends to the analytical one (3.27) for $\Delta x \to 0$. Therefore, to verify that the TMM solution also tends to the solution of the continuous problem, (3.49) and (3.50) are substituted into (3.45) and the validity of the following limit is verified,

$$\begin{aligned} \lim_{\Delta x\to 0}\Bigg\{(1,1)\Bigg[\frac{1}{(\Delta x)^2}\mathbf{I} + \left(k_{n-1}^2 - \frac{2}{(\Delta x)^2}\right)\mathbf{D}_{n-1}\mathbf{T}_{n-1}\mathbf{D}_n^{-1} + \\ + \frac{1}{(\Delta x)^2}\mathbf{D}_{n-2}\mathbf{T}_{n-2}\mathbf{T}_{n-1}\mathbf{D}_n^{-1}\Bigg]\tilde{\boldsymbol{\phi}}_n\Bigg\} = 0. \end{aligned} \tag{3.51}$$

The limit (3.51) can be proved through a Taylor series expansion of all the matrix elements involved. For instance, the elements of the matrix $\mathbf{T}_{n-1}$ can be expanded as

$$\begin{aligned} T_{n-1}^{1,1} &= 1 + \frac{2\mathrm{j}mk_0L^mx_n - mx_n^m}{2x_n^{m+1}}\Delta x + \\ &\quad \frac{-2m^2k_0^2L^{2m}x_n^2 - 2\mathrm{j}mk_0L^mx_n^{m+1} + (m^2-m)x_n^{2m}}{4x_n^{2m+2}}(\Delta x)^2 \\ T_{n-1}^{1,2} &= -\frac{m\mathrm{e}^{\left(\frac{2\mathrm{j}S_n}{x_n}\right)}}{2x_n}\Delta x + \frac{(4\mathrm{j}m - 2\mathrm{j}m^2)k_0L^mx_n\mathrm{e}^{\left(\frac{2\mathrm{j}S_n}{x_n}\right)} + x_n^m(m^2-m)\mathrm{e}^{\left(\frac{2\mathrm{j}S_n}{x_n}\right)}}{4x_n^{m+2}}(\Delta x)^2 \\ T_{n-1}^{2,1} &= -\frac{m\mathrm{e}^{\left(-\frac{2\mathrm{j}S_n}{x_n}\right)}}{2x_n}\Delta x + \frac{(2\mathrm{j}m^2 - 4\mathrm{j}m)k_0L^mx_n\mathrm{e}^{\left(-\frac{2\mathrm{j}S_n}{x_n}\right)} + x_n^m(m^2-m)\mathrm{e}^{\left(-\frac{2\mathrm{j}S_n}{x_n}\right)}}{4x_n^{m+2}}(\Delta x)^2 \\ T_{n-1}^{2,2} &= 1 - \frac{2\mathrm{j}mk_0L^mx_n + mx_n^m}{2x_n^{m+1}}\Delta x + \\ &\quad \frac{-2m^2k_0^2L^{2m}x_n^2 + 2\mathrm{j}mk_0L^mx_n^{m+1} + (m^2-m)x_n^{2m}}{4x_n^{2m+2}}(\Delta x)^2 \end{aligned} \tag{3.52}$$

and those of $\mathbf{T}_{n-2}$ become

$$\begin{aligned}
T^{1,1}_{n-2} &= 1 + \frac{2\mathrm{j}mk_0L^mx_n - mx_n^m}{2x_n^{m+1}}\Delta x + \\
&\quad \frac{-2m^2k_0^2L^{2m}x_n^2 + (4\mathrm{j}m^2 - 2\mathrm{j}m)k_0L^mx_n^{m+1} + (m^2-3m)x_n^{2m}}{4x_n^{2m+2}}(\Delta x)^2 \\
T^{1,2}_{n-2} &= -\frac{m\mathrm{e}^{(\frac{2\mathrm{j}S_n}{x_n})}}{2x_n}\Delta x + \frac{(8\mathrm{j}m - 6\mathrm{j}m^2)k_0L^mx_n\mathrm{e}^{(\frac{2\mathrm{j}S_n}{x_n})} + x_n^m(m^2-3m)\mathrm{e}^{(\frac{2\mathrm{j}S_n}{x_n})}}{4x_n^{m+2}}(\Delta x)^2 \\
T^{2,1}_{n-2} &= -\frac{m\mathrm{e}^{(-\frac{2\mathrm{j}S_n}{x_n})}}{2x_n}\Delta x + \frac{(6\mathrm{j}m^2 - 8\mathrm{j}m)k_0L^mx_n\mathrm{e}^{(-\frac{2\mathrm{j}S_n}{x_n})} + x_n^m(m^2-3m)\mathrm{e}^{(-\frac{2\mathrm{j}S_n}{x_n})}}{4x_n^{m+2}}(\Delta x)^2 \\
T^{2,2}_{n-2} &= 1 - \frac{2\mathrm{j}mk_0L^mx_n + mx_n^m}{2x_n^{m+1}}\Delta x + \\
&\quad \frac{-2m^2k_0^2L^{2m}x_n^2 + (2\mathrm{j}m - 4\mathrm{j}m^2)k_0L^mx_n^{m+1} + (m^2-3m)x_n^{2m}}{4x_n^{2m+2}}(\Delta x)^2
\end{aligned} \tag{3.53}$$

In such expressions, it is to be noted that the parameters S_n can be simplified recovering the smoothness condition (3.35), that is

$$S_n = \sqrt{k_0^2L^{2m} + (m-m^2)x_n^{2m-2}} \approx \sqrt{k_0^2L^{2m}} = k_0L^m. \tag{3.54}$$

Moreover, for the linear case (3.49) no approximation is needed because, since $m = 1$, we have $m - m^2 = 0$. Now, the fulfillment of the limit (3.51) can be checked. Inserting the expressions (expanded by means of Taylor series) for all matrices $\mathbf{T}$, as well as the corresponding expansions of $\mathbf{D}_{n-1}$, $\mathbf{D}_{n-2}$ and $\mathbf{D}_n^{-1}$ requires a big amount of algebraic manipulations. These have been mostly handmade and checked with the PARI-GP mathematical software. The final step to conclude the demonstration consists in reverting the change of variable $\phi = \rho_s^{-1/2}\hat{p}$ and checking if the TMM solution for the acoustic pressure $\hat{p}_n$ satisfies the ABH equation, in the limit $\Delta x \to 0$. The pressure at the n-th layer is

$$\hat{p}_n = \hat{p}_n^i + \hat{p}_n^r = \rho_s^{1/2}(x_n)(\phi_n^i + \phi_n^r) = \rho_0^{1/2}\frac{L^m}{x_n^m}(\phi_n^i + \phi_n^r), \tag{3.55}$$

where matrix expressions analogous to (3.43), (3.47) and (3.48) for the acoustic pressure can be derived, namely

$$\begin{aligned}\tilde{\mathbf{P}}_n = \begin{pmatrix}\hat{p}_n^i\\ \hat{p}_n^r\end{pmatrix} = \rho_s^{1/2}(x_n)\begin{pmatrix}\phi_n^i\\ \phi_n^r\end{pmatrix} &= \frac{\rho_s^{1/2}(x_n)}{\rho_s^{1/2}(x_{n+1})}\mathbf{D}_n\mathbf{T}_n\mathbf{D}_{n+1}^{-1}\begin{pmatrix}\hat{p}_{n+1}^i\\ \hat{p}_{n+1}^r\end{pmatrix} = \\ &= \frac{x_{n+1}^m}{x_n^m}\mathbf{D}_n\mathbf{T}_n\mathbf{D}_{n+1}^{-1}\tilde{\mathbf{P}}_{n+1},\end{aligned} \tag{3.56}$$

$$\tilde{\mathbf{P}}_{n-1} = \frac{x_n^m}{x_{n-1}^m}\mathbf{D}_{n-1}\mathbf{T}_{n-1}\mathbf{D}_n^{-1}\tilde{\mathbf{P}}_n, \tag{3.57}$$

and

$$\tilde{\mathbf{P}}_{n-2} = \frac{x_{n-1}^m}{x_{n-2}^m}\mathbf{D}_{n-2}\mathbf{T}_{n-2}\mathbf{D}_{n-1}^{-1}\tilde{\mathbf{P}}_{n-1} = \frac{x_n^m}{x_{n-2}^m}\mathbf{D}_{n-2}\mathbf{T}_{n-2}\mathbf{T}_{n-1}\mathbf{D}_n^{-1}\tilde{\mathbf{P}}_n. \tag{3.58}$$

A second order finite difference approximation for (3.6) at point x_{n-1} is

$$\frac{\hat{p}_n - 2\hat{p}_{n-1} + \hat{p}_{n-2}}{(\Delta x)^2} + \frac{2m}{x_{n-1}}\frac{\hat{p}_n - \hat{p}_{n-2}}{2\Delta x} + \left(\frac{k_0 L^m}{x_{n-1}^m}\right)^2 \hat{p}_{n-1} = 0. \tag{3.59}$$

The first and third terms of (3.59) can be treated analogously to those of (3.45). The second term involves the first order derivative of the pressure at point x_{n-1},

$$\left.\frac{\partial \hat{p}}{\partial x}\right|_{n-1} \approx \frac{\hat{p}_n - \hat{p}_{n-2}}{2\Delta x} = \frac{1}{2\Delta x}(1,1)\mathbf{D}_{n-2}\left(\mathbf{D}_{n-2}^{-1}\mathbf{D}_n - \frac{x_n^m}{x_{n-2}^m}\mathbf{T}_{n-2}\mathbf{T}_{n-1}\right)\mathbf{D}_n^{-1}\tilde{\mathbf{P}}_n. \tag{3.60}$$

In order to prove that the discretized $\hat{p}_n$ tends to the continuous pressure $\hat{p}$ of the ABH equation when $\Delta x \to 0$, the following limit needs to hold

$$\begin{aligned}\lim_{\Delta x\to 0}\Bigg\{(1,1)\Bigg[&\frac{1}{(\Delta x)^2}\left(\mathbf{I} - 2\frac{x_n^m}{x_{n-1}^m}\mathbf{D}_{n-1}\mathbf{T}_{n-1}\mathbf{D}_n^{-1} + \frac{x_n^m}{x_{n-2}^m}\mathbf{D}_{n-2}\mathbf{T}_{n-2}\mathbf{T}_{n-1}\mathbf{D}_n^{-1}\right) + \\ &+ \frac{m}{x_{n-1}\Delta x}\left(\mathbf{I} - \frac{x_n^m}{x_{n-2}^m}\mathbf{D}_{n-2}\mathbf{T}_{n-2}\mathbf{T}_{n-1}\mathbf{D}_n^{-1}\right) + \\ &+ \frac{k_0^2 L^{2m}}{x_{n-1}^{2m}}\left(\frac{x_n^m}{x_{n-1}^m}\mathbf{D}_{n-1}\mathbf{T}_{n-1}\mathbf{D}_n^{-1}\right)\Bigg]\tilde{\mathbf{P}}_n\Bigg\} = 0\ .\end{aligned} \tag{3.61}$$

As explained above, the limit can be verified by means of Taylor series expansions of the elements in matrices $\mathbf{T}_{n-1}$, $\mathbf{T}_{n-2}$, $\mathbf{D}_{n-1}$, $\mathbf{D}_{n-2}$ and $\mathbf{D}_n^{-1}$. Once again, the involved algebraic manipulations have been performed mostly by hand and checked with the mathematical software PARI-GP (Batut *et al.*, 2000). The proof of the validity of the limit concludes the demonstration.

3.4 Numerical results

3.4.1 The ABH reflection coefficient

The performance of an ABH is generally measured by means of the reflection coefficient at its entrance $x = -L$. The reflection coefficient can be calculated once the exact solution of the ABH equation (3.6), therefore to its metafluid analogue, is known. These solutions have been respectively derived for the linear ABHs ($m = 1$) and quaratic ABHs ($m = 2$) in (Mironov and Pislyakov, 2002; Guasch *et al.*, 2017). The solution to the equation (3.6) for $m = 1$ is given by

$$p(x) = C_+ \mathrm{e}^{\alpha_+ \ln x} + C_- \mathrm{e}^{\alpha_- \ln x} \tag{3.62}$$

where C_+ and C_- are real constants and

$$\alpha_\pm = \frac{1}{2}\left[-1 \pm \sqrt{1-(2k_0 L)^2} \right]. \tag{3.63}$$

Besides, the solution for the case $m = 2$ is

$$\begin{aligned} p(x) = {} & \frac{C_+}{x}\sqrt{(k_0L^2)^2 + x^2}\exp\left\{ \mathrm{j}\left[\frac{k_0L^2}{x} - \arctan\left(\frac{k_0L^2}{x}\right)\right]\right\} \\ & + \frac{C_-}{x}\sqrt{(k_0L^2)^2 + x^2}\exp\left\{ -\mathrm{j}\left[\frac{k_0L^2}{x} - \arctan\left(\frac{k_0L^2}{x}\right)\right]\right\}. \end{aligned} \tag{3.64}$$

Now, it is possible to calculate the linear and quadratic reflection coefficients at $x = -L$, denoted respectively as R_L^{lin} and R_L^{quad}, in terms of those at $x = 0$, R_0^{lin} and R_0^{quad}, by imposing the continuity of pressure and velocity at the ABH entrance, with the use of (3.62) and (3.64), and prescribing a boundary admittance Y_0 at the ABH termination. However, since the ABH equation is singular at the origin, a small imperfection l needs to be introduced and, therefore, Y_0, R_0^{lin} and R_0^{quad} are replaced by Y_l, R_l^{lin} and R_l^{quad}. For the sake of completeness, the reflection coefficient for the linear case at the ABH entrance is given by the expression

$$R_L^{\text{lin}} = \frac{1 + R_l^{\text{lin}} + \frac{1}{\mathrm{j}k_0L}(\alpha_+ + R_l^{\text{lin}}\alpha_-)}{1 + R_l^{\text{lin}} - \frac{1}{\mathrm{j}k_0L}(\alpha_+ - R_l^{\text{lin}}\alpha_-)}\mathrm{e}^{-2\mathrm{j}k_0L}, \tag{3.65}$$

with the reflection coefficient at $x = -l$, R_l^{lin}, being

$$R_l^{\text{lin}} = -\frac{\alpha_+ + \mathrm{j}k_0Z_0lY_l}{\alpha_- + \mathrm{j}k_0Z_0lY_l}\left(\frac{l}{L}\right)^{\alpha_+-\alpha_-}. \tag{3.66}$$

It is worth noting that, in case a rigid end wall condition for the ABH needs to be implemented, $Y_l = 0$ in (3.66) has to be considered. Analogously, the reflection coefficient for the quadratic case becomes

$$R_L^{\text{quad}} = \frac{R_l^{\text{quad}}\mathrm{e}^{\mathrm{j}k_0L} - \mathrm{e}^{-\mathrm{j}k_0L}(1 + 2\mathrm{j}k_0L)}{R_l^{\text{quad}}\mathrm{e}^{\mathrm{j}k_0L}(1 - 2\mathrm{j}k_0L) - \mathrm{e}^{-\mathrm{j}k_0L}}\mathrm{e}^{-2\mathrm{j}k_0L}, \tag{3.67}$$

where

$$R_l^{\text{quad}} = \frac{Y_l + \mathrm{j}\frac{k_0L^2}{l}(Y_l + \frac{L^2}{Z_0l^2})}{Y_l - \mathrm{j}\frac{k_0L^2}{l}(Y_l - \frac{L^2}{Z_0l^2})}\mathrm{e}^{-2\mathrm{j}\frac{k_0L^2}{l}}. \tag{3.68}$$

When using the TMM approach, the expression for the reflection coefficient at $x = -L$ can be easily obtained from (3.41). In fact, by considering a rigid termination, the relationship $B_N = -A_N$ is obtained, from which follows,

$$R_L^{TMM} = \frac{\bar{T}_{0,N}^{21} - \bar{T}_{0,N}^{22}}{\bar{T}_{0,N}^{11} - \bar{T}_{0,N}^{12}}. \tag{3.69}$$

3.4.2 Numerical simulations

Now that all the formulations have been derived, few particular cases are chosen and it is checked that the TMM reflection coefficient R_L^{TMM} in (3.69) tends to the exact ones, R_L^{lin} in (3.65) and R_L^{quad} in (3.67), when the number of layers of the metafluid increases. For the simulations, a cylindrical duct with radius $R = 0.23$ m and $L = 0.5$ m both for the linear and the quadratic cases is considered. The cutoff frequency of the tube is $f_c = 1.84c_0/2\pi R = 445$ Hz, where $c_0 = 340$ m/s stands for the speed of sound. Damping has been introduced by consider a complex speed of sound, $c_0 = c_0(1 + 0.05\mathrm{j})$ (see,

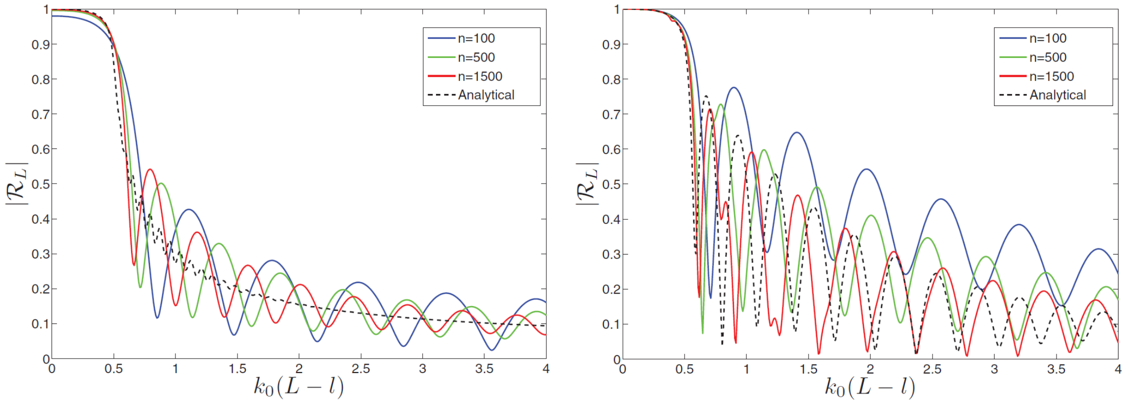

(a) Linear ($m=1$), $L=0.5$ m, $l=5\times10^{-15}$m (b) Linear ($m=1$), $L=0.5$ m, $l=5\times10^{-5}$m

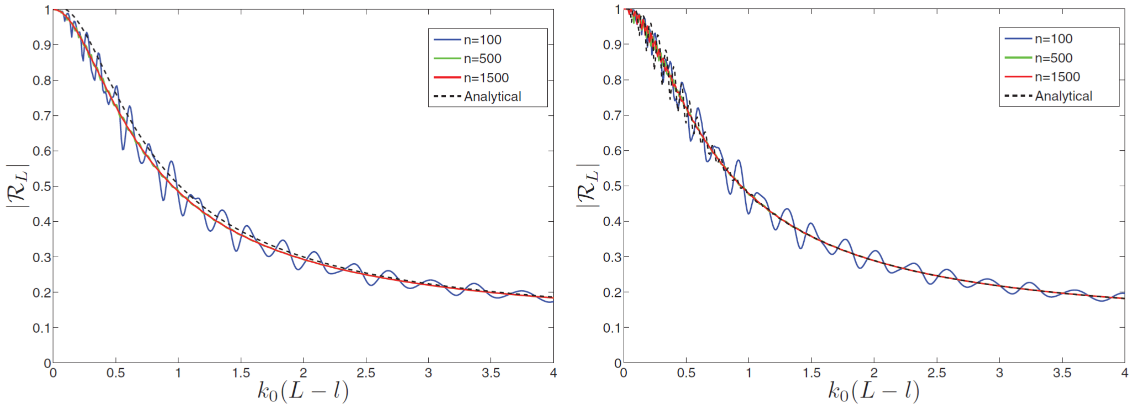

(c) Quadratic ($m=2$), $L=0.5$ m, $l=5\times10^{-5}$m (d) Quadratic ($m=2$), $L=0.5$ m, $l=1\times10^{-2}$m

Figure 3.5: Comparison between analytical and TMM reflection coefficients for the linear (a)-(b) and quadratic (c)-(d) ABHs.

Mironov and Pislyakov, 2002; Guasch *et al.*, 2017). In Figures 3.5(a) and 3.5(b), the analytical and TMM reflection coefficients for the linear ABH when varying the number of TMM layers are presented. Figure 3.5(a) shows the values of R_L^{lin} and R_L^{TMM} respectively for 100, 500 and 1500 layers. As noted, the TMM reflection coefficients tend to the analytical one, although very slowly. It is to be observed that the TMM reflection coefficients have been computed by assuming a very small imperfection $l = 5\times10^{-15}$ m at the end of the ABH, which implies just a few oscillations of the analytical solution. Moreover, the critical value for the smoothness condition (3.30) occurs at $k_0 l = 1$, so the ABH performs well (that is, low values for the reflection coefficient) only when passed such value. In 3.5(b) a higher value of $l = 5\times10^{-5}$ has been considered and this highlights a very important aspect. In fact, although the magnitude of l and its small variations can be neglected from a manufacturing point of view, they can extremely influence the performance of the linear ABH. As for the second order ABHs, in 3.5(c) it can be appreciated that the TMM solutions tend to the analytical one much faster for the quadratic ABH than for the linear one. Moreover, the performance of the quadratic ABH is shown to be more robust to the small imperfection l than the linear one; for the same value used in 3.5(b), that is $l = 5 \times 10^{-5}$, R_L^{quad} does not exhibit any oscillation. The value of l needs to be increased up to $l = 1 \times 10^{-2}$ (see 3.5(d)) to visualize some fluctuations in the reflection coefficient. Finally, it has to be noted that, for the quadratic case, the critical value for the smoothness condition is $k_0 L = 2$, so a larger length L than the linear case would be necessary to achieve a low reflection coefficient for the same frequency.

3.5 Conclusions

The consistency of using the transfer matrix method (TMM) to simulate the performance of acoustic black holes (ABHs) in duct terminations has been analyzed and proved. In particular, a discrete ABH termination, that is a retarding structure made of rings and cavities with a power-law decreasing inner radius, has been considered and the formal convergence of its TMM solution to the analytical one has been demonstrated. In order to do that, some crucial conceptual steps need to be followed.

First of all, the governing equations for an ABH termination and for plane waves in a duct filled with a non-homogeneous fluid have been introduced and explained, followed by a revision and a contextualization of the classical TMM for acoustic filters. Second, the analogy between the discrete ABH and a metafluid whose density increases while approaching the duct termination has been proved. Such fact has been extremely important, because it leads to significant simplifications of the proof, while opening new possibilities for a framework of future ABH designs. Third, the metafluid equation has been manipulated and transformed into a Helmholtz equation with varying wavenumber. This has strongly simplified the TMM approach and the related calculations. In fact, this allows to consider the discretization of the metafluid into layers with constant physical magnitudes, with planar acoustic waves propagating in them, providing a particularly simple form for the transfer matrices. Then, a second order finite difference approximation has been applied to the Helmholtz equation and the TMM solution has been substituted in this newly discretized equation. The proof of the fulfillment of the differential Helmholtz equation has been performed with the help of a Taylor series expansion of all the matrix elements involved in the formulation and with the use of the ABH smoothness condition. Finally, some numerical results for the reflection coefficients of the linear and quadratic ABHs have been presented. The simulations show that the TMM solutions tend to the analytical ones, very slowly for the linear cases and much faster for the quadratic ones.

Chapter 4

Finite element simulations of the linear and quadratic ABH in duct terminations

In this chapter, FEM simulations will be used to further analyze ABHs in duct terminations. While the Transfer Matrix Method (TMM) used in Chapter 3 is a fast manner to analyze the qualitative behavior of ABHs, it relies on some restrictive hypotheses. Although only wall losses will be considered for the simulations, FEM results have a higher computational cost but they will provide insights closer to the real phenomenon. The influence of many parameters on the ABH performance will be analyzed and the wave propagation and absorption inside the retarding structure will be visualized. Finally, the fundaments of the ABH behavior, that is different cavities responsible for the absorption of certain frequency ranges, will be derived.

Concerning implementation aspects, an in-house finite element software based on Fortran language has been used. Moreover, the generation of ABH geometries, the finite element meshes and the postprocessing of simulation results have been done using GID (`http://gidhome.com/`) and Matlab.

This chapter is mainly based on the following work:

- Davide Ghilardi, Marc Arnela and Oriol Guasch (2018), ”Finite element simulations of the acoustic black hole effect in duct terminations”, Proceedings of the Noise and Vibration Emerging Methods, NOVEM2018, Santa Eulària des Riu, Ibiza, Spain, 257, pp. 887-897.

4.1 Introduction

The acoustic black hole (ABH) effect is a fairly new technique for sound and vibrations control and reduction and, traditionally, it has been deeply studied and analyzed for beams and plates. Later, Mironov and Pislyakov (Mironov and Pislyakov, 2002) proposed a structure capable to reach that effect, made of rings with decreasing inner radii separated by air cavities and placed at the end of a duct. From a theoretical point of view, the necessary time for a wave to reach the duct termination should be infinite, so that no reflections might be expected. However, in practice, waves are partially reflected from the ABH since many of the hypotheses of Mironov and Pislyakov's model cannot be fulfilled. Practical realizations of the structure proposed in (Mironov and Pislyakov, 2002) have been built and analyzed in (El Ouahabi *et al.*, 2015; El Ouahabi *et al.*, 2015b). The discrepancies found between the manufactured prototypes and the expected theoretical behavior lead to the use of alternative strategies and methods to study the effects of the discretization of the continuous ABH, such as the number of rings, their thickness, etc. In particular, the transfer matrix method (TMM) has been used in (Guasch *et al*, 2016b, Guasch *et al*, 2017), while in (Guasch *et al*, 2020) it has been shown, for any ABH of order m, that the TMM solution recovers the analytical one when the number of rings and cavities tends to infinity. Moreover, the TMM has also been used to analyze duct mufflers inspired on the ABH effect (Sharma *et al*, 2016, Sharma *et al*, 2017). Although the TMM method is a very useful tool for qualitative and fast approaches to ABHs, it relies on some assumptions which impede to get a deep understanding of the physics governing the ABH behavior. This is the reason behind the choice of performing direct FEM simulations of the acoustics inside the ABH. It has to be noted that, after the publication of the work corresponding to the main reference of this chapter, new research arised and explanation of observed phenomena have been provided. In particular, in (Cervenka and Bednarík, 2022), thermoviscous losses are taken into account in the FEM solution of the linearized Navier-Stokes equations. In this case, the ABH is behaving as a rainbow trapping absorber (see Jiménez *et al.*, 2017). Thanks to this, the comprehension of the ABH is improved, compared with the works based on the solution of the Helmholtz equation. Also, it has been observed that the acoustic energy absorption is related with the resonance of the annular cavities between rings. Moreover, in (Mousavi *et al.*, 2022) it has been shown that the addition of damping material at the end of the ABH does not imply an improvement in the absorption process, as already observed experimentally in (El Ouahabi *et al.*, 2015; El Ouahabi *et al.*, 2015b), while using thermoviscous losses in the cavities reduces the reflection coefficient at all the frequencies. Moreover, it is showed that at high frequencies the pressure distribution inside ABH cavities is not uniform, meaning that cavity resonances appear. As a consequence of this, it is shown that adding a small amount of damping material at the end of each cavity (at the outer tube) reduces drastically the reflection coefficient at all frequencies. In this chapter, Section 4.2 opens with the resolution of the standard wave equation in mixed form for the cases of linear and quadratic three-dimensional ABH geometries. The FEM simulation will allow to observe from one side how the ABH effect works and, for the other, how waves propagate inside the ABH. In fact, thanks to a numerical adaptation of the experimental two-microphone transfer function method (TMTF), the reflection coefficient, which is the key measure of an ABH performance, can be computed. Finally, many numerical results will show the influence on the ABH performance of parameters such as number of rings and absorption at walls, and the pressure distribution inside the ABH.

4.2 Methodology

4.2.1 The wave equation in mixed form

Traditionally, when dealing with problems related to waves, it is common to consider the wave equation in its irreducible form. By considering a single scalar unknown, the acoustic pressure, p, depending on the spatial variable $\mathbf{x}$ and on time t, the wave equation is

$$\frac{\partial^2 p}{\partial t^2} - c^2 \Delta p = f \ , \tag{4.1}$$

where c is the speed of sound, f stands for the forcing term and Δ denotes the Laplace operator. This equation needs to be solved in a certain domain so it has to be complemented with some boundary and initial conditions. However, in some cases it can be useful to rewrite (4.1) in mixed form (mass and momentum conservation equations), which means considering the solution for p and the acoustic velocity vector $\mathbf{u}(\mathbf{x},t)$ of the problem

$$\mu_p \partial_t p + \nabla \cdot \mathbf{u} = f_p, \tag{4.2a}$$

$$\mu_u \partial_t \mathbf{u} + \nabla p = \mathbf{f}_u, \tag{4.2b}$$

where μ_p and μ_u are coefficients that have to satisfy $c^2 = (\mu_p \mu_u)^{-1}$ and the forcing terms f_p and $\mathbf{f}_u$ are such that $\mu_u \partial_t f_p - \nabla \cdot \mathbf{f}_u = f$.

4.2.2 Finite Element simulations

We used the stabilized FEM strategy described in (Codina, 2008; Guasch *et al.*, 2016) in order to solve the mixed wave equation for the acoustic pressure $p(\mathbf{x},t)$ and the acoustic particle velocity $\mathbf{u}(\mathbf{x},t)$ for waves propagating inside a circular duct with an ABH termination at one of its end (see Figure 4.1). The mixed wave equation has the form,

$$\frac{1}{\rho_0 c_0^2} \partial_t p + \nabla \cdot \mathbf{u} = 0, \tag{4.3a}$$

$$\rho_0 \partial_t \mathbf{u} + \nabla p = 0, \tag{4.3b}$$

and it has been complemented with the following boundary and initial conditions:

$$\mathbf{u} \cdot \mathbf{n} = p/Z_{w_1} \qquad \text{on } \Gamma_Z, t > 0, \tag{4.3c}$$

$$\mathbf{u} \cdot \mathbf{n} = p/Z_{w_2} \qquad \text{on } \Gamma_R, t > 0, \tag{4.3d}$$

$$\mathbf{u} \cdot \mathbf{n} = g(t) \qquad \text{on } \Gamma_G, t > 0, \tag{4.3e}$$

$$\mathbf{u} \cdot \mathbf{n} = 0 \qquad \text{on } \Gamma_L, t > 0, \tag{4.3f}$$

$$p = 0, \ \mathbf{u} = 0 \qquad \text{in } \Omega, t = 0. \tag{4.3g}$$

In Equation (4.3), $\mathbf{n}$ stands for the unitary vector normal to the considered surface, ∂_t represents the first partial time derivative and Ω the computational domain with boundary $\Gamma = \Gamma_G \cup \Gamma_Z \cup \Gamma_R \cup \Gamma_L$ (see Figure 4.1).

With respect to the boundary conditions, in Equation (4.3c)-(4.3d) the impedances Z_{w_1} and Z_{w_2} are responsible for introducing losses on the walls Γ_Z and Γ_R, respectively. Such magnitudes are related with the boundary admittance coefficient μ as $\mu = \rho_0 c_0 / Z_w$. In Equation (4.3e) a particle velocity $g(t)$ is imposed at the duct entrance Γ_G, in order to generate acoustic waves within the tube. In particular, the following Gaussian pulse is used

$$u_g(t) = \mathrm{e}^{-[(t-T_{gp})/0.29T_{gp}]^2} [\mathrm{m/s}], \tag{4.4}$$

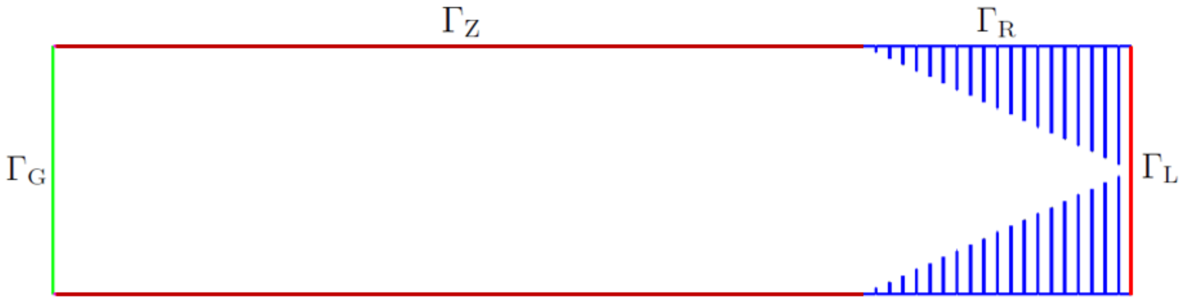

Figure 4.1: Two-dimensional view of the computational domain.

with $T_{gp} = 0.646/f_c$ and $f_c = 10$ kHz. To avoid numerical errors at high frequencies, a low-pass filter has been applied to the pulse, that carries energy for all frequencies, limiting it to 10 kHz. It has to be noted that the model considered in Equation (4.3) does not account for thermoviscous losses, while in the TMM results from Chapter 3 such losses are considered by means of a complex speed of sound. In this chapter, the only losses taken into account are wall losses. Therefore, the results obtained with TMM in 3 and with FEM in the current chapter cannot be directly compared since losses come from different physical phenomena. The model expressed in Equation (4.3) could be improved and made more complete and closer to reality by considering other types of losses (see, Mousavi *et al.*, 2022).

4.2.3 The two microphone transfer function method

The performance of an ABH is generally measured and expressed in terms of its reflection coefficient. Even though analytical expressions exist for theoretical models or the TMM approach, we need to compute it from the outputs of the FEM simulations. We will do so by following the strategy contained in (Arnela and Guasch, 2013), which adapts the experimental two-microphone transfer function method (TMTF) to the numerical context. Essentially, the procedure consists of a few steps. First, plane waves are generated at the beginning of the circular duct, propagate in the duct and enter the ABH (see Figure 4.2). In our experiments, the duct is 1.5 m long and has a radius of $R = 0.23$ m, so that plane waves are guaranteed up to about the cutoff frequency $f_c = 445$ Hz ($f_c = 1.84 c_0/(2\pi R)$). The ABH termination has the same radius and a length of 0.5 m. Second, two virtual microphones are located in the center line of the duct, at a distance of $s = 0.15$ m, the closer one

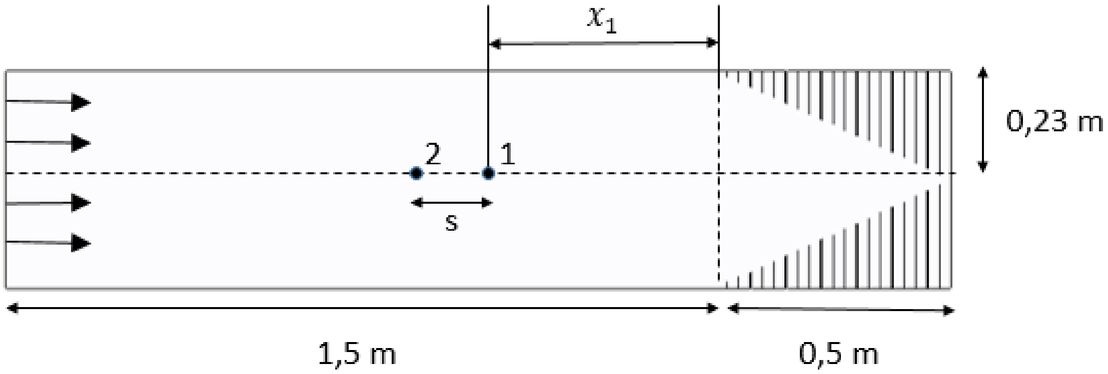

Figure 4.2: Sketch of the circular duct with an ABH termination at its right end.

(i.e., microphone #1 in Figure 4.2) being at a distance of $x_1 = 0.5$ m from the ABH entrance. It needs to be noted that the microphone separation also limits the application range of the TMTF for higher frequencies. In this case, such distance gives an upper frequency limit of 1167 Hz ($s = 0.5\lambda_{min}$), beyond the plane wave propagation restriction also required by this method. A 100 ms simulation is then performed to solve the mixed wave equation (4.3), setting the speed of sound to $c_0 = 350$ m/s and the sampling frequency to $f_s = 1/\Delta t = 20$ kHz. The computational domain is meshed by using unstructured tetrahedra, with an element size of $h = 0.04$ m for the impedance tube and $h = \{0.01, 0.004\}$ m for the ABH. The acoustic pressure evolution $p_1(t)$ and $p_2(t)$ at the two points #1 and #2 (see Figure 4.2) is tracked as sound waves propagate within the duct and the ABH. This permits to compute the transfer function $H_{12}(f)$ between the two microphones as

$$H_{12}(f) = \frac{P_2(f)}{P_1(f)}, \tag{4.5}$$

with $P_1(f)$ and $P_2(f)$ standing for the Fourier transform of pressure signals $p_1(t)$ and $p_2(t)$, respectively. The reflection coefficient $\mathcal{R}$ is finally obtained as (Arnela and Guasch, 2013)

$$\mathcal{R} = \frac{H_{12} - \mathrm{e}^{-\mathrm{j}k_z s}}{\mathrm{e}^{\mathrm{j}k_z s} - H_{12}} \, \mathrm{e}^{\mathrm{j}2k_z x_1}, \tag{4.6}$$

k_z standing for the complex wave number within the duct. This can be computed from the boundary admittance coefficient μ_{w_1} imposed at the duct walls as

$$k_z = k_0 \sqrt{1 - \mathrm{j}\frac{2\mu_{w_1}}{k_0 R}}. \tag{4.7}$$

As already mentioned, a circular duct of constant radius $R = 0.23$ m and length $L = 1.5$ m is considered. At its right end the ABH termination is located to be analyzed. This structure has a fixed length of $l = 0.5$ m and it is made of rigid rings separated by air cavities that follow a power-law decreasing inner radius $r(x)$ (see in Figure 4.2 a 2D section of the geometry). Equally spaced rings of constant thickness $h_r = 1$ mm are considered. Four different retarding structures consisting of linear and quadratic ABHs with 20 and 40 rings each one are taken into account. Two-dimensional sections of the tested ABHs are represented in Figure 4.3. With respect to the wall losses, the circular duct boundary admittance coefficient μ_{w_1} is always set to $\mu_{w_1} = 0.005$, while the boundary admittance coefficient for the ABH can be $\mu_{w_2} = \{0.0001, 0.0005, 0.001, 0.005\}$, depending on the particular case considered. For the sake of simplicity, in the following sections μ_{w_2} will be simply denoted by μ.

4.3 Results of the FEM simulations

4.3.1 Influence of the number of rings and of the ABH order

The performance of different ABHs is studied by computing the corresponding reflection coefficient. In order to do that, the boundary admittance coefficient at ABH walls μ is fixed to the value $\mu = 0.0005$, while other parameters, such as the number of rings and the exponent in the power law governing their inner radii, will vary. The influence of the number of rings on the absolute value of the reflection coefficient $|\mathcal{R}|$ is shown in Figure 4.4. As it can be seen in Figure 4.4(a) for the linear ABH, the case with $N = 40$ rings presents lower values than the 20 rings one, especially at high frequencies. Moreover, a higher number of rings also brings more oscillations in the $|\mathcal{R}|$ value. Such remarks are also valid for the quadratic case shown in Figure 4.4(b), where it can be appreciated that this ABH has much more oscillations than its linear counterpart (where the explanation for this phenomenon has been already provided in Chapter 2). Additionally, the quadratic ABH is performing better than the linear one, since it is achieving lower values for its reflection coefficient, especially with the highest number of rings. In fact, when increasing the number of rings, the absorption area is getting bigger, which leads to a better ABH performance, although this could be detrimental from the manufacturing point of view.

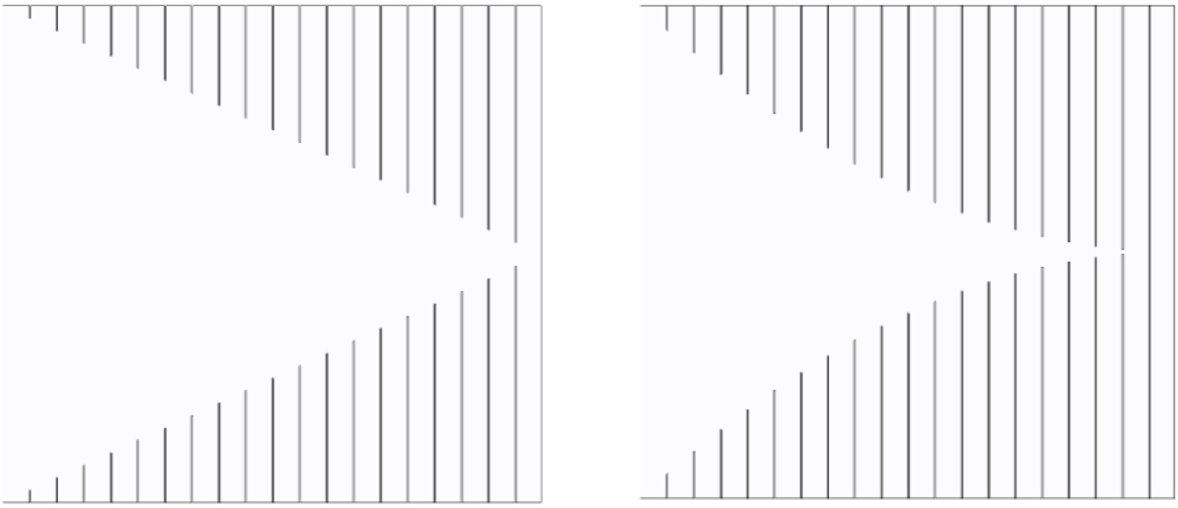

(a) Linear ABH with $N = 20$ rings (b) Quadratic ABH with $N = 20$ rings

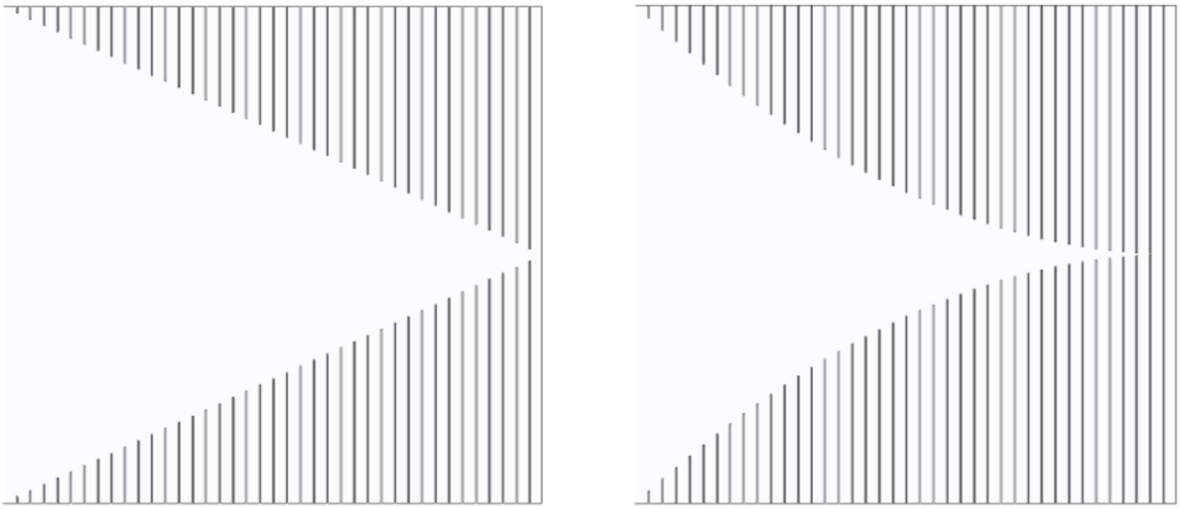

(c) Linear ABH with $N = 40$ rings (d) Quadratic ABH with $N = 40$ rings

Figure 4.3: Tested geometries: linear and quadratic ABHs with $N = 20$ and $N = 40$ rings.

4.3.2 Influence of the boundary admittance coefficient

Now, the effect of the variation of the boundary admittance coefficient μ at ABH walls on its reflection coefficient $|\mathcal{R}|$ is analyzed. Four different ABHs (linear and quadratic, both with $N = 20$ and $N = 40$ rings) are tested, while the following values are considered $\mu = \{0.0001, 0.0005, 0.001, 0.005\}$. In Figure 4.5, $|\mathcal{R}|$ against frequency is plotted for all the configurations considered. As it can be observed, the boundary admittance coefficient μ plays a fundamental role in the absorption process. In all the four cases considered,

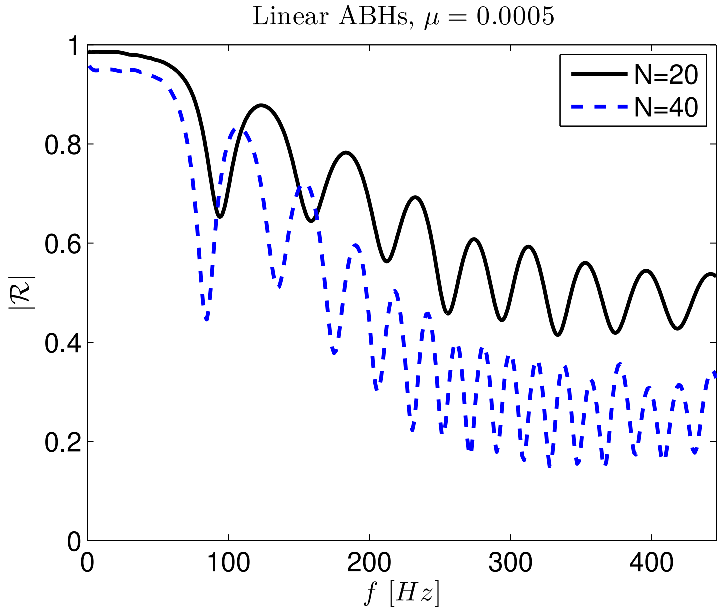

(a)

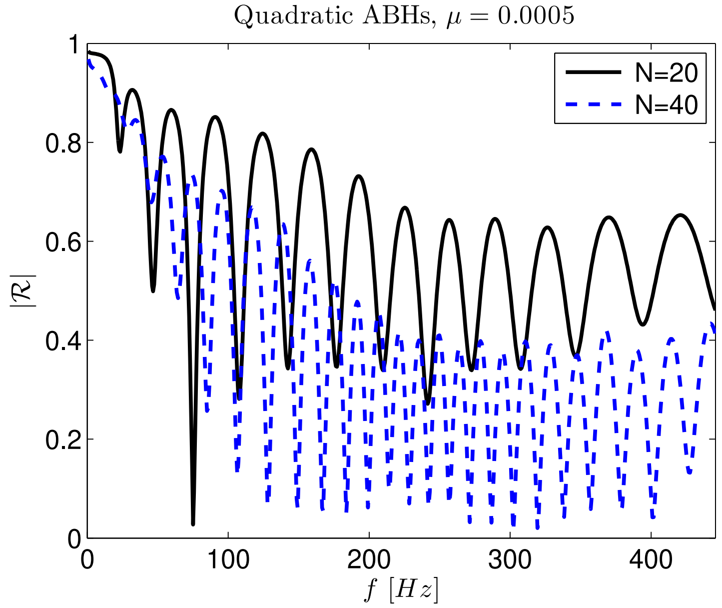

(b)

Figure 4.4: Influence of the number of rings on $|\mathcal{R}|$ for the linear (a) and quadratic (b) cases.

smaller values for the reflection coefficient are obtained when μ is increasing, as one might expect. Besides, when μ is large enough, the oscillations in the $|\mathcal{R}|$ behavior almost disappear (see the 40 rings ABHs for $\mu = 0.005$ in Figures 4.5(c) and 4.5(d)). Moreover, when considering low values for μ, it can be appreciated that the quadratic cases perform better than the linear

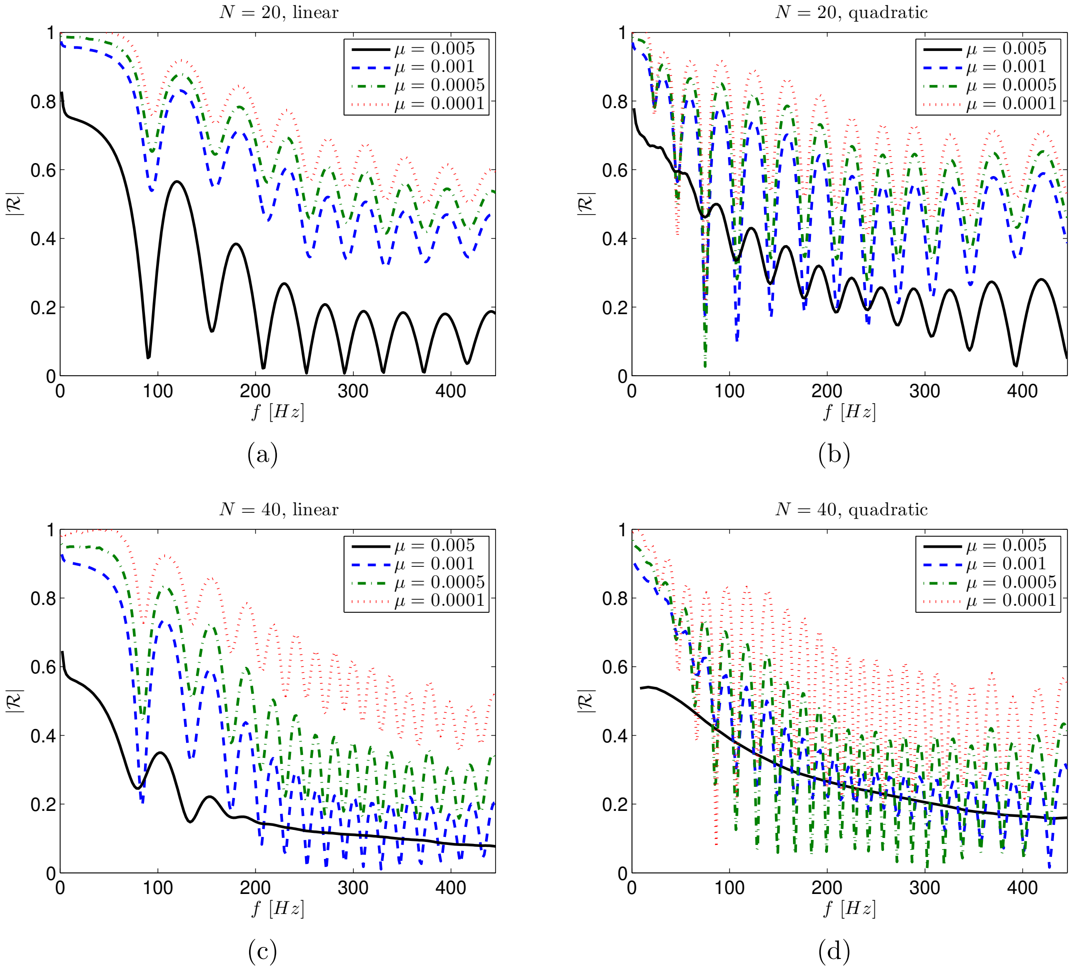
(a) (b) (c) (d)

Figure 4.5: Influence of the boundary admittance coefficient μ on $|\mathcal{R}|$ for linear and quadratic ABHs. (a) Linear ABH with $N = 20$ rings, (b) Quadratic ABH with $N = 20$ rings, (c) Linear ABH with $N = 40$ rings, and (d) Quadratic ABH with $N = 40$ rings.

ones (regardless the number of rings). This fact becomes evident especially at low frequencies. In conclusion, it is worth noting that, as stated in the previous section, the higher number of rings forming the ABH corresponds to a better performance, that is, to smaller values for the reflection coefficient $|\mathcal{R}|$.

4.3.3 Influence of the ring thickness

The case of a linear ABH with a fixed number of $N = 20$ rings, where the ring thickness h_r can vary and it assumes the values $h_r = 0.5, 1, 2, 3$ mm is considered. Analogous results can be achieved for quadratic configurations. It can be seen in Figure 4.6 that the general performance of the ABH it is not affected by its ring thickness. This parameter only has an influence on the frequency location of peaks and dips.

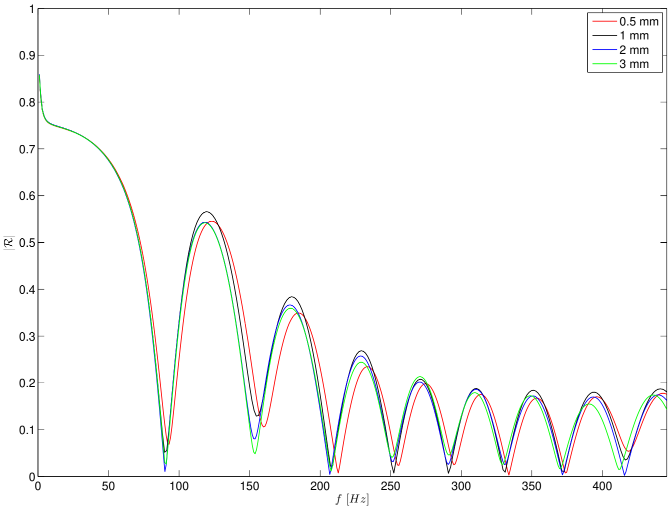

Figure 4.6: Influence of the ring thickness on the reflection coefficient for the linear case with $N = 20$ rings.

4.3.4 Pressure distribution inside the ABH

For this study, the configuration of a linear ABH with 20 rings and $\mu = 0.005$ is chosen. First of all, we consider three points P_1, P_2 and P_3 located respectively at the beginning, middle and end positions of the ABH center line (see Figure 4.7). Their coordinates are $P_1 = (-0.5, 0)$, $P_2 = (-0.237, 0)$ and $P_3 = (-0.062, 0)$, with the origin of coordinates being located at the end of the ABH termination. Then, the pressure is collected at such locations. In Figure 4.8(a), the acoustic pressure evolution at the three points is depicted. Although the initial peak is higher at P_1, at the entrance of the ABH region, than at P_3, as time evolves the acoustic energy at low frequencies tends to concentrate at the end of the ABH. This can be more evidently appreciated by looking at the pressure spectra in Figure 4.8(b). Compared to the other points, in fact, P_3 exhibits higher pressure values in the low frequency range. However, is is to be noted that a strong decay of the P_3 spectrum is produced at high frequencies. So, this indicates that the last rings play an important role in the absorption of low frequency acoustic pressure, as those rings have the largest area and the pressure field gets particularly intense there. On the

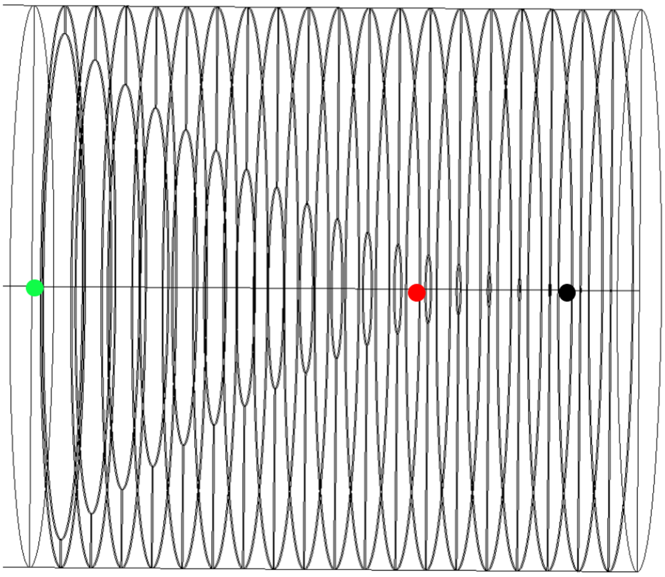

Figure 4.7: The points P_1 (in green), P_2 (in red) and P_3 (in black) located on the ABH center line.

other hand, the first rings may absorb the higher frequencies. In Figure 4.9 it can be appreciated, through a series of snapshots, how the Gaussian pulse gets absorbed by the ABH. While the wave is entering the retarding structure, the cavities play a fundamental role in the absorption process. On the other hand, we can notice how a small part of the incident wave is reflected in Figure 4.9(e) in yellow. This is not surprising and it is expected, otherwise the ABH would be perfect with zero reflection coefficient. It is to be noted

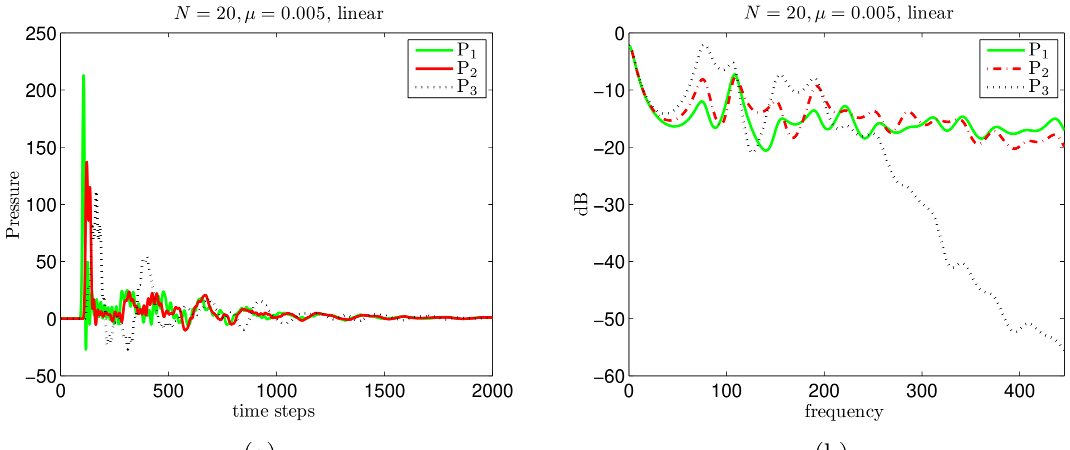

(a) (b)

Figure 4.8: (a) Pressure signals measured inside the ABH at points $P_1 = (-0.5, 0)$, $P_2 = (-0.237, 0)$ and $P_3 = (-0.062, 0)$ and (b) corresponding spectra.

that, in order to properly visualize the pressure distribution inside the duct and the ABH, the legend scale has been modified from one figure to another. Finally, in Figure 4.9 it can be appreciated, especially in Figure 4.9(e), that the pressure does not distribute in a uniform way inside the cavities, as it has been found in (Mousavi *et al.*, 2022).

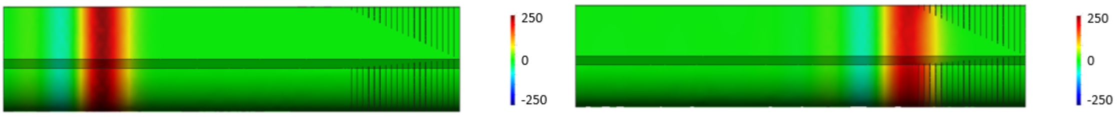

(a) $t = 0.0025$ s (b) $t = 0.005$ s

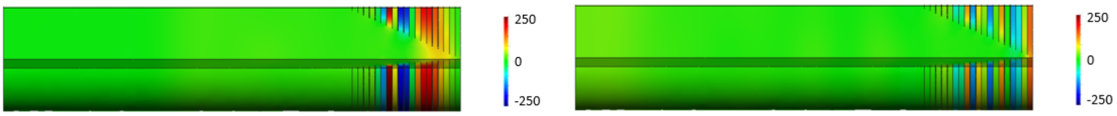

(c) $t = 0.0075$ s (d) $t = 0.01$ s

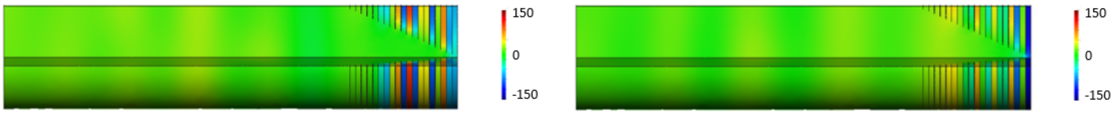

(e) $t = 0.0125$ s (f) $t = 0.015$ s

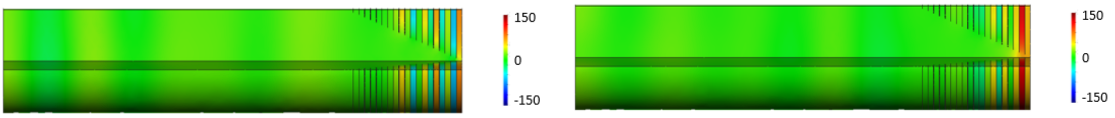

(g) $t = 0.0175$ s (h) $t = 0.02$ s

Figure 4.9: Pressure evolution at different times.

By following the same logic, several tracking points equally spaced are located in the center line, equaling the number of cavities. So that it is possible to analyze the behavior of the four ABHs by studying the acoustic pressure within each cavity. Moreover, the boundary admittance coefficient is reduced to $\mu = 0.0005$ so as to better observe all resonance modes. In Figure 4.10, the pressure spectra of all the points are plotted and compared to the reflection coefficient, which has been scaled with a factor of 30 for visualization purposes.

It looks evident, by looking at the four configurations considered, that the reflection coefficient does not start to oscillate until a resonance appear. With regards to the number of rings, it seems that they to do not influence too much the general structure of the reflection coefficient oscillations. However,

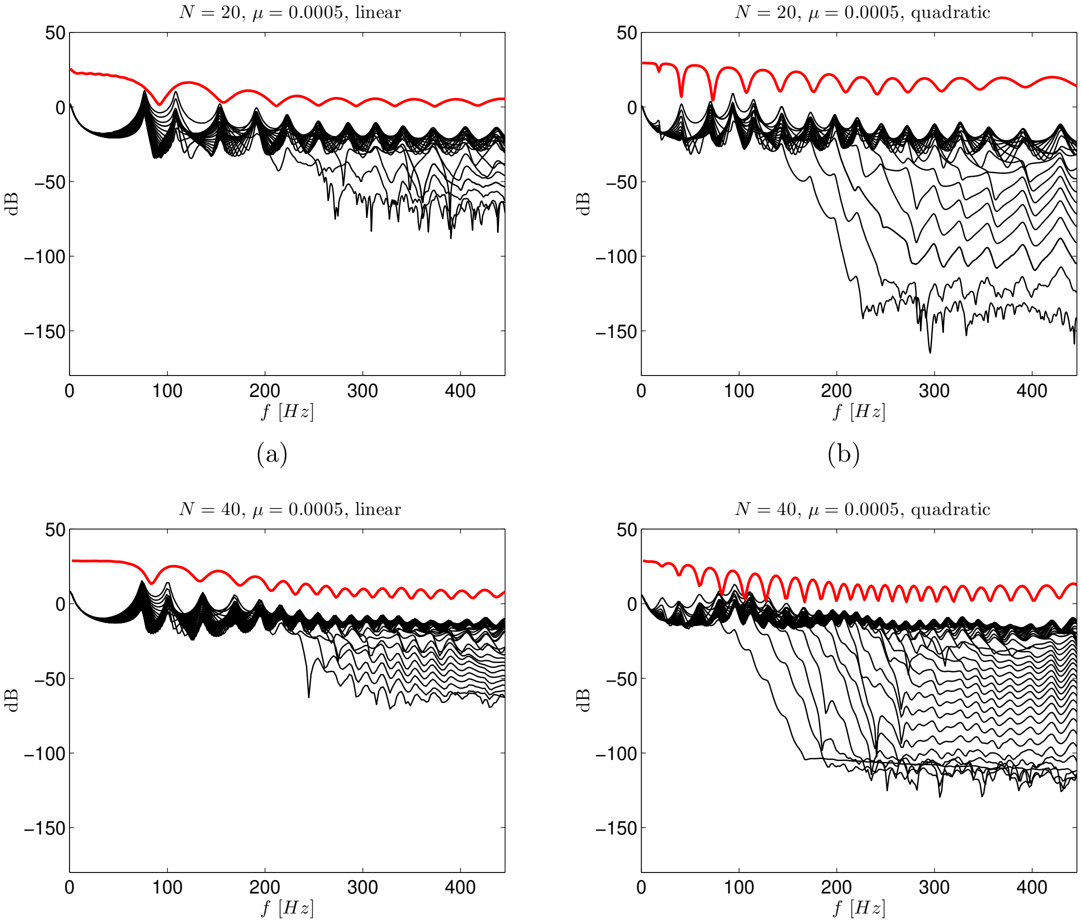

(a) (b)

(c) (d)

Figure 4.10: Comparison between scaled reflection coefficient (in red) and pressure spectra for $\mu = 0.0005$ (a) Linear ABH with $N = 20$ rings, (b) Quadratic ABH with $N = 20$ rings, (c) Linear ABH with $N = 40$ rings, and (d) Quadratic ABH with $N = 40$ rings.

it can be observed that increasing the number of rings leads to a higher number of resonances in the spectra. Consequently, this also increases the number of oscillations in the reflection coefficient. In fact, in (Mousavi *et al.*, 2022) a relationship between the inner radius of cavities and resonance frequency is presented.

In conclusion, it is to be underlined that Figure 4.10 reveals the essential on how the ABH works. By looking at the spectra it can be seen that, while all the cavities get excited at low frequencies, each spectra starts to decay, at some particular frequency, in a sorted way. It is remarkable that the first decaying spectra correspond to the last cavities, when the last spectrum relates to the first cavity. When the incident field reaches the last cavities its high frequency components have already disappeared through the excitation of the resonances in all previous cavities. In fact, the ABH works as a rainbow trapping absorber where the resonances of the cavities are the main mechanism playing a role in the absorption process, not the ABH effect itself.

4.3.5 Influence of the ABH final wall

The boundary conditions at wall Γ_L are modified in order to study its influence on the overall ABH performance. The case of a linear ABH with 20 rings and $\mu = 0.005$ at walls is considered, while only the condition regarding the final wall at the end of the termination is changed. Namely, the cases of Sommerfeld condition ($\mu = 1$) and rigid wall ($\mu = 0$) are considered. The reflection coefficient for the two cases is depicted in Figure 4.11. In the case of the Sommerfeld condition, the lower frequencies of the wave continue propagating towards the right and they do not notice the impact of the ABH geometry. In fact, in an extreme case the reflection coefficient would be zero at very low frequencies while the opposite occurs if the termination is rigid. In this last case, the low frequency wave get totally reflected as when encountering a rigid flat wall and the reflection coefficient is one. Therefore,

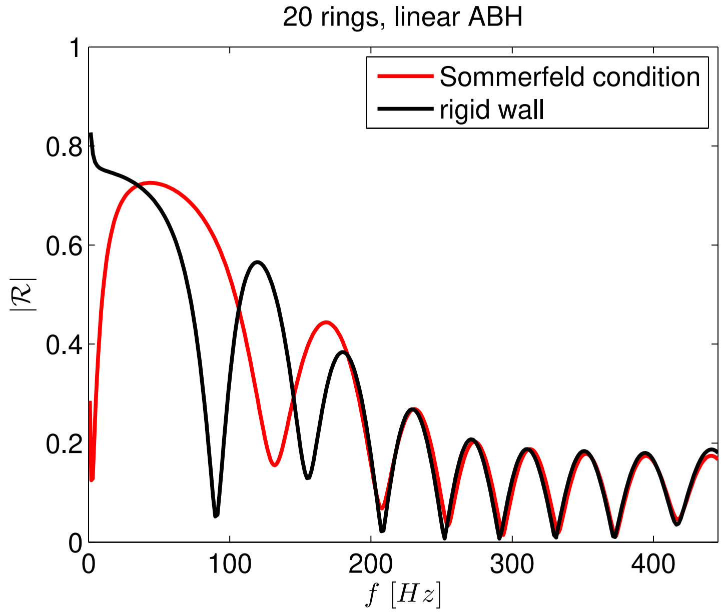

Figure 4.11: The wall at the end of the ABH termination has an influence only at low frequencies (the last cavities).

the two reflection coefficients differs at low frequency, while they coincide at middle-high frequency within the considered range. This goes inline with the findings of (Mousavi *et al.*, 2022). Moreover, it is to be noted that is coherent with the results from the previous sections: since the low frequencies are absorbed by the rings placed closed to the ABH termination, in this range it becomes evident the influence of the final wall. On the contrary, the conditions over Γ_L do not affect the ABH performance at high frequency, since they are absorbed by the rings placed at the entrance of the retarding structure.

4.3.6 Occlusion of the first cavities

Motivated by the previous findings, a new design of the ABH termination can be proposed. In fact, the first cavities would absorb frequencies much higher than the cutoff frequency of the tube. Therefore, they can be occluded (see Figure 4.12) and a very similar ABH performance is obtained (see Figure 4.13). Moreover, in the profile occluding the first cavities, it is not necessary to put some absorption (see Figure 4.14). These results can be very important from a manufacturing point of view.

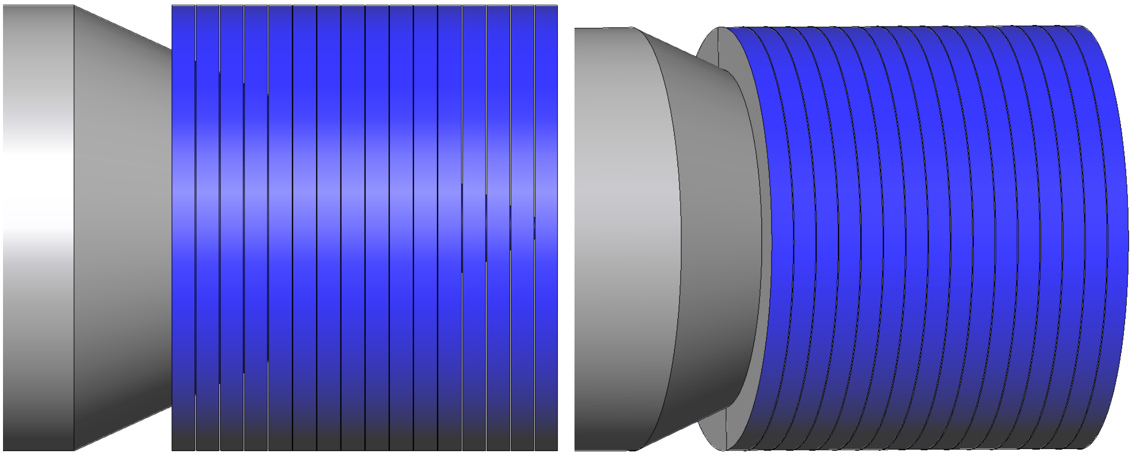

Figure 4.12: Two different views of the same geometry: linear ABH with 16 cavities and 4 occluded.

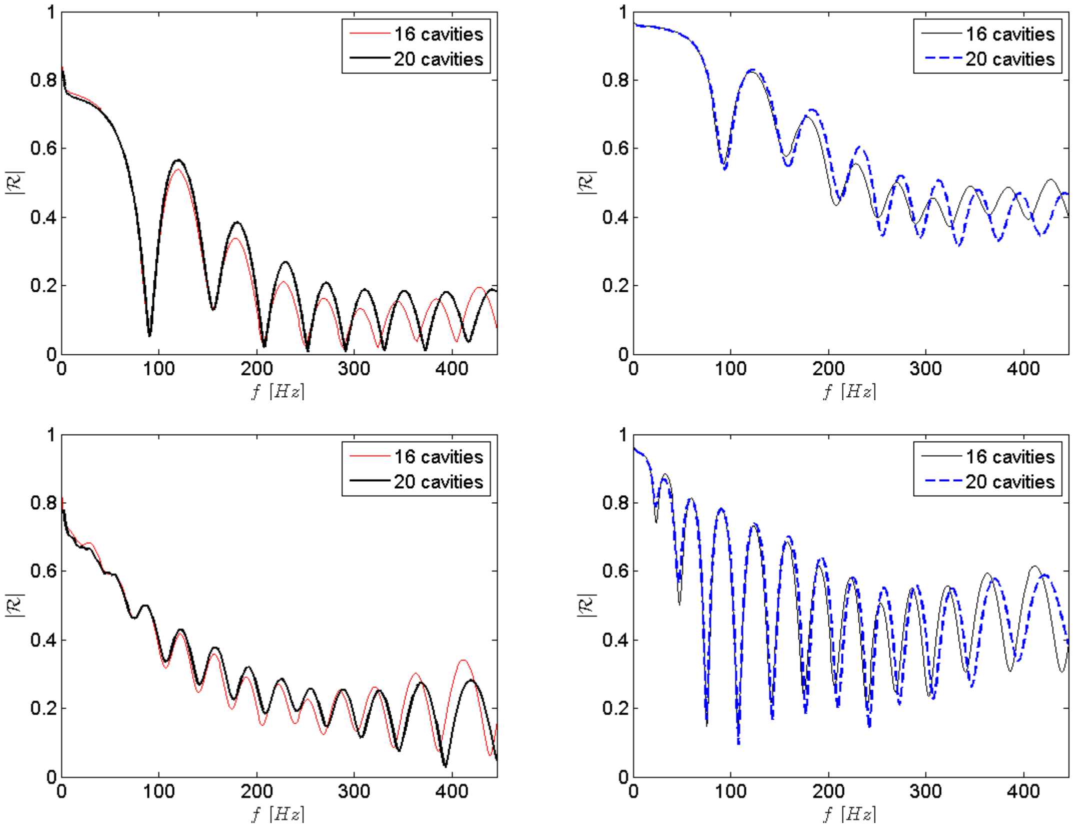

Figure 4.13: Comparison between reflection coefficients for configurations with 20 and 16 cavities (4 occluded), for linear (top) and quadratic (bottom) order, with $\mu = 0.005$ (left) and $\mu = 0.001$ (right).

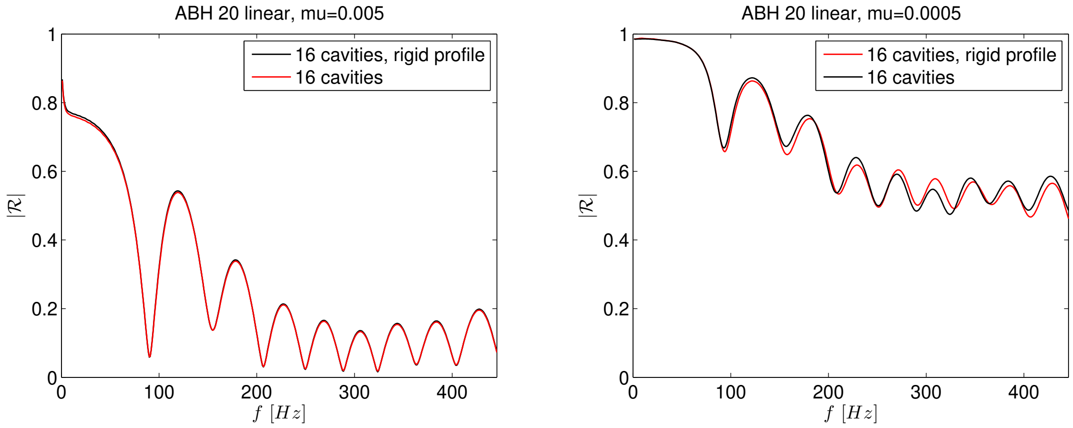

Figure 4.14: Comparison between linear profile with absorption and without it. Linear ABHs with $\mu = 0.005$ and $\mu = 0.0005$.

4.4 Conclusions

Four main ABH configurations have been simulated through the Finite Element Method. The influence of parameters, such as the number of rings and the boundary admittance coefficient on the reflection coefficient of the ABHs have been studied. Such quantity is a great indicator of the ABH performance and it has been computed with a numerical adaptation of the classical two-microphone transfer function (TMTF) method. As expected, augmenting the number of rings leads to an improvement of the ABH performance, although it can be detrimental from the manufacturing point of view, and it increases the number of oscillations in the reflection coefficient. Similarly, increasing the boundary admittance coefficient results in higher absorption. Moreover, pressure spectra at several points located at the center line of the ABH have been computed and visualized. With this result, the general behavior of the ABH can be understood and the relationship between cavities and range of absorbed frequencies is observed. Such behavior can be appreciated also by considering different conditions at the ABH final wall (such as Sommerfeld condition and rigid wall) and visualizing their influence on the reflection condition. Finally, the visualization of the pressure field evolution shows an excellent functioning of the ABH with a very small quantity of reflected wave.

Chapter 5

Conclusions and future work

5.1 Conclusions

This thesis has focused on the semi-analytical and numerical characterization of acoustic black holes in duct terminations. Specific conclusions and discussions have already been presented at the end of each chapter, so this section will briefly describe the main contributions of the thesis.

These can be summarized as follows:

1. **A theoretical framework for the analysis of ABHs** has been presented in Chapter 2. This is achieved through the variational formulation of the problem (a Helmholtz equation with spatial-dependent wavenumber), whose solution is found using Gaussians as admissible basis functions. The ABH modes are computed via an eigenvalue problem formulated following a similar approach. In addition, the dependence of the shape and distribution of the modes on the residual radius and damping makes it possible to clarify the occurrence and disappearance of oscillations in the input admittance and reflection coefficient of the ABH at different frequencies.

   This has resulted in the publications (J2) and (C2), see Section 5.3.

   The aim of these publications is to contribute to the comprehension of the behavior of theoretical or ideal ABHs in duct terminations. In fact, since the original proposal in (Mironov and Pislyakov, 2002), the majority of research efforts on ABHs has been devoted to their practical realization. But, further explorations of ideal ABHs can be very important to better understand their behavior and provide hints for industrial designs. While in (Mironov and Pislyakov, 2002) it was proposed to introduce a length imperfection in order to overcome the singularity at the ABH termination, in (J2) and (C2) a rigid residual surface is considered, which is analogous to the residual thickness for ABHs in beams and plates (see, Krylov, 2004; Krylov and Tilman, 2004; O'Boy and Krylov, 2011). The solution of the Helmholtz equation with spatially varying wavenumber could be computed via a high-order WKB expansion (as done in (Karlos *et al.*, 2019) for ABHs in beams) or through the Bremmer series for the equation (Bremmer, 1951; Atkinson, 1960; Doc *et al.*, 2016). However, the former implies dealing with a series that tends to diverge, while the latter carries difficulties with the evaluation of numerical integrals and the imposition of complex boundary conditions. Those are the main reasons for the proposed approach in Chapter 2, which has been validated against FEM results.

2. **A formal proof of the consistency of the TMM solution** has been presented in Chapter 3. The TMM provides a first step towards the characterization of more realistic ABHs, than those analyzed in Chapter 2. The proof relies on showing the equivalence between the governing equation of an acoustic wave propagating inside a duct with an inner radius decreasing by according to power-law and the equation of wave propagation in a duct filled with a metafluid with power-law increasing density. The Transfer Matrix Method (TMM) can be used to solve the latter and it is shown that the TMM solution tends to the continuous one when the number of metafluid layers (equivalently the number of rings and cavities in the ABH termination) tends to infinity. Finally, the TMM is used to compute the reflection coefficient for linear and quadratic ABH. Their behavior and speed of convergence, depending on the small imperfection introduced at the end of the termination, are briefly discussed and analyzed.

   This work has been published in (J1), see Section 5.3.

   The TMM is a standard method widely used in many areas of physics, such as the study of vibrations of complex structures (Kang *et al.*, 2016) and articulatory speech synthesis (Sondhi and Schroeter, 1987), just to mention a few. Generally, the main assumption consists in considering uniform physical properties over finite layers. That is, a discretization of the domain is performed. Prior to the contribution provided in (J1), the behavior of the TMM in the limit case where the discretization tends to the continuous problem (that is, the number of layers tends to infinity or their width vanishes) has not been explored. Although in (Guasch *et al.*, 2017) it was showed that the TMM can be used to study and analyzed practical realizations of ABHs in duct terminations, in (J1) it has been proved that the TMM solution tends to the continuous one, which certifies the validity of the method. To provide a rigorous demonstration, the concept of metafluid (Cummer *et al.*, 2016) has been used. An ABH based on the equivalence between the generalized Webster equation governing acoustic plane wave propagation in the ABH and the wave equation for a metafluid with a power-law varying density was recently experimentally tested in (Mironov and Pislyakov, 2020).

3. **Preliminary FEM results for ABHs in duct terminations** have been presented in Chapter 4. This consists in solving the wave equation in mixed form in a simulated impedance tube equipped with linear and quadratic ABHs. The reflection coefficient, that is the indicator of the ABH performance, is computed via a numerical adaptation of the two-microphone transfer function method (TMTF). The influence of the ABH behavior on many parameters such as the ABH order, the number of rings and the absorption coefficient at walls is studied. Moreover, the general behavior of an ABH in duct terminations is understood and the relationship between cavities and damped frequencies is described.

   This work has been presented in (C1), see Section 5.3.

   When (C1) was presented, to the best of authors knowledge it was the first work applying FEM to ABHs in duct terminations. In fact, the theory was already formulated in (Mironov and Pislyakov, 2002), first experiments were carried out (El Ouahabi *et al.*, 2015; El Ouahabi *et al.*, 2015b) and, as a consequence of the discrepancy between theoretical and experimental results, methods to better understand the ABH performance, such as the TMM (Guasch *et al.*, 2016b; Guasch *et al.*, 2017), began to be investigated. While the FEM drawback is its computational cost, the main advantage is that it relies on less assumptions than semi-analytical methods and the TMM, therefore providing results closer to reality. This allowed to visualize the wave propagation inside ducts equipped with an ABH, something that it was not possible in the aforementioned works. Thereby, ABH cavities were observed to interact with each other and to respond in different ways depending on frequencies. In more recent FEM works (Cervenka and Bednarík, 2022) and (Mousavi et al., 2022) an explanation of the relationship between the absorption process in the ABH and the role played by cavity resonances and the different types and damping is provided. This has been achieved by simulating the linearized Navier-Stokes equations, which can take into account visco-thermal losses naturally or by simulating modified Helmholtz equations, respectively. These aspects were not considered in (C1), where only the losses due to the wall boundary admittance were taken into account.

5.2 Future work

The work contained in this thesis leaves several lines of research open for future exploration.

- **Periodic acoustic black holes** in duct terminations deserve future attention. They have been recently proposed in (Mi *et al.*, 2022) showing strong attenuation of the sound transmission loss in the low-frequency range thanks to Bragg scattering in addition to the ABH effect at high frequencies. Therefore, such configuration could serve as a broadband absorber. Moreover, band gaps could be achieved, suggesting the idea that periodic ABHs in ducts could be used for efficient wave filtering. In this thesis, periodic ABHs have not been taken into account, being a single ABH termination with a closed rigid end the subject of study. However, the theoretical, TMM and FEM approaches in Chapters 2, 3 and 4 could be used to calculate reflection, absorption and transmission coefficients of periodic ABHs. In fact, the TMM was used in (Mi *et al.*, 2022) to compare experiments with theoretical predictions.

- **Improvement of the ABH performance at low frequencies**. As an alternative to periodic ABHs, in (Zhang *et al.*, 2021) an ABH in a duct termination is combined with micro-perforated panels (MPPs) to achieve broadband sound absorption, including the low-frequency range. Also, in (Liang *et al.*, 2023) the sound absorption of ABHs with MPP is studied with FEM. More research in the topic needs to be done. A parametric study could be held to find an optimal structure for sound absorption at low frequencies. Therefore, the method used in Chapter 4 could be a starting point to achieve this. On the one hand, the computational domain could be equipped with micro-perforated panels. On the other hand, a study on the position of the micro-perforation, that might be not uniform and grouped in a localized area of the domain, could help improving the ABH performance at low frequencies.

- **Muffler's design inspired by ABHs**. In (Sharma and Umnova, 2018) 3D printed silencers based on the acoustic black hole effect have been studied numerically and validated experimentally. Also, in (Sharma *et al.*, 2017) transmission loss, absorption and reflection coefficients are analyzed for outer flare shaped mufflers. In (Bravo and Maury, 2023), a fully-opened ABH-type silencer made up of annular cylindrical cavities is modelled, optimized and tested to achieve full dissipation of the incident energy over a wide frequency band. As a future work, numerical and experimental aero-acoustic approaches should be carried out in order to further assess how flow-induced noise will influence the ABH effect. Moreover, other power laws for cavity radii may be explored.

- **Mean flow and thermal effects**. For mufflers inspired on ABHs the effects of mean flow in the duct and also thermal effects may be considered (see (Bravo and Maury, 2023) for initial consideration of mean flow effects). Neither of them were considered in the TMM and FEM simulations of Chapters 3 and 4, respectively. In (Liang *et al.*, 2023) the sound absorption of an ABH with micro-perforated panels is studied, but neither mean flow or thermal effects are considered. This is important if one thinks of practical muffler design for automotive exhaust systems, ventilation and air-conditioned systems, etc.

- **ABHs for room acoustics** Another research field would be the study of the ABH effect applied to architectural acoustics. One can imagine to add one or several ABHs on a wall or ceiling and analyze how they influence the acoustic parameters of the room, such as the reverberation time. The theoretical and methodological knowledge gained in this thesis would help to characterise how ABH parameters could influence room acoustics. The optimal location of the ABHs, the possibility of using ABHs of different geometries, etc. should be studied.

5.3 Publications

Academic journals

(J2) Jie Deng, Oriol Guasch and Davide Ghilardi, ”Solution and analysis of theoretical sonic black holes in duct terminations”, Journal of Sound and Vibration, Submitted.

(J1) Oriol Guasch, Patricia Sánchez-Martín and Davide Ghilardi, (2020) ”Application of the transfer matrix approximation for wave propagation in a metafluid representing an acoustic black hole duct termination”, Applied Mathematical Modelling, 77, pp. 1881-1893.

International conferences

(C2) Jie Deng, Oriol Guasch and Davide Ghilardi, ”Gaussian series for sonic black holes in duct terminations”, 10th Forum Acusticum 2023, September 11-15, Turin, Italy, Accepted.

(C1) Davide Ghilardi, Marc Arnela and Oriol Guasch, (2018) ”Finite element simulations of the acoustic black hole effect in duct terminations”, 6th Noise and vibration emerging methods (NOVEM2018), May 7-9, Santa Eulària des Riu, Ibiza, Spain.

Bibliography

Arnela, M. (**2015**), ”Numerical production of vowels and diphtongs using finite element methods”, Ph.D. dissertation, La Salle, Ramon Llull University, Barcelona, Spain.

Arnela, M. and Guasch, O. (**2013**), ”Finite element computation of elliptical vocal tract impedances using the two-microphone transfer function method”, J. Acoust. Soc. Am., **133**(6), pp. 4197-4209.

Atkinson, F. (**1960**), ”Wave propagation and the Bremmer series”, J. Math. Anal. Appl., **1**(3-4), pp. 255-276.

Baccarelli, I., Gianturco, F. A., González-Lezana, T., Delgado-Barrio, G., Miret-Artés, S., and Villareal, P. (**2007**), ”Vibrational and rotational bound states in floppy triatomic systems: The distributed Gaussian functions approach”, Phys. Rep., **452**(1) pp. 1-32.

Batut, C., Belabas, K., Bernardi, D., Cohen, H., and Olivier, M. (**2000**), ”User's Guide to PARI-GP”, (Université de Bordeaux I).

Bazilevs, Y., Calo, V. M., Cottrell, J. A., Hughes, T. J. R., Reali, A., and Scovazzi, G. (**2007**), ”Variational multiscale residual-based turbulence modeling for large eddy simulation”, Comput. Methods Appl. Mech. Engrg., **197**(1-4) pp. 173-201.

Bellman, R. and Kalaba, R. (**1959**), ”Functional equations, wave propagation and invariant imbedding”, J. Math. Mech., pp. 683-704.

Bergmann, P. G. (**1946**), ”The wave equation in a medium with a variable index of refraction”, J. Acoust. Soc. Am., **17**(4) pp. 329-333.

Bowyer, E. P. and Krylov, V. V. (**2016**), ”Slots of power-law profile as acoustic black holes for flexural waves in metallic and composite plates”.”, Structures, **6**, pp. 48-58.

Bowyer, E. P., O'Boy, D. J., Krylov, V. V., and Gautier, F. (**2013**), "Experimental investigation of damping flexural vibrations in plates containing tapered indentations of power-law profile", Appl. Acoust., **74**(4), pp. 553-560.

Bravo, T. and Maury, C. (**2023**), "Broadband sound attenuation and absorption by duct silencers based on the acoustic black hole effect: Simulations and experiments", J. Sound Vib., **561**, 117825.

Brekhovskikh, L. (**2012**), *Waves in layered media*, Vol. 16, (Elsevier).

Bremmer, H. (**1951**), "The WKB approximation as the first term of a geometric-optical series", Comm. Pure Appl. Math., **4**(1), pp. 105-115.

Carbó, R. (**1997**), "Wave reflection from a transitional layer between the seawater and the bottom", J Acoust. Soc. Am., **101**(1), pp. 227-232.

Caussé, R., Kergomard, J., and Lurton, X. (**1984**), "Input impedance of brass musical instruments - comparison between experiment and numerical models", J. Acoust. Soc. Am., **75**(1), pp. 241-254.

Cervenka, M. and Bednarík, M., (**2013**), "Non-paraxial model for a parametric acoustic array", J. Acoust. Soc. Am., **134**(2), 933.

Cervenka, M. and Bednarík, M., (**2022**), "On the role of resonance and thermoviscous losses in an implementation of "acoustic black hole" for sound absorption in air", Wave motion, **114**, 103039.

Chua, J. W., Li, X., Yu, X., and Zhai, W. (**2023**), "Novel slow-sound lattice absorbers based on the sonic black hole", Composite Structures, **304**(2), 116434.

Climente, A., Torrent, D., and Sanchez-Dehesa, J. (**2014**), "Gradient index lenses for flexural waves based on thickness variations", Appl. Phys. Lett, **105**, 064101064101.

Climente, A. (**2015**), "Refractive devices for acoustical and flexural waves", Ph.D. dissertation, Universitat Politécnica de València, Valencia, Spain.

Codina, R. (**2002**), "Stabilized finite element approximation of transient incompressible flows using orthogonal subscales", Comput. Methods Appl. Mech. Engrg., **191**(39-40), pp. 4295-4321.

Codina, R. (**2008**), "Finite element approximation of the hyperbolic wave equation in mixed form", Comput. Methods Appl. Mech. Engrg., **197**(13-16), pp. 1305-1322.

Codina, R., Principe J., Guasch, O., and Badia, S. (**2007**), "Time dependent subscales in the stabilized finite element approximation of incompressible flow problems", Comput. Methods Appl. Mech. Engrg., **196**(21-24), pp. 2413-2430.

Conlon, S. C., Fahnline J. B., and Semperlotti, F. (**2015**), "Numerical analysis of the vibroacoustic properties of plates with embedded grids of acoustic black holes", J. Acoust. Soc. Am., **137**(1), pp. 447-457.

Cummer, S. A., Christensen, J., and Alù, A. (**2016**), "Controlling sound with acoustic metamaterials", Nat. Rev. Mater., **1**(3), 16001.

Deng, J. (**2020**), "Vibroacoustic modeling of acoustic blackhole applications in flat, curved and complex mechanical structures", Ph.D. dissertation, La Salle, Ramon Llull University, Barcelona, Spain.

Deng, J., Guasch, O., and Ghilardi, D. (**2023**), "Gaussian series for sonic black holes in duct terminations", Forum Acusticum 2023, Submitted.

Deng, J., Guasch, O., and Ghilardi, D. (**2023**), "Solution and analysis of theoretical sonic black holes in duct terminations", J. Sound Vib., Submitted.

Deng, J., Guasch, O., and Zheng, L. (**2019**), "Ring-shaped acoustic black holes for broadband vibration isolation in plates", J. Sound Vib., **458**, pp. 109-122.

Deng, J., Guasch, O., and Zheng, L. (**2020**), "A semi-analytical method for characterizing vibrations in circular beams with embedded acoustic black holes", J. Sound Vib., **476**, 115307.

Deng, J., Guasch, O., and Zheng, L. (**2021**), "Reconstructed Gaussian basis to characterize flexural wave collimation in plates with periodic arrays of annular acoustic black holes", Int. J. Mech. Sci., **194**, 106179.

Deng, J., Xu, Y., Guasch, O., Gao, N., Tang, L., and Chen, X. (**2023**), "A two-dimensional wave and Rayleigh–Ritz method for complex dispersion in periodic arrays of circular damped acoustic black holes", Mech. Syst. Signal Pr., **200**, 110507.

Deng, J., Zheng, L., Guasch, O., Wu, H., Zeng, P., and Zuo, Y. (**2019**), "Gaussian expansion for the vibration analysis of plates with multiple acoustic black holes indentations", Mech. Syst. Signal Pr., **131**, pp. 317-334.

Deng, J., Zheng, L., Zeng, P., Zuo, Y., and Guasch, O. (**2019**b), "Passive constrained viscoelastic layers to improve the efficiency of truncated acoustic black holes in beams", Mech. Syst. Signal Pr., **118**, pp. 461-476.

Doc, J.B., Lihoreau, B., Felix, S., and Pagneux, V. (**2016**), "Bremmer series for the multimodal sound propagation in inhomogeneous waveguides", Wave Motion, **67**, pp. 55-67.

El-Ouahabi, A., Krylov, V., and O'Boy, D. (**2015**), "Experimental investigation of the acoustic black hole for sound absorption in air", in *Proc. of 22nd International Congress on Sound and Vibration* (Florence, Italy).

El-Ouahabi, A., Krylov, V., and O'Boy, D. (**2015**b), "Investigation of the acoustic black hole termination for sound waves propagating in cylindrical waveguides", in *Proc. of the INTER-NOISE and NOISE-CON Congress and Conference* (Institute of Noise Control Engineering, San Francisco, USA).

Feurtado, P. A. and Conlon, S. C. (**2015**), "Investigation of boundary-taper reflection for acoustic black hole design", Noise Control Eng. J., **63**(5), pp. 460-466.

Feurtado, P. A. and Conlon, S. C. (**2016**), "An experimental investigation of acoustic black hole dynamics at low, mid, and high frequencies", J. Vib. Acoust., **138**, 061002-1.

Georgiev, V. B., Cuenca, J., Gautier, F., Simon, L., and Krylov, V. V. (**2011**), "Damping of structural vibrations in beams and elliptical plates using the acoustic black hole effect", J. Sound Vib., **330**(11), pp. 2497-2508.

Ghilardi, D., Arnela, M., and Guasch, O. (**2018**), "Finite element simulations of the acoustic black hole effect in duct terminations", in *Proc. of the Noise* *and Vibration Emerging Methods, NOVEM2018* (Santa Eulària des Riu, Ibiza, Spain) **257**, pp. 887-897.

Guasch, O., Arnela, M., Codina, R., and Espinoza, H. (**2016**), "A stabilized finite element method for the mixed wave equation in an ALE framework with application to diphtong production", Acta Acust. united Ac., **102**(1), pp. 94-106.

Guasch, O., Arnela, M., and Sánchez-Martín, P. (**2016b**), "Transfer matrices to analyze the acoustic black hole effect in duct terminations", in *Proc. of the INTER-NOISE and NOISE-CON Congress and Conference* (Institute of Noise Control Engineering), **253**, pp. 2590-2598.

Guasch, O., Arnela, M., and Sánchez-Martín, P. (**2017**), "Transfer matrices to characterize linear and quadratic acoustic black holes in duct terminations", J. Sound Vib., **395**, pp. 65-79.

Guasch, O. and Codina, R. (**2007**), "An algebraic subgrid scale finite element method for the convected Helmholtz equation in two dimensions with applications in aeroacoustics", Comput. Methods Appl. Mech. Engrg., **196**(45-48), pp. 4672-4689.

Guasch, O., Codina, R., Arnela, M., and Espinoza, H. (**2014**), "A stabilized Arbitrary Lagrangian Eulerian Finite Element Method for the mixed wave equation with application to diphtong production", in *11th World Congress on Computational Mechanics (WCCM)*, Barcelona, Spain.

Guasch, O. and Sánchez-Martín, P. (**2017**), "Power-law density metafluids to achieve the acoustic black hole effect in duct terminations", in *Proc. of the INTER-NOISE and NOISE-CON Congress and Conference* (Institute of Noise Control Engineering), **255**, pp. 1716-1726.

Guasch, O., Sánchez-Martín, P., and Ghilardi, D. (**2020**), "Application of the transfer matrix approximation for wave propagation in a metafluid representing an acoustic black hole duct termination", Appl. Math. Model., **77**, pp. 1881-1893.

Hiyama, E., Kino, Y., and Kamimura, M. (**2003**), "Gaussian expansion method for few-body systems", Prog. Part. Nucl. Phys., **51**(1), pp. 223-307.

Hook, K., Cheer, J., and Daley, S. (**2019**), "A parametric study of an acoustic black hole on a beam", J. Acoust. Soc. Am., **145**(6), pp. 3488-3498.

Huang, W., Ji, H., Qiu, J., and Cheng, L. (**2018**), "Analysis of ray trajectories of flexural waves propagating over generalized acoustic black hole indentations", J. Sound Vib., **417**, pp. 216-226.

Hughes, T. J. R. (**1995**), "Multiscale phenomena: Green's function, the Dirichlet-to-Neumann formulation, subgrid scales models, bubbles and the origins of stabilized formulations", Comput. Methods Appl. Mech. Engrg., **127**(1), pp. 387-401.

Hughes, T. J. R., Feijóo, G. R., Mazzei, L., and Quincy, J. B. (**1998**), "The variational multiscale method, a paradigm for computational mechanics", Comput. Methods Appl. Mech. Engrg., **166**(1), pp. 3-24.

Ji, H., Luo, J., Qiu, J., and Cheng, L. (**2018**), "Investigations on flexural wave propagation and attenuation in a modified one-dimensional acoustic black hole using a laser excitation technique", Mech. Syst. Signal Pr., **104**, pp. 19-35.

Jiménez, N., Romero-García, V., Pagneux, V., and Groby, J. P. (**2017**), "Rainbow-trapping absorbers: Broadband, perfect and asymmetric sound absorption by subwavelength panels for transmissions problems", Sci. Rep., **7**, 13595.

Kalkowski, M. K., Muggleton, J. M., and Rustighi, E. (**2017**), "An experimental approach for the determination of axial and flexural wavenumbers in circular exponentially tapered bars", J. Sound Vib., **390**, pp. 67-85.

Kang, H., Xie, W., and Guo, T. (**2016**), "Modeling and parametric analysis of arch bridge with transfer matrix method", Appl. Math. Model., **40**(23.24), pp. 10587-10595.

Karlos, A., Elliott, S. J., and Cheer, J. (**2019**), "Higher-order WKB analysis of reflection from tapered elastic wedges'", J. Sound Vib., **449**, pp. 368-388.

Kralovic, V. and Krylov, V. (**2007**), "Damping of flexural vibrations in tapered rods of power-law profile: Experimental studies", Proc. Inst. Acoust., **5**, pp. 66-73.

Krylov, V. (**1990**), "Localized acoustic modes of a quadratic solid wedge", Moscow Univ. Phys. Bull., **45**, pp. 65-69.

Krylov, V. (**2004**), "New type of vibration dampers utilising the effect of acoustic 'black holes'", Acta Acoust., **90**(5), pp. 830-837.

Krylov, V. (**2007**), "Propagation of plate bending waves in the vicinity of one-and two-dimensional acoustic black holes", in *ECCOMAS Thematic Conference on Computational Methods* (Rethymno, Crete, Greece).

Krylov, V. (**2014**), "Acoustic black holes: Recent developments in the theory and applications", IEEE Transactions on Ultrasonics, Ferroelectrics, and Frequency Control, **61**(8), pp. 1296-1306.

Krylov, V. and Tilman, F. (**2004**), "Acoustic black holes for flexural waves as effective vibration dampers", J. Sound Vib., **274**(3), pp. 605-619.

Krylov, V. V. and Winward, R. E. T. B. (**2007**), "Experimental investigation of the acoustic black hole effect for flexural waves in tapered plates", J. Sound Vib., **300**(12), pp. 43-49.

Lee, J. Y. and Jeon, W. (**2017**), "Vibration damping using a spiral acoustic black hole", J. Acoust. Soc. Am., **141**(3), pp. 1437-1445.

Lee, J. Y. and Jeon, W. (**2019**), "Exact solution of Euler-Bernoulli equation for acoustic black holes via generalized hypergeometric differential equation", J. Sound Vib., **452**, pp. 191-204.

Li, X. and Ding, Q. (**2018**), "Analysis on vibration energy concentration of the one-dimensional wedge-shaped acoustic black hole structure", J. Intell. Mater. Syst. Struct., **29**(10), pp. 2137-2148.

Li, X. and Ding, Q. (**2019**), "Sound radiation of a beam with a wedge-shaped edge embedding acoustic black hole feature", J. Sound Vib., **439**, pp. 287-299.

Liang, X., Liang, H., Chu, J., Wang, W., Li N., Yang Z., Zhou, G., Gao, N., Hu, C., and Zhou, Z. (**2023**), "A modified sonic black hole structure for improving and broadening sound absorption", Appl. Acoust., **210**, 109440.

Lomonosov, A. M., Yan, S., Han, B., Zhang, H., and Shen, Z. (**2016**), "Orbital-type trapping of elastic lamb waves", Ultrasonics, **64**, pp. 58-61.

Ma, L., Zhang, S., and Cheng, L. (**2018**), "A 2D Daubechies wavelet model on the vibration of rectangular plates containing strip indentations with a parabolic thickness profile", J. Sound Vib., **429**, pp. 130-146.

Mechel, F. P. (**2002**), *Formulas of Acoustics*, (Springer-Verlag, Berlin).

Mi, Y., Zhai, W., Cheng, L., Xi, C., and Yu, X. (**2021**), "Wave trapping by acoustic black hole: simultaneous reduction of sound reflection and transmission", Appl. Phys. Lett., **118**, 114101.

Mironov, M. (**1988**), "Propagation of a flexural wave in a plate whose tickness decreases smoothly to zero in a finite interval", Sov. Phys. Acoust., **34**(3), pp. 318-319.

Mironov, M. and Pislyakov, V. (**2002**), "One-dimensional acoustic waves in retarding structures with propagation velocity tending to zero", Acoust. Phys., **48**(3), pp. 347-352.

Mironov, M. and Pislyakov, V. (**2020**), "One-dimensional sonic black holes: Exact analytical solution and experiments", J. Sound Vib., **473**, 115223.

Mousavi, A., Berggren, M., and Wadbro, E. (**2022**), "How the waveguide acoustic black hole works: A study of possible damping mechanisms", J. Acoust. Soc. Am., **151**(6), pp. 4279-4290.

Munjal, M. L. (**1987**), *Acoustics of Ducts and Mufflers*, 1st Ed., (John Wiley and Sons, New York).

Nakada, H. (**2006**), "Hartree-Fock-Bogolyubov calculations with Gaussian expansion method", Nucl. Phys. A, **764**(C), pp. 117-134.

O'Boy, D. and Krylov, V. (**2011**), "Damping of flexural vibrations in circular plates with tapered central holes", J. Sound Vib., **330**(10), pp. 2220-2236.

O'Boy, D. and Krylov, V. (**2016**), "Vibration of a rectangular plate with a central power-law profiled groove by the Rayleigh-Ritz method", Appl. Acoust., **104**, pp. 24-32.

Park, S., Kim, M., and Jeon, W. (**2019**), "Experimental validation of vibration damping using an Archimedean spiral acoustic black hole", J. Sound Vib., **459**, 114838.

Pelat, A., Gautier, F., Conlon, S. C., and Semperlotti, F. (**2020**), "The acoustic black hole: A review of theory and applications", J. Sound Vib., **476**, 115316.

Plitnik, G. and Strong, W. (**1979**), "Numerical method for calculating input impedances of the oboe", J. Acoust. Soc. Am., **65**(3), pp. 816-825.

Robins, A. J. (**1991**), "Reflection of a plabe wave from a fluid layer with continuously varying density and sound speed", J. Acoust. Soc. Am., **89**(4), pp. 1686-1696.

Ross, D., Ungar E., and Kerwin, E. (**1959**), "Damping of plate flexural vibrations by means of viscoelastic laminae", Structural Damping, pp. 49-88.

Sharma, N. and Umnova, O.(**2018**), "Study of sound absorption capability of silencers based on the acoustic black hole effect", in *Proceedings of ISMA2018 and USD2018*, pp. 1121-1127.

Sharma, N., Umnova, O., and Moorhouse, A. (**2016**), "Analysis of a low frequency muffler based on the acoustic black hole effect", in *Proceedings of the Institute of Acoustics, Acoustics2016*, **38**(1).

Sharma, N., Umnova, O., and Moorhouse, A. (**2017**), "Low frequency sound absorption through a muffler with metamaterial lining", in *24th International Congress on Sound and Vibration* (London, UK).

Singh, K. V. and Ram, Y. M. (**2002**), "Transcendental eigenvalue problem and its application", AIAA J., **40**(7), pp. 1402-1407.

Sondhi, M. and Schroeter, J. (**1987**), "A hybrid time-frequency domain articulatory speech synthesizer", IEEE Trans. Acoust. Speech Signal Process., **35**(7), pp. 955-967.

Tang, L. and Cheng, L. (**2017**), "Broadband locally resonant band gaps in periodic beam structures with embedded acoustic black holes", J. Appl. Phys., **121**, 194901.

Tang, L. and Cheng, L. (**2017b**), "Enhanced Acoustic Black Hole effect in beams with a modified thickness profile and extended platform", J. Sound Vib., **391**, pp. 116-126.

Tang, L. and Cheng, L. (**2017c**), "Ultrawide band gaps in beams with double-leaf acoustic black hole indentations", J. Acoust. Soc. Am., **142**(5), pp. 2802-2807.

Tang, L. and Cheng, L. (**2019**), "Periodic plates with tunneled Acoustic-Black-Holes for directional band gap generation", Mech. Syst. Signal Process., **133**, 106257.

Tang, L. and Cheng, L. (**2020**), "Impaired sound radiation in plates with periodic tunneled Acoustic Black Holes", Mech. Syst. Signal Process., **135**, 106410.

Tang, L., Cheng, L., Ji, H., and Qiu, J. (**2016**), "Characterization of acoustic black hole effect using a one-dimensional fully-coupled and wavelet-decomposed semi-analytical model", J. Sound Vib., **374**, pp. 172-184.

Tisseur, F. and Meerbergen, K. (**2001**), "The quadratic eigenvalue problem", SIAM Review, **43**(2), pp. 235-286.

Umnova, O., Brooke, D., Leclaire, P., and Dupont, T. (**2023**), "Multiple resonances in lossy acoustic black holes - theory and experiment", J. Sound Vib., **543**, 117377.

Vemula, Z., Norris, A. N., and Cody, G. D. (**1996**), "Attenuation of waves in plates and bars using a graded impedance interface at edges", J. Sound Vib., **196**(1), pp. 107-127.

Wang, Z. and Norris, A. N. (**1995**), "Waves in cylindrical shells with circumferential submembers: a matrix approach", J. Sound Vib., **181**(3), pp. 457-484.

Yan, S., Lomonosov A. M., and Shen, Z. (**2016**), "Evaluation of an acoustic black hole's structural characteristics using laser-generated lamb waves", Laser Phys. Lett., **13**(2), 025003.

Yan, S., Lomonosov A. M., and Shen, Z. A. (**2016b**), "Numerical and experimental study of lamb wave propagation in a two-dimensional acoustic black hole", J. Appl. Phys., **119**(21), 214902.

Zeng, P., Zheng, L., Deng, J., Elsabbagh, A., Xiang, S., Yan, T., and Wu, Y. (**2019**), "Flexural wave concentration in tapered cylindrical beams and wedge-like rectangular beams with power-law thickness", J. Sound Vib., **452**, pp. 82-96.

Zhang, X., Cheng, L., Liu, Y., and Du, J. (**2021**), "Acoustic modelling and analyses of geometrically complex systems with Micro-perforated panels", J. Sound Vib., **499**, 115995.

Zhao, C. and Prasad, M. G. (**2019**), "Acoustic Black Holes in Structural Design for Vibration and Noise Control", Acoust., **1**, pp. 220-251.

Zhou, T., Tang, L., Ji, H., Qiu, J., and Cheng, L. (**2017**), "Dynamic and static properties of double-layered compound acoustic black hole structures", Int. J. Appl. Mech., **9**(5), 1750074.